INVESTIGATION INTO THE SYNTHESIS AND CARBON DOPING OF MgB_2 FOR POSSIBLE BULK SUPERCONDUCTING FAULT CURRENT LIMITERS APPLICATION

Jonathan Celvin Archer

Submitted in fulfilment of the Master of Science in Engineering to the
Faculty of Engineering, University of KwaZulu-Natal

21 June 2012

Supervisor: Dr. A.L.L. Jarvis

Declarations

As the candidate's Supervisor I agree/do not agree to the submission of this thesis.

Signed: ________________ Name: _____________________ Date: __________

DECLARATION

I, Jonathan Celvin Archer declare that

(i) The research reported in this dissertation, except where otherwise indicated, is my original work.

(ii) This dissertation has not been submitted for any degree or examination at any other university.

(iii) This dissertation does not contain other persons' data, pictures, graphs or other information, unless specifically acknowledged as being sourced from other persons.

(iv) This dissertation does not contain other persons' writing, unless specifically acknowledged as being sourced from other researchers. Where other written sources have been quoted, then:

a) their words have been re-written but the general information attributed to them has been referenced;

b) where their exact words have been used, their writing has been placed inside quotation marks, and referenced.

(v) Where I have reproduced a publication of which I am an author, co-author or editor, I have indicated in detail which part of the publication was actually written by myself alone and have fully referenced such publications.

(vi) This dissertation does not contain text, graphics or tables copied and pasted from the Internet, unless specifically acknowledged, and the source being detailed in the dissertation and in the References sections.

Signed: _____________

Acknowledgements

In the time I have spent performing this research, there are a great number of people that deserve my gratitude, but only a fraction that I can list here.

I would like to thank the National Research Foundation for their financial support. My thanks also goes out to the technical staff that have helped me significantly over the years, particularly workshop staff such as Anthony, Dharma, Roland, Greg and Swanie. To the lab crowd of old: Dan, Shivan, Brett, Turck, Pete and Dagwood, you have spent the majority of time with me, I thank you for your patience and for providing me with some of the most entertaining times yet. To the new lab crowd, who are certainly worthy replacements: Wayne, Roland, Darryl and Sergio, for the road trips, lunches and fantastic tea debates. Britney.

To mah Col Crowd [sic], you lot are the most amazing bunch of people on the planet. I thank you for your support and stress-relieving fun times: all Yakka- and taxi-related outings in particular, and I hope there are many more! To running and the running partners, thanks for the getting me onto ultramarathons to keep the head clear!

To my supervisor, Leigh Jarvis, who has been an inspiration to me and provided endless advice and patience throughout this research. I am very grateful for his constant support and motivational efforts, in particular, the free lunches along the way. The result of this is genuine excitement for commencing my PhD future!

Last but certainly not least, to my family for putting up with me and my absurdly strange work schedules. I appreciate how little sleep you have managed over the last few months, and would like to thank you for your unending love and support. I shall do my best to ensure the next time will be far less stressful for you ☺.

Abstract

Magnesium Diboride (MgB_2) bulk superconductor has been manufactured for use in superconducting fault current limiters (SFCLs) via *in situ* reaction. SFCLs have proven to be a viable means for limiting surge currents on power lines by dissipating fault energy as the superconductor quenches. As the current limiting behaviour is determined by the normal resistance (R_n), research has been conducted to evaluate an effective means to increase R_n for bulk superconducting MgB_2. Other researchers have previously looked into the improvement and optimisation of the critical current, J_c, by carbon doping and other flux pinning techniques. Carbon doping has been confirmed as a means to increase R_n, and was implemented by chemical vapour deposition (CVD) at 600 ºC in a tubular furnace apparatus. Intragranular doping was achieved by CVD on the boron precursor powder. *In situ* manufacturing of MgB_2 bulk was performed using the reactive liquid magnesium infiltration technique. Carbon doping provided an adequate increase in R_n, for a small decrease in the critical temperature, T_c.

Selected List of Symbols and Their Units

Roman Letters

A	
a	Crystal lattice parameter (Å)
A	Cross-sectional Area (m^2)
A_p	Magnetic field vector potential
B	
B	Magnetic flux density (T)
B_a	Applied magnetic flux density (T)
B_i	Internal magnetic flux density (T)
B_r	Residual magnetic flux density (T)
C	
C	Crystal lattice parameter (Å)
c	Speed of light (2.998×10^8 $m.s^{-1}$)
C	Euler's constant (0.577)
C_p	Specific heat capacity ($J.kg^{-1}.K^{-1}$)
D	
d	Specimen geometry constant
d	Pin spacing (m)
D	Specimen thickness (m)
D	Diffusivity ($m^2.s^{-1}$)
E	
e	Electron charge (1.6×10^{-19} C)

e^*	$2e$
E	Electric field (V.m^{-1})
E_F	Fermi energy (eV)
E_{kin}	Kinetic energy (J)
E_{mag}	Magnetic energy (J)
F	
f	Frequency (Hz)
f_p	Local pinning force (N)
f_s	Sampling frequency (Hz)
F_L	Lorentz force (N)
F_N	Normalised pinning force density
F_P	Pinning force density (N.m^{-2})
G	
g	Free energy density (J)
g_n	Normal free energy density (J.m^{-3})
g_s	Superconducting free energy density (J.m^{-3})
G	Gibbs free energy (J)
G_0	Total condensation energy (J)
G_n	Gibbs normal free energy (J)
G_s	Gibbs superconducting free energy (J)
H	
h	Local magnetic field (A.m^{-1})
h	Normalise magnetic field
h	Planck's constant (6.6×10^{-34} J.s)
$\hbar$	Reduced Planck constant (1.1×10^{-34} J.s)
H	Magnetic field (A.m^{-1})
H_c	Critical magnetic field (A.m^{-1})
H_{c0}	Critical magnetic field at T = 0 K (A.m^{-1})
H_{c1}	Lower critical magnetic field (A.m^{-1})
H_{c2}	Upper critical magnetic field (A.m^{-1})
H_{irr}	Irreversible magnetic field (A.m^{-1})
H_p	Critical State Model peak magnetic field (A.m^{-1})
I	
I	Current (A)
I_c	Critical current (A)

I_{lim}	Fault current magnitude (A)
J	
J	Current density (A.cm^{-2})
J_{c}	Transport critical supercurrent density (A.cm^{-2})
J_{e}	Engineering critical supercurrent density (A.cm^{-2})
J_{n}	Normal current density (A.cm^{-2})
J_{s}	Superconducting current density (A.cm^{-2})
J_{D}	Depairing current density (A.cm^{-2})
K	
k_{B}	Boltzmann constant (1.4×10^{-23} J.K^{-1})
K	Constant
L	
l_{e}	Electron mean free path (m)
L	Length (m)
M	
m	Effective mass (kg)
m_{e}	Mass of an electron (9.11×10^{-31} kg)
m_{i}	Isotopic mass (kg)
$m*$	$2m_e$
M	Magnetisation (A.m^{-1})
M^+	Magnetisation measured in increasing magnetic field (A.m^{-1})
M^-	Magnetisation measured in decreasing magnetic field (A.m^{-1})
N	
n	Clean/dirty limit parameter
n	Total electron density (#.cm^{-3})
n_{n}	Normal electron density (#.cm^{-3})
n_{s}	Superconducting electron density (#.cm^{-3})
N	Density of states (J^{-1}.m^{-3})
P	
p	Momentum (kg.m.s^{-1})
p	Pinning force scaling parameter
P	Power (W)
Q	
q	Pinning force scaling parameter
R	
r	Distance (m)

R	Resistance (Ω)
R_n	Normal state resistance (Ω)
S	
s_n	Normal entropy density (J.K^{-1}.m^{-3})
s_s	Superconducting entropy density (J.K^{-1}.m^{-3})
S	Entropy (J.K^{-1})
T	
t	Reduced temperature
t	Time (s)
T	Temperature (K)
T_c	Critical Temperature (K)
V	
v	Velocity (m.s^{-1})
v_F	Fermi velocity (m.s^{-1})
v_n	Normal state velocity (m.s^{-1})
v_s	Superconducting state velocity (m.s^{-1})
V	Volume (m^3)
V	Electron-electron attractive interaction
V_0	Electron-electron attractive interaction at T=0 K
V_0	System RMS voltage (V)
X	
x	Distance (m)
Z	
Z	System enthalpy (J)

Greek Letters

α	Bloch-Grüneisen coefficient
α	GL phenomenological parameter
α	Isotope effect coefficient
β	GL phenomenological parameter
β	AC susceptibility phase imbalance (^{o})
β_{c}	Proportional energy gap constant
γ	Anisotropy
γ_{H}	GL magnetic field anisotropy parameter
γ_{λ}	Penetration depth anisotropy
γ_{ξ}	Coherence length anisotropy
γ	Anisotropy
γ_{c}	Critical density
δ	Density (g.cm^{-3})
κ	GL parameter
λ	Coupling constant
λ	Penetration depth (m)
λ_0	Penetration depth at T=0 K (m)
λ_{ep}	Electron-phonon coupling constant
λ_{GL}	GL penetration depth (m)
λ_{L}	London penetration depth (m)
μ	Effective permeability (N.A^{-2})
μ_0	Permeability of free space (1.256×10^{-6} N.A^{-2})
ξ	Coherence length (m)
ξ_0	BCS coherence length (m)
ξ_{GL}	GL coherence length (m)
ξ_{P}	Pippard coherence length (m)
ρ	Resistivity (μΩ.m)
ρ_0	Residual resistivity (μΩ.m)
ρ_{n}	Normal-state resistivity (μΩ.m)
ρ_{ph}	Phonon-related resistivity contribution (μΩ.m)
σ_{ns}	Surface energy (J)
τ	Mean scattering time (s)
φ_{p}	Phase difference
χ_V	Magnetic volume susceptibility
ψ	Wavefunction (m$^{-3/2}$)

ψ_0	Wavefunction at T=0 ($m^{-3/2}$)
ω_D	Debye frequency ($rad.s^{-1}$)
Γ	Brillouin zone center
Δ	Superconducting energy gap (eV)
Δ_0	Superconducting energy gap at T=0 K (eV)
Θ_D	Debye temperature (K)
Φ_0	Magnetic flux quantum (2.068×10^{-15} Wb)

Acronyms

2G	Second generation (HTS)
AC	Alternating current
ADC	Analogue-to-digital converter
BCS	Bardeen, Cooper and Schrieffer
CTFF	Continuous tube forming and filling
CVD	Chemical vapour deposition
DC	Direct current
FAST	Field assisted sintering technique
FCL	Fault current limiter
HEP	High energy physics
HIP	Hot isostatic pressing
HP	High pressure
HTS	High temperature superconductor
ID	Inner diameter
LH2	Liquid hydrogen
LNe	Liquid neon
LN2	Liquid nitrogen
LIA	Lock-in amplifier
LTS	Low temperature superconductor
MG	Microgrid
MgB_2	Magnesium diboride
MLI	Multi-layer insulation
MOCVD	Metalorganic chemical vapour deposition

MRI	Magnetic resonance imaging
NMR	Nuclear magnetic resonance
PCS	Power conditioning system
PIT	Powder-in-tube
RES	Renewable energy sources
RLI	Reactive liquid infiltration
RRR	Residual resistivity ratio
SEM	Scanning electron microscopy
SFCL	Superconducting fault current limiter
SMES	Superconducting magnetic energy storage
SN2	Solid nitrogen
SPS	Spark plasma system
SS	Stainless steel
TIG	Tungsten inert gas
XPS	X-ray photoelectron spectroscopy
XRD	X-ray diffraction

Contents

List of figures

List of tables

Chapter 1 Introduction

The focus of this work was to ascertain if superconducting magnesium diboride (MgB_2) could be effectively used as the current limiting element of a resistive superconducting fault current limiter (SFCL).

Globally, as power demand grows and the use of renewable energy sources increase, it is typically met with an increase in grid complexity and distributed generation, which increases fault current levels and makes them harder to predict [**1**]. The capacity of installed switchgear may no longer be sufficient to support this growth, presenting a need for fault current limiter to reduce the magnitude of fault currents for during the brief time period between fault occurrence and switchgear interruption of the fault current [**2**].

In new substation design, they can be utilised to ensure that the fault current levels are lowered, and thus specifications on equipment installed may be relaxed [**3**]. Fault current limiters may also be integrated into an existing substation, to allow for previously impossible local grid upgrades to be made. An emerging application is at the connection point where an independent power provider, such as a wind farm, ties into the grid [**4**]. Having this increased protection from fault currents facilitates the large scale move to independent power providers connecting into the grid.

Superconductors, by their intrinsic current quenching characteristics, make them particularly suitable for fault current limiter application. A superconductor that is operating at below its critical temperature, T_c, and critical current density, J_c, will be in a superconducting state characterised by zero resistance. Should either temperature increase above T_c or the current density increase above J_c, then the superconductor will transition into a normal (resistive) state, in a process called 'quench'. Thus, a superconducting fault current limiter in the superconducting state will be transparent to the grid and present zero impedance, but under fault conditions the superconductor will immediately quench and present to the grid an impedance determined by the normal resistance, R_{n}, and dissipate fault energy through $P = I^2 R_{\mathrm{n}}$ resistive losses, thus limiting the fault current. Once the fault has been cleared, the FCL can be 'reset' by cooling the superconductor to superconducting state again.

Superconducting fault current limiters may be constructed using different types of superconductors, and there is currently active research in this field by a number of companies. Many companies are developing superconducting fault current limiters using second generation high T_{c} superconductors (2G HTS) due to their high T_{c} and R_{n} values. It is R_{n} that determines the energy dissipated during fault currents, and therefore a high R_{n} is desired for enhanced current limiting properties. Due to the high T_{c} of HTS, the cryogenic requirements to keep the superconductors cool are achievable using inexpensive liquid nitrogen (LN2). Despite being second generation, HTS still require advanced fabrication processes to minimise the grain boundary problems, and are sheathed by expensive materials such as silver.

In comparison to 2G HTS, MgB_2 features grain boundaries that are extremely transparent to current flow [**5**]. As both magnesium and boron have very low densities, superconducting MgB_2 is therefore a lightweight superconductor. In addition, MgB_2 can be fabricated in bulk using very inexpensive processes that yield high quality product, despite the low cost [**6**]. With ever-improving technologies, closed cycle cryogenic refrigerators are sufficiently powerful and inexpensive enough to render operation of MgB_2 in the range of 20 to 30 K for extended durations economically feasible.

A practical problem with the use of MgB_2 in resistive FCLs is the intrinsically low normal resistivity of MgB_2, which limits the minimum length of superconductor that can be used. With a low resistivity, longer lengths of superconductor are required increasing both size and cost. Work has been done to investigate the effect of chemical doping on the superconducting properties of MgB_2, primarily in the form of J_{c} and upper critical field, H_{c2}, and has revealed increases in these parameters up to a certain limit with an increase in disorder due to doping. The approach taken in this research has been to further dope the specimens to substantially increase R_{n}, making it more suitable for use in FCLs whilst still maintaining reasonable operational conditions.

Doping can be achieved by different methods, such as impurity powder addition (such as Al [**7**], C [**8**], SiC [**9**]) prior to reaction, and chemical vapour deposition. Carbon chemical vapour deposition on the precursor powder was the method used in this research, as it intrinsically allows for homogenous doping [**10**].

The metric used in this research to determine the suitability of MgB_2 for FCL operation is an effective increase in R_{n} to decrease the length of superconductor required, and a reasonable decrease in T_{c} that still allows for operation of the FCL in the temperature range of 20 to 30 K. From our research presented in this dissertation, we have established an order of magnitude increase in R_{n} at a modest decrease in T_{c}.

The dissertation is organised as follows:

Chapter 2 introduces a brief history of superconductivity, the different types of superconductors, and some models and theories used to describe superconducting behaviour. The chapter deals with general theory that is fundamental to understanding superconductivity, but can be skipped should the reader be already familiar with these theories.

Chapter 3 discusses the structure and properties of magnesium diboride, the material chosen for this research. The resistivity, critical current and magnetic properties of polycrystalline MgB_2 are detailed, along with the methods of manufacture, some disorder effects, degradation, and possible applications for MgB_2.

Chapter 4 details the experimental work, including the design and manufacture of apparatus that was used in the doping, manufacturing and testing of specimens. The details of the manufacturing and testing procedures that were performed on the MgB_2 specimens are also dealt with in detail.

Chapter 5 presents the results, analysis and interpretation of gathered data from optical and scanning electron microscopy, resistive and AC susceptibility tests.

Chapter 6 concludes and establishes the achievement of the research goal, that the resistivity was significantly improved without a significant decrease in T_c. An outline of future work to be carried out is also mentioned.

Chapter 2 Superconductivity

2.1. Introduction

Superconductivity is a state characterised by zero electrical resistance, perfect diamagnetism and long range quantum order. The route to the discovery of superconductivity began in April 1911 during low temperature electrical resistance tests on pure mercury by Heike Kamerlingh Onnes, where it was found that the resistivity decreased to 'practically zero' [**11**]. In May 1911 he noted the abrupt nature of that decrease, and the fact that it occurred at 4.2 K [**12**]. At first labelled 'supraconductivity', Kamerlingh Onnes soon settled on naming the state 'superconductivity' [**13**]. The temperature at which the material transitions from normal to superconducting state is called the critical temperature, T_c, as shown in the resistivity graph of Figure 2-1.

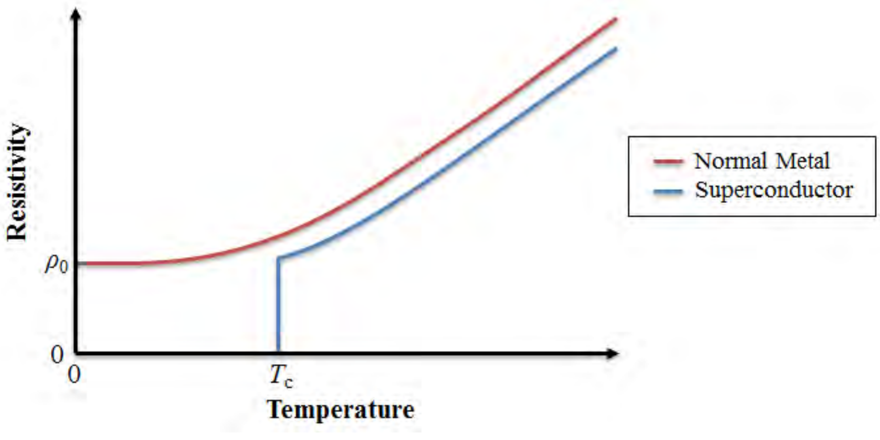

Figure 2-1 Temperature dependence of a normal metal and a superconductor. Below a critical temperature T_c, the resistivity of the superconductor abruptly drops to zero.

The lack of electrical resistivity would describe a perfect conductor, but superconductors also display unique magnetic properties, as they are capable of perfect diamagnetism in weak applied fields. This property was discovered in 1933 by Meissner and Ochsenfeld, many years after the initial discovery of superconductivity, and named the Meissner Effect [**14**]. Perfect diamagnetism describes the ability of a material to completely exclude magnetic flux; an absence of magnetic permeability.

The difference between a superconductor and a perfect conductor is due to the fact that they exhibit very different behaviour in magnetic fields. For the case of the cooling in zero applied field, the perfect conductor and superconductor both maintain a state of zero internal flux, $B_i = 0$, within the bulk as a field B_a is applied and removed. This is shown in Figure 2-2.

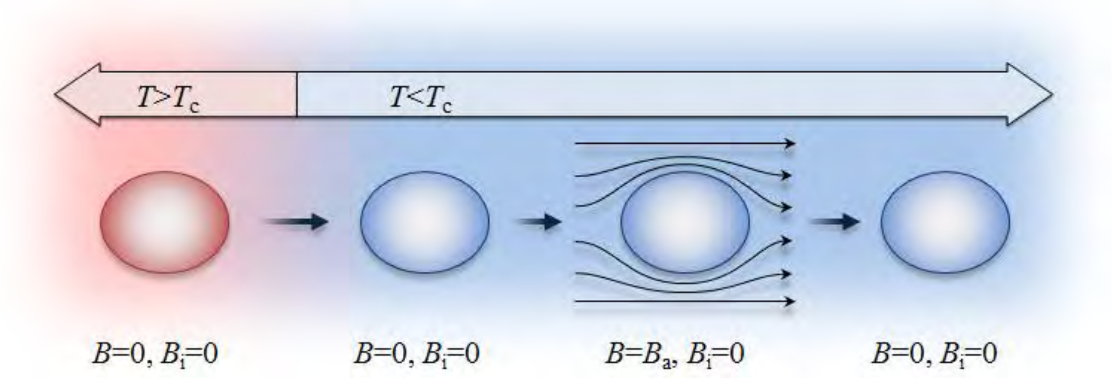

Figure 2-2 Behaviour of both superconductors and perfect conductors in zero-field cooled conditions. Below the transition temperature, a state of zero internal flux is sustained despite changes in the applied field.

The situation changes when cooling in a non-zero applied field, as the superconductor will exclude the flux below T_c, as shown in Figure 2-3, whilst the perfect conductor will maintain the flux density in the bulk, even after the applied field is removed, as shown in Figure 2-4.

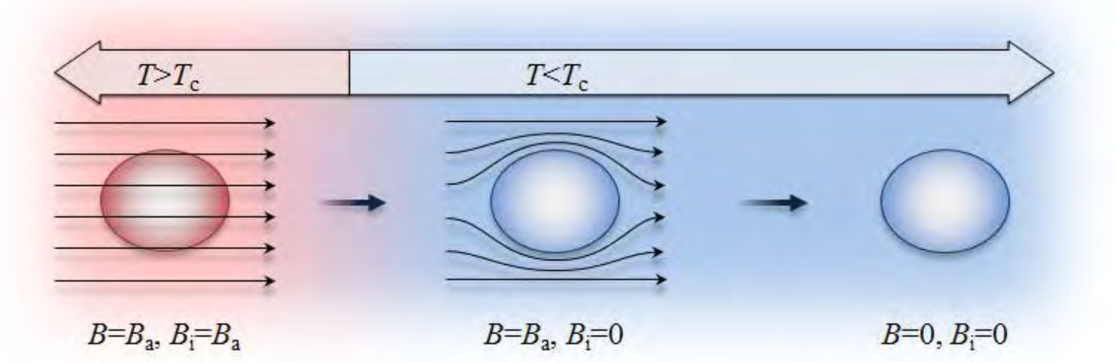

Figure 2-3 Behaviour of superconductors when cooled in an applied field. Although the flux is able to penetrate the bulk above the transition temperature, cooling to below the transition temperature results in the superconductor excluding this field.

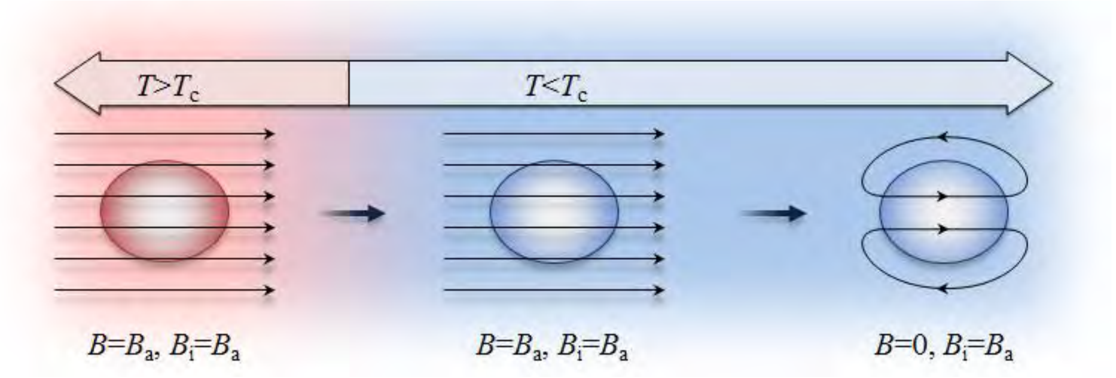

Figure 2-4 Behaviour of perfect conductors when cooled in an applied field. The perfect conductor allows flux to penetrate both above and below the transition temperature, and the non-zero internal flux density is maintained even if the applied field is removed completely.

The superconductor thus ensures that the flux within the bulk is always zero, whilst the perfect conductor ensures that the rate of change of flux within the bulk remain zero. This will be shown later through the London equations in Section 2.2.2.

Alexei Abrikosov predicted in 1957 [**15**] that there existed two distinct groups of superconductor, based on the different magnetisation responses to applied fields. A superconductor can be classified as belonging to one of these groups, dependent on the behaviour exhibited in applied magnetic fields.

Type I superconductors exhibit perfect diamagnetism in an applied magnetic field in the range of zero up to a critical limit H_c, after which the superconductor will transition to the normal, non-superconducting state. Type II superconductors exhibit perfect diamagnetism up to a certain critical applied magnetic field H_{c1}, after which the superconductor enters into a 'mixed-state' as the magnetic field increases to another critical field, H_{c2}, after which superconductivity is destroyed. In the mixed state, there is decreasing partial flux expulsion up to H_{c2}, after which there is zero flux expulsion and the transition to non-superconducting state is complete.

In addition to being confined to certain bounds of operating temperature and magnetic field, the superconductor also has operating limitations on the transport current, where the superconductor has a critical current density limit of J_c. Like H_c, the critical current density has a temperature dependence, and also has a dependence on H_c. The bounds of the superconducting state can visually interpreted as critical surface, as shown in Figure 2-5.

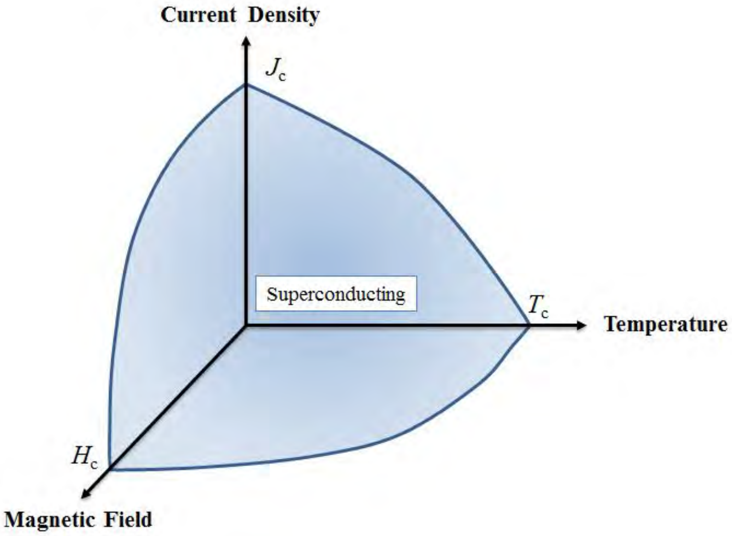

Figure 2-5 Generalised critical surface diagram. The superconducting state is preferred when operating with $T < T_c$, $H < H_c$, and $J < J_c$.

In 1954, Matthias *et al* discovered superconductivity in Nb_3Sn [**16**]. Early on it was found that the critical temperature of this brittle material could be as high as 18.3 K, with an operating field of up to 20 T [**17**]. Recently this upper critical field has been enhanced up to 35.7 T [**18**].

In the same time period, superconductivity was discovered in NbTi by Hulm and Blaugher [**19**]. NbTi has a transition temperature of 9.2 K, and has practical operation at 4.2 K in fields up to 9 T [**20**]. Although having a lower transition temperature and operating in lower fields, NbTi is cheaper than Nb_3Sn and has favourable mechanical properties, so has therefore been the workhorse superconducting material in practical applications, particularly MRI [**21**]. NbTi and Nb_3Sn formed the definition of low temperature superconductors (LTS) before the discovery of cuprate-based superconductors.

The ability of electron pairs to perform tunnelling between two superconductors separated by a thin insulating material was first discovered by Josephson in 1962, and named the DC Josephson Effect [**22**]. The effect is exploited in superconducting quantum interference devices (SQUIDs), which are used in extremely sensitive magnetometers that are able to measure magnetic fields down to the order of the flux quantum, Φ_0, discussed later.

In 1986, Bednorz and Müller made the breakthrough discovery of high temperature superconductors (HTS) which carry supercurrent in copper oxide planes [**23**]. Their discovery was of superconducting LaBaCuO with T_c~35 K, which exceeded the previously determined theoretical maximum critical temperature of superconductors by 'BCS' theory, as discussed in Section 2.2.5. This class of cuprate-based superconductors was therefore not defined by existing theory, and therefore the upper limit for critical temperature clearly did not apply, and the discovery earned Bednorz and Müller the Nobel Prize in Physics in 1987.

In 1987, Wu *et al*, discovered superconductivity in YBCO with $T_\mathrm{c} = 93$ K, becoming the first superconductor to have a critical temperature above the 77 K boiling point of liquid nitrogen [**24**]. This had major commercial implications, as the cryogenic systems required for superconductivity could be significantly reduced, and expensive liquid cryogens such as liquid helium would no longer be required.

HTS superconductors are electrically anisotropic, which presents significant manufacturing challenges when producing both superconducting wires and bulk pieces. The anisotropic nature results the fact that supercurrent is carried in 2-dimensional copper oxide planes, the overall current transport properties thus vary depending on the crystallographic orientation. Complex process and fabrication techniques are thus required to maximise the superconducting properties, specifically to ensure the grain orientation is optimal, to minimise grain boundary (GB) problems.

The GB is the interface between superconducting crystal grains in a polycrystalline superconductor bulk. The properties of the GBs determine the critical current density, J_c, due to the fact that these GBs form resistive paths that impede the flow of supercurrent, suppressing J_c.

In 2001, magnesium diboride, a well-known compound, was found to superconduct below $T_\mathrm{c} = 39$ K by Akimitsu *et al* [**25**, **26**]. This breakthrough discovery established the material as having the highest critical temperature of any 'BCS' superconductor. Both HTS and MgB_2 have layered structures, but MgB_2 is a metallic conductor at room temperature. MgB_2 also contains two superconducting energy gaps, as theoretically predicted in 2001 [**27**], and later confirmed by a number of experiments 2003 [**28**]. MgB_2 offers economic benefits compared with HTS: sheathed HTS tapes can be as much as 70% Ag by volume [**29**] whereas MgB_2 can be sheathed with many inexpensive materials.

Superconductors frequently find application in scenarios where high currents and/or high magnetic fields are required, such as medical Magnetic Resonance Imaging (MRI) machines, Nuclear Magnetic Resonance (NMR) imaging and spectroscopy, magnetic levitation for transportation, and particle accelerators.

2.2. Summary of theories

Following the discovery of superconductivity, research to explain the physical mechanisms was undertaken, but despite a number of active researchers in the field, there were no adequate theories developed for a number of decades.

The first theoretical milestone was the theory of the London brothers in 1935, and was the first theory to explain the Meissner effect and lossless current transport. The phenomenological-based London theory did not, however, explain the microscopic reasons for superconductivity. The concept of the London penetration depth was introduced: the non-zero depth to which a magnetic field will penetrate a superconductor.

The phenomenological Ginzburg-Landau theory introduced the quantum nature of superconductivity which lead to the prediction of flux quantisation, and led to the distinction of Type II superconductivity.

The microscopic theory of Bardeen, Cooper and Shrieffer (BCS) provides the greatest insight into the mechanism of superconductivity, and is based on electron-pairing, when two electrons experience an attractive force they form Cooper pairs. Cooper pairs obey Bose–Einstein statistics, thereby circumventing the Pauli Exclusion Principle that applies to electrons (which are Fermions), permitting the description of all charge carriers by one macroscopic wave function. In contrast, both the London and GL theories were both developed without the knowledge of coupled electrons.

2.2.1. Second Order Transition

In the absence of magnetic field, the transition from normal to superconducting state is a second order transition, as the entropy is continuous at the transition point. Lev Landau formulated a general theory of second order phase transitions that was fundamental to the development of Ginzburg-Landau theory [**30**, **31**]. Below T_c, the superconducting state is preferred, and thus must be a lower energy state than the normal state at these temperatures.

The Gibbs free energy, developed by Josiah Willard Gibbs in the 1870's [**32**], is defined as

$$G(p,T) = Z - TS, \tag{2.1}$$

where Z is the system enthalpy[†], T is the temperature of the system, and S is the entropy of the system. A suitable form for superconductivity would be to define the Gibbs free energy in terms of the applied magnetic field, H, and the temperature T, as an increase in either quantity could prompt a change from superconducting to normal state. In this form, the superconducting state would be the lower energy state for when both $T < T_c$ and $H < H_c$ for Type I superconductors, or when both $T < T_c$ and $H < H_{c2}$ for Type II superconductors. In order for a change between superconducting and normal phase to occur, the Gibbs free energy of both the superconducting state, G_s, and the normal state, G_n, should be equal at the transition condition, i.e.: at a field of $H = H_\mathrm{c}$, we have

$$G_\mathrm{s}(H_\mathrm{c},T) = G_\mathrm{n}(H_\mathrm{c},T). \tag{2.2}$$

The magnetic volume susceptibility, χ_v, and magnetic flux density, B, are defined by the relationships

$$\chi_\mathrm{v} = \frac{M}{H}, \tag{2.3}$$

$$B = \mu_0(H+M) = \mu_0(1+\chi_\mathrm{v})H, \tag{2.4}$$

where M is the magnetisation, and μ_0 is the permeability of free space. The magnetic permeability can thus be expressed as

$$\mu = \mu_0(1+\chi_\mathrm{v}). \tag{2.5}$$

[†] The system enthalpy is usually denoted as *H*, but has been changed to *Z* to avoid possible confusion with magnetic field.

In the Meissner state with perfect diamagnetism, the susceptibility $\chi_{\mathrm{v}} = -1$, which results in an effective permeability of $\mu = 0$, so no magnetic field penetrates the superconductor. As the applied magnetic field is increased from zero to H_c, the Gibbs free energy undergoes a corresponding change as the magnetic energy of the superconducting state increases as

$$G_{\mathrm{s}}(H_{\mathrm{c}}, T) = G_{\mathrm{s}}(0, T) - \int_0^{H_{\mathrm{c}}} \mu_0 M dH. \tag{2.6}$$

Since in the superconducting state $\chi_{\mathrm{v}} = -1$, $M = -H$, Equation (2.6 becomes

$$G_{\mathrm{s}}(H_{\mathrm{c}}, T) = G_{s}(0, T) + \frac{\mu_0 H_{\mathrm{c}}^2}{2}. \tag{2.7}$$

In the normal state, neglecting the typically small magnetic susceptibility, the Gibbs free energy is no different at H_c, than at zero applied field, so thus

$$G_{\mathrm{n}}(H_{\mathrm{c}}, T) = G_{\mathrm{n}}(0, T). \tag{2.8}$$

Combining Equation (2.2, Equation (2.7 and Equation (2.8 we obtain the condensation energy:

$$G_{\mathrm{n}}(0, T) - G_{\mathrm{s}}(0, T) = \frac{\mu_0 H_{\mathrm{c}}^2}{2}. \tag{2.9}$$

So the difference in Gibbs free energy is simply the energy required to exclude the applied magnetic field from the superconductor. For Type II superconductors, the difference is given by

$$G_{\mathrm{n}}(0, T) - G_{\mathrm{s}}(0, T) = -\int_0^{H_{\mathrm{c2}}} \mu_0 f(H) dH, \tag{2.10}$$

where $f(H)$ represents the nonlinear magnetisation curve.

Experimentally it has been shown that the H_{c} of Type I superconductors have an approximate temperature dependence relationship of

$$H_{\mathrm{c}}(T) = H_{\mathrm{c0}}\left[1 - \left(\frac{T}{T_{\mathrm{c}}}\right)^2\right], \tag{2.11}$$

within the superconducting state of $T \leq T_{\mathrm{c}}$, as shown in Figure 2-6.

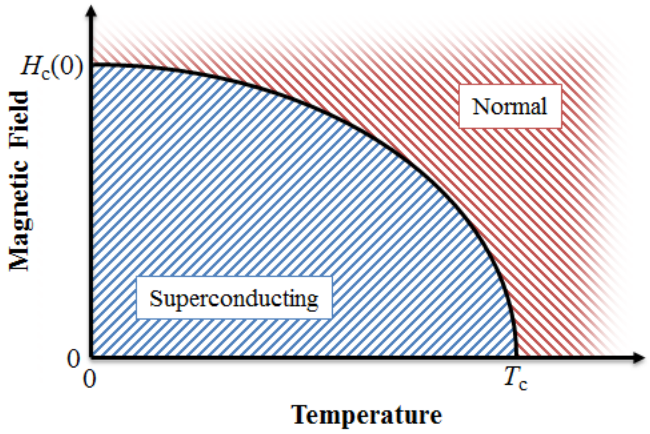

Figure 2-6 Experimental temperature dependence of the critical field for Type I superconductors.

Using the entropy relationship, $S_{\mathrm{n}}(0,T) = -\left(\frac{\partial G}{\partial T}\right)_H$, the entropy can be expressed as

$$S_{\mathrm{n}}(0,T) - S_{\mathrm{s}}(0,T) = \mu_0 H_{\mathrm{c}}(T)\frac{dH_{\mathrm{c}}(T)}{dT}. \tag{2.12}$$

From Figure 2-6, it is clear that as $T \to T_{\mathrm{c}}$, $H_{\mathrm{c}} \to 0$, so as $T \to T_{\mathrm{c}}$, the right-hand-side of Equation (2.12 becomes zero, and thus $S_{\mathrm{n}}(T_{\mathrm{c}}) = S_{\mathrm{s}}(T_{\mathrm{c}})$. This implies second order continuity at the transition temperature, and hence Landau's second-order transition theory can be applied.

2.2.2. The London Equations

The London equations are a set of equations developed by brothers Fritz and Heinz London in 1935, and describe the electrodynamics of superconductivity on a macroscopic scale [**33**]. Specifically, they relate the current and electromagnetic behaviours in superconductors, with explanations for the Meissner effect and zero resistance.

The Two-Fluid Model

The electrons in a superconductor can be described by a two fluid model, with one fluid consisting of 'normal' electrons, and the other fluid consisting of superconducting electrons, 'superelectrons'. The normal electrons have a density n_{n}, drift velocity $\vec{v}_{\mathrm{n}}$, and behave the same as conventional free electrons in any normal metal. Any applied electric field $\vec{E}$ will accelerate the normal electrons, but the scattering due to defects in the ion lattice, impurities, and thermal phonons, electrons will be limited to a mean drift velocity

$$\langle \vec{v}_{\mathrm{n}} \rangle = -\frac{e\tau}{m}\vec{E}, \tag{2.13}$$

with e the charge of an electron, τ the mean time between scattering events, and m the mass of an electron. The normal current flow of these electrons is thus

$$\vec{J}_{\mathrm{n}} = -n_{\mathrm{n}} e \langle \vec{v}_{\mathrm{n}} \rangle = \frac{n_{\mathrm{n}} e^2 \tau}{m}\vec{E}. \tag{2.14}$$

For the case of the superelectrons with density n_{s} and drift velocity $\vec{v}_{\mathrm{s}}$, they do not encounter any scattering, and hence the electric field produces an acceleration:

$$m\frac{d\vec{v}_{\mathrm{s}}}{dt} = -e\vec{E}, \tag{2.15}$$

and the supercurrent flow is thus

$$\vec{J}_{\mathrm{s}} = -n_{\mathrm{s}} e \vec{v}_{\mathrm{s}}. \tag{2.16}$$

Differentiation of Equation (2.16, and combining with Equation (2.15 yields the expression

$$\frac{\partial \vec{J}_{\mathrm{s}}}{\partial t} = n_{\mathrm{s}} e \frac{\partial \vec{v}_{\mathrm{s}}}{\partial t} = \frac{n_{\mathrm{s}} e^2}{m}\vec{E}. \tag{2.17}$$

This is known as London's first equation, and shows that the supercurrent will continue to increase due to the acceleration from the electric field and the lack of scattering. This contradicts Ohm's law, as it shows that it is $\frac{\partial \vec{J}_\mathrm{s}}{\partial t}$ rather than $\vec{J}_\mathrm{s}$ that is proportional to the applied electric field $\vec{E}$, indicating an inductive relationship. For the case of a steady current flow, $\frac{\partial \vec{J}_\mathrm{s}}{\partial t} = 0$ and hence the electric field is zero, and thus the normal current flow will be zero. All of the current is carried by the supercurrent without developing a potential difference, and so the superconductor has zero resistance. Thus we have $\vec{J} = \vec{J}_\mathrm{s}$, and a description of the lossless transport of DC current.

Using the Maxwell equation

$$\nabla \times \vec{E} = -\frac{\partial \vec{B}}{\partial t}, \tag{2.18}$$

and combining with the curl of the first London equation,

$$\frac{\partial}{\partial t}\left(\nabla \times \vec{J}_\mathrm{s}\right) = \frac{n_\mathrm{s} e^2}{m}\left(\nabla \times \vec{E}\right), \tag{2.19}$$

we obtain

$$\frac{\partial}{\partial t}\left(\nabla \times \vec{J} + \frac{n_\mathrm{s} e^2}{m}\vec{B}\right) = 0, \tag{2.20}$$

which describes perfect conductors, where $\frac{\partial \vec{B}}{\partial t} = 0$. For application to superconductors, it was necessary to add an additional restriction Equation (2.20 to describe the Meissner effect, $B = 0$, which is obtained by integrating, giving

$$\nabla \times \vec{J} + \frac{n_\mathrm{s} e^2}{m}\vec{B} = 0, \tag{2.21}$$

the second London equation.

The Ampère-Maxwell law with negligible electric displacement field and susceptibility can be expressed as $\vec{J} = \frac{\nabla \times \vec{B}}{\mu_0}$, and substituted into Equation (2.21 to obtain

$$\frac{\nabla \times \nabla \times \vec{B}}{\mu_0} + \frac{n_\mathrm{s} e^2}{m}\vec{B} = 0, \tag{2.22}$$

$$\nabla \times \nabla \times \vec{B} = \frac{\mu_0 n_\mathrm{s} e^2}{m} B. \tag{2.23}$$

Recalling the identity $\nabla \times \nabla \times \vec{A} = \nabla(\nabla . \vec{A}) - \nabla^2 \vec{A}$, Equation (2.23 can be expressed as

$$\nabla \times \nabla \times \vec{B} = -\frac{1}{\lambda_\mathrm{L}^2}\vec{B} = \nabla\left(\nabla . \vec{B}\right) - \nabla^2 \vec{B}, \tag{2.24}$$

and since $\nabla . \vec{B} = 0$, we obtain

$$\nabla^2 \vec{B} = \frac{1}{\lambda_\mathrm{L}^2}\vec{B}, \tag{2.25}$$

where λ_L is known as the London penetration depth, defined as

$$\lambda_\mathrm{L} = \left(\frac{m}{\mu_0 n_\mathrm{s} e^2}\right)^{1/2}. \tag{2.26}$$

From looking at Equation (2.25, it can be seen that for any spatially uniform field with $\nabla^2\vec{B} = 0$, $\vec{B}$ would then also have to be zero everywhere; any non-zero $\vec{B}$ would give a non-zero $\nabla^2\vec{B}$ implying a spatially dependent $\vec{B}$, which is contrasted with the case of the perfect conductor.

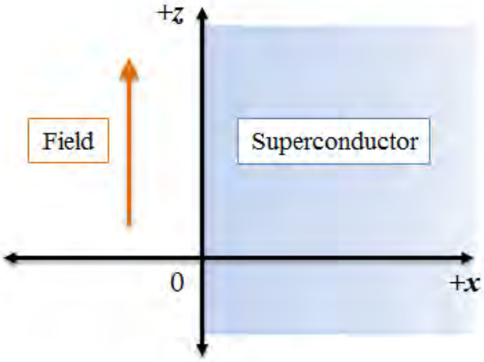

Figure 2-7 The boundary between a superconductor existing in the positive *x*-direction, and an applied magnetic field in the *z*-direction.

Looking at a simple geometrical case of a superconductor in a magnetic field oriented in the *z*-direction of the magnetic field, and existing only for $x > 0$ as shown in Figure 2-7, the magnetic field should only have a *z*-direction component, thus we can simplify Equation (2.25 to one-dimension to obtain

$$\vec{B}_{\mathrm{z}}(x) = -\frac{1}{\lambda_{\mathrm{L}}^2}\frac{d^2\vec{B}_{\mathrm{z}}(0)}{dx^2}. \tag{2.27}$$

The reference solution for such a differential equation is of the form

$$\vec{B}_{\mathrm{z}}(x) = \alpha B_{z0}e^{\frac{-x}{\lambda_{\mathrm{L}}}} + \beta B_{z0}e^{\frac{x}{\lambda_{\mathrm{L}}}}. \tag{2.28}$$

For the physical restraint that the flux shouldn't exponentially increase further away from the interface, we set $\beta = 0$ and obtain the solution

$$\vec{B}_{\mathrm{z}}(x) = B_{z0}e^{\frac{-x}{\lambda_{\mathrm{L}}}}, \tag{2.29}$$

with a corresponding screening current density in the *y*-direction given by:

$$\vec{J}_y(x) = J_{y0}e^{\frac{-x}{\lambda_{\mathrm{L}}}}. \tag{2.30}$$

Equation (2.29) observes that an applied external magnetic field penetrates the surface of the superconductor, and undergoes an exponential decay to zero within the bulk, thus describing the Meissner effect. The characteristic London depth parameter determines the flux penetration depth, as well as the screening current density penetration, as shown for the magnetic field penetration in Figure 2-8.

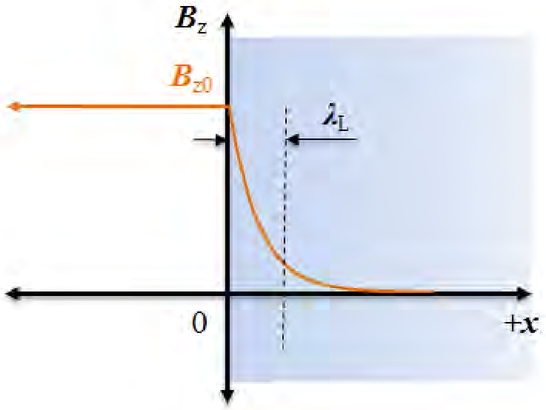

Figure 2-8 Field profile at the boundary surface of a superconductor in an applied magnetic field. The magnetic penetration decays exponentially to a depth determined by the London penetration depth λ_L.

Since the penetration depth is dependent on the density of superelectrons, which is a function of temperature, the penetration depth is also then temperature dependent, empirically described by

$$\lambda_{\mathrm{L}}(T) \approx \frac{\lambda_{\mathrm{L}}(0)}{\left[1-\left(\frac{T}{T_{\mathrm{c}}}\right)^{4}\right]^{1/2}}, \tag{2.31}$$

revealing that the penetration depth tends towards infinity as the temperatures reaches T_{c}. It is important to note that this was not a direct consequence of London theory, but rather from experimental observations. Interestingly, GL theory later establishes this result theoretically, as discussed in Section 2.2.4.

Coherence length

In London theory, there is only one characteristic length, the penetration depth, which came from relating the supercurrent density at a point to the magnetic vector potential at that point. Before electron pairing mechanisms were discovered, Pippard in 1953 found that this local approach was insufficient to describe the experimentally observed penetrations of some Type I superconductors [**34**]. He introduced the Pippard coherence length ξ_{p} that describes the length over which the supercurrent is not largely affected by the spatially-varying magnetic field. This is obtained by evaluating the influence on the supercurrent density at a point from the neighbouring magnetic vector potentials; this is distinctly a non-local approach.

Using the Heisenberg uncertainty principle, $\Delta p \Delta x \gtrsim \hbar$, he was able to establish that for an momentum range of electrons in superconducting state, $\Delta p \approx k_{\mathrm{B}}T_{\mathrm{c}}/v_{\mathrm{F}}$, the length could be estimated as

$$\Delta x \gtrsim \frac{\hbar}{\Delta p} \approx \frac{\hbar v_{\mathrm{F}}}{k_{\mathrm{B}}T_{\mathrm{c}}}, \tag{2.32}$$

where $\hbar$ is the reduced Planck constant, v_{F} is the Fermi velocity, and k_{B} is the Boltzmann constant. Later, BCS theory would establish the coherence length as

$$\xi_0 = \frac{\hbar v_{\mathrm{F}}}{\pi \Delta_0}, \tag{2.33}$$

where $\Delta_0 \approx k_{\mathrm{B}} T_{\mathrm{c}}$ represents the BCS energy gap at $T = 0$ K, as discussed later in Section 2.2.5. This shows that the coherence length of the superconductor can be determined by measurement of the energy gap.

The Pippard coherence length was found to have an order of $\xi_{\mathrm{p}} \approx 10^{-6}$ m, and could be related to the BCS coherence as

$$\frac{1}{\xi_{\mathrm{p}}} = \frac{1}{\xi_0} + \frac{1}{\alpha l_{\mathrm{e}}}, \tag{2.34}$$

with α a unity-order constant, and l_{e} representing the mean free path length of electrons. Here, a decrease in the electron mean free path due to scattering from ions and impurities reduces the coherence length, as could be expected moving towards the dirty limit $\xi_0 >> l_{\mathrm{e}}$. Interestingly, there is an appreciable increase in the penetration depth as ξ_0 becomes more than l_{e}, effectively allowing for Type II response form a Type I superconductor under certain substitutional modifications.

Pippard's modifications were to solve experimental disagreements with Type I superconductors, which is the case when $\xi_0 \gg \lambda$. For type II superconductors, where $\lambda \gg \xi_0$, these modifications are not necessary, and the London equations alone provide a good description of the magnetic penetration depth at the superconductor boundary.

2.2.3. Free energy in the London model

The free energy of a superconductor with a current density J and local magnetic field h can be expressed as the summation of the volume integral of the superconducting energy along with the kinetic and magnetic energy:

$$G = \int G_{\mathrm{s}}(\vec{r}) d^3\vec{r} + E_{\mathrm{kin}} + E_{\mathrm{mag}}. \tag{2.35}$$

Here, E_{kin} represents the kinetic energy from the supercurrent, and E_{mag} the magnetic energy. From the definition of the supercurrent, and with substitution from the London penetration depth, the kinetic energy and magnetic energy can respectively be expressed as:

$$E_{\mathrm{kin}} = \int \frac{1}{2} m_{\mathrm{e}} n_{\mathrm{s}} \vec{v}_{\mathrm{s}}(\vec{r}) d^3\vec{r} = \frac{\mu_0}{2} \int \lambda_{\mathrm{L}}^2 \vec{J}^2(\vec{r}) d^3\vec{r}, \tag{2.36}$$

$$E_{\mathrm{mag}} = \frac{\mu_0}{2} \int \vec{h}^2(\vec{r}) d^3\vec{r}. \tag{2.37}$$

Substitution back into the free energy Equation (2.35, yields

$$G = \int d^3\vec{r} \left[G_{\mathrm{s}}(\vec{r}) + \frac{\mu_0}{2} \lambda_{\mathrm{L}}^2 \vec{J}^2(\vec{r}) + \frac{\mu_0}{2} \vec{h}^2(\vec{r}) \right], \tag{2.38}$$

and with the use of Maxwell's equation, $\vec{J}(\vec{r}) = \nabla \times \vec{h}(\vec{r})$, the above can be simplified to

$$G = G_0 + \frac{\mu_0}{2}\int d^3\vec{r}\left[\lambda_{\mathrm{L}}^2\left(\nabla \times \vec{h}(\vec{r})\right)^2 + \vec{h}^2(\vec{r})\right], \tag{2.39}$$

where G_0 is the total condensation energy, and the first and second terms in the square brackets still represent the current and magnetic contributions respectively. Minimisation of bracketed terms with respect to the local magnetic field leads to the same equation derived by London from electrodynamics:

$$\vec{h}(\vec{r}) + \lambda_{\mathrm{L}}^2\left[\nabla \times \nabla \times \vec{h}(\vec{r})\right] = 0. \tag{2.40}$$

So assuming no change in the number of electrons participating in superconductivity, the London equation represents the field distribution responsible for minimisation of the supercurrent and magnetic contributions.

2.2.4. The Ginzburg-Landau theory

With London theory lacking consideration of quantum effects, it was the phenomenologically-based theory of Ginzburg and Landau that first introduced these effects [**35**]. In their 1950 paper, they asserted that London theory was unable to determine the surface energy at the normal-superconductor phase interface, as well as being unable to describe the destruction of superconductivity with increased current and magnetic fields.

Their theory – commonly known as GL theory – is based on electrodynamics, quantum mechanics and thermodynamics – particularly on Landau's second order transition. The theory provides an effective means to deal with spatial inhomogeneities such as those encountered in Type II superconductors in the mixed state. GL theory predicts Type II superconducting behaviour and quantisation of magnetic vortices.

The theory introduces the superconducting order parameter ψ, which represents an average of the wave functions of the electrons. GL theory uses the two fluid model, so it follows that the wave function should be related to the number of superconducting electrons, and was originally set such that the absolute square of the order parameter was equal to the density of superconducting electrons, $|\psi|^2 = n_{\mathrm{s}}$, but later normalised to the number of superconducting pairs, $|\psi|^2 = \frac{n_{\mathrm{s}}}{2}$. The complex order parameter is expressed as

$$\psi(\vec{r}) = |\psi(\vec{r})|e^{i\varphi_{\mathrm{p}}(\vec{r})}, \tag{2.41}$$

which, because of the linking to the density of superconducting electrons, is finite below T_{c} and zero above T_{c}, whist the phase term $\varphi_{\mathrm{p}}(\vec{r})$ is related to the current.

The basic idea postulate behind GL theory is that near the second order phase transition, the order parameter is small, and has a slow spatial variation. For the case where ψ is constant, and in the absence of magnetic field, the free energy should depend solely on the density of superconducting electrons. So with a power series expansion for the order parameter, the free energy can be expressed as

$$G_{\mathrm{s}}(\vec{r},T) = G_{\mathrm{n}}(\vec{r},T) + \alpha|\psi|^2 + \frac{\beta}{2}|\psi|^4, \tag{2.42}$$

where $\alpha = a(T - T_{\mathrm{c}})$ which is positive only the normal state, and where $\beta > 0$. The first term simply represents the normal state free energy, whilst the second and third terms form the power series expansion. After considering the current and magnetic field contributions, the final free energy density and total free energy can be expressed respectively as:

$$G_{\mathrm{s}}(\vec{r},T) = G_{\mathrm{n}}(\vec{r},T) + \alpha|\psi|^2 + \frac{\beta}{2}|\psi|^4 + \frac{1}{2m_{\mathrm{e}}^*}\left|\left(-i\hbar\nabla - e^*\vec{A}_{\mathrm{p}}\right)\right|^2 + \frac{\mu_0\vec{h}^2}{2}, \tag{2.43}$$

$$G_{\mathrm{s}}(T) = \int G_{\mathrm{s}}(\vec{r},T)d^3\vec{r}, \tag{2.44}$$

where $m_{\mathrm{e}}^* = 2m_{\mathrm{e}}, e^* = 2e$, and $\vec{A}_{\mathrm{p}}$ is the magnetic field vector potential ($\mu_0\vec{h} = \nabla \times \vec{A}_{\mathrm{p}}$). The fourth term of Equation (2.43 describes the kinetic energy of electrons due to current flow, whilst the fifth term represents the magnetic energy. By substituting the magnitude and phase components of the complex order parameter, we obtain

$$G_{\mathrm{s}}(\vec{r},T) = G_{\mathrm{n}}(\vec{r},T) + \alpha|\psi|^2 + \frac{\beta}{2}|\psi|^4 + \frac{\hbar}{2m_e^*}(\nabla|\psi|)^2 + \frac{1}{2}|\psi|^2 m_{\mathrm{e}}^*\vec{v}_{\mathrm{s}}^2 + \frac{\mu_0\vec{h}^2(\vec{r})}{2}, \tag{2.45}$$

with $\vec{v}_{\mathrm{s}}$ defined as

$$\vec{v}_{\mathrm{s}} = \frac{1}{2m_{\mathrm{e}}^*}\left(\hbar\nabla\varphi_{\mathrm{p}} - e^*\vec{A}_{\mathrm{p}}\right). \tag{2.46}$$

By minimisation of the equation with respect to ψ and $\vec{A}_{\mathrm{p}}$, we obtain the two Ginzburg-Landau equations:

$$\alpha\psi + \beta|\psi|^2\psi + \frac{1}{2m_{\mathrm{e}}^*}\left(-i\hbar\nabla - e^*\vec{A}_{\mathrm{p}}\right)^2\psi = 0, \tag{2.47}$$

$$\vec{J} = \nabla \times \vec{h} = \frac{e^*}{m_{\mathrm{e}}^*}\left[\psi^*\left(-i\hbar\nabla - e^*\vec{A}_{\mathrm{p}}\right)\psi\right]. \tag{2.48}$$

The first GL equation describes the order parameter, whilst the second GL equation describes the current. Many other superconducting parameters may be established from these two equations, and some are outlined in the following subsections.

Thermodynamic critical field

Recalling Equation (2.42), where the free energy in the absence of currents and magnetic field was shown to be the normal state free energy, plus the power series contribution from the superconducting electrons. The difference between superconducting and normal state free energy is clearly just the power series expansion of the order parameter:

$$G_{\mathrm{s}}(\psi,T) - G_{\mathrm{n}}(\psi,T) = G(\psi,T) = \alpha(T)|\psi|^2 + \frac{\beta}{2}|\psi|^4. \tag{2.49}$$

Minimisation with respect to $|\psi|^2$, the number of superconducting pairs, we obtain

$$\frac{dG(\psi,T)}{d|\psi|^2} = \alpha(T) + \beta|\psi|^2 = 0, \tag{2.50}$$

and hence the order parameter can be expressed as:

$$|\psi|^2 = -\frac{\alpha(T)}{\beta}. \tag{2.51}$$

The substitution of this back into Equation (2.42) yields

$$G_{\mathrm{s}} - G_{\mathrm{n}} = -\frac{\alpha^2(T)}{2\beta} = \frac{\mu_0 H_{\mathrm{c}}^2}{2}, \tag{2.52}$$

so the difference in free energy density in the absence of current and magnetic field is simply determined by the magnitude of the critical magnetic field.

Penetration Depth

In small magnetic fields, and treating the order parameter as being uniform, the second GL equation simplifies to

$$\vec{J} = \nabla \times \vec{h} = -\frac{e^{*2}|\psi|^2}{m_{\mathrm{e}}^*}\vec{A}_{\mathrm{p}}, \tag{2.53}$$

and substituting $\vec{h} = \nabla \times \vec{A}_{\mathrm{p}}$, in a similar manner to London we obtain

$$\nabla \times \nabla \times \vec{A}_{\mathrm{p}} = -\frac{e^{*2}|\psi|^2}{m_{\mathrm{e}}^*}\vec{A}_{\mathrm{p}} = \frac{1}{\lambda^2}\vec{A}_{\mathrm{p}}, \tag{2.54}$$

$$\lambda^2 = \frac{m_{\mathrm{e}}^*}{\mu_0 e^{*2}|\psi|^2}. \tag{2.55}$$

This is an expression of the penetration depth, but since $|\psi|^2$ is dependent on $\alpha(T)$, the penetration depth is now a function of temperature, in contrast to London theory. The penetration depth has a temperature relationship near T_{c} defined by

$$\lambda^2 \propto \frac{1}{T_{\mathrm{c}} - T}. \tag{2.56}$$

Coherence Length

Like the Pippard coherence length that defines the length scale for largely unchanged current flow, there exists a coherence length for GL theory, ξ_{GL}, that determines the length scale over which the order parameter varies from zero to maximum. In the absence of magnetic field, the first GL equation can be simplified to:

$$\left(-\frac{\hbar^2}{2m_{\mathrm{e}}^*}\right)\nabla^2\psi + \alpha\psi + \beta|\psi|^2\psi = 0, \tag{2.57}$$

which in the one-dimensional case becomes

$$\left(-\frac{\hbar^2}{2m_{\mathrm{e}}^*}\right)\frac{d^2\psi}{dx^2} + \alpha\psi + \beta|\psi|^2\psi = 0, \tag{2.58}$$

and has a corresponding physical solution of

$$\psi = \psi_0 \left[1 - \exp\left(-\frac{\sqrt{2}x}{\xi_{\mathrm{GL}}(T)}\right)\right]. \tag{2.59}$$

The coherence length can thus be defined as

$$\xi_{\mathrm{GL}}^2(T) = \frac{\hbar^2}{2m_{\mathrm{e}}^*|\alpha|}. \tag{2.60}$$

It is clear from Equation (2.59) that the order parameter follows an exponential law across the coherence length.

Depairing current density

As mentioned in Section 2.1, the superconducting state is favoured below a critical surface bound by T_{c}, H_{c}, and J_{c}. There exists a fundamental upper limit of critical current that may be achieved in a given superconducting material. This limit may be approached as all other limiting factors are circumvented, and is set by the size of the superconducting energy gap. As the current density is increased, the kinetic energy of superconducting charge carriers will eventually exceed the binding energy of the Cooper pairs (discussed in Section 2.2.5), after which it becomes energetically favourable for pairs to split. This limit is called the depairing current density, $J_{\mathrm{d}}^{\mathrm{GL}}$, and is given by

$$J_{\mathrm{d}}^{\mathrm{GL}} = \frac{\phi_0}{3\sqrt{3}\pi\lambda^2\xi\mu_0}. \tag{2.61}$$

Achieving this limit is effectively just a practical design and manufacturing issue, and typically J_{c} values fall short of this limit considerably, but continual research results in consistent improvements of the current densities.

Other important relations

One of the most important relations to emerge from GL theory is the GL parameter, κ, which is the ratio of the penetration depth to coherence length:

$$\kappa = \frac{\lambda}{\xi_{\mathrm{GL}}}. \tag{2.62}$$

It is not temperature dependent, as both the penetration depth and coherence length have the same temperature dependence of $(T_{\mathrm{c}} - T)^{-1/2}$ as $T \to T_{\mathrm{c}}$. The GL parameter reflects the fundamental superconducting characteristic of the material, and led to the easy distinction between the two types of superconductors. Dependent on the value of the GL parameter, materials can be Type I ($\kappa < \frac{1}{\sqrt{2}}$) or Type II ($\kappa > \frac{1}{\sqrt{2}}$) near T_{c}. The GL parameter is also related to the thermodynamic critical field at which superconductivity is destroyed,

$$\kappa = \frac{2\sqrt{2}e}{\hbar} H_{\mathrm{c}}\lambda^2. \tag{2.63}$$

The α and β parameters can be related to parameters that can be determined experimentally, namely the thermodynamic critical field and the penetration depth

$$\alpha = -\left(\frac{e^{*2}}{m_{\mathrm{e}}^{*}}\right)\mu_0^2 H_c^2 \lambda^2, \tag{2.64}$$

$$\beta = -\left(\frac{e^{*2}}{m_{\mathrm{e}}^{*}}\right)^2 \mu_0^3 H_c^2 \lambda^4 \tag{2.65}$$

Another interesting relationship is the combination of the critical field, penetration depth and coherence length expressions of Equation (2.52, Equation (2.55 Equation (2.60 to yield

$$H_{\mathrm{c}}(T)\lambda(T)\xi(T) = C = \frac{\hbar}{e^{*}\mu_0\sqrt{2}} = \frac{\Phi_0}{2\pi\mu_0\sqrt{2}}, \tag{2.66}$$

where C is a constant, and $\Phi_0 = \frac{hc}{e^{*}}$ defines the flux quantum. So despite the temperature dependencies of the critical field, penetration depth and coherence length, the product of the three is a constant. Furthermore, this value of C is defined only in terms of physical constants; there is no dependence on the material properties.

Finally, for Type II superconductors with $\kappa \gg 1$, the upper and lower critical fields can be expressed as:

$$H_{\mathrm{c1}} = \frac{H_{\mathrm{c}}}{\sqrt{2}\kappa}\ln(\kappa), \tag{2.67}$$

$$H_{\mathrm{c2}} = \sqrt{2}\kappa H_{\mathrm{c}}. \tag{2.68}$$

Surface energy and the GL parameter

Whilst London theory was unable to describe the surface energy at the superconducting-normal boundaries as found in Type II superconductors, GL theory provides an effective means to accomplish this. The surface energy is defined as

$$\sigma_{\mathrm{ns}} = \int_{-\infty}^{\infty}(g(x) - g_{\mathrm{n}}(x))dx, \tag{2.69}$$

where $g(x)$ is the Gibbs free energy which is set to the normal state energy, $g_{\mathrm{n}}(x)$, for $x < 0$, and to the superconducting energy, $g_{\mathrm{s}}(x)$, for $x > 0$. Substitution for the free energy results in the description

$$\sigma_{\mathrm{ns}} = \frac{\mu_0 H_c^2}{2}\int_{-\infty}^{\infty}\left[\left(1 - \frac{h(x)}{H(0)}\right) - \left(\frac{\psi}{\psi_0}\right)^4\right]dx. \tag{2.70}$$

Here, the first term in the integral represents the positive energy contribution from the screening currents, whilst the second term representing the condensation energy has a negative contribution. Thus the sign of the integral is determined by the net balance of the condensation energy and the energy of magnetic screening, with the breakpoint found when $\kappa = \frac{1}{\sqrt{2}}$.

In 1950, Ginzburg and Landau stated that the experimental values of κ were small, and investigating the case where $\kappa \to \infty$ and $\sigma_{\mathrm{ns}} < 0$ was simply not of interest. Later Ginzburg discussed in 1952 that instability of superconductivity in cases where $\kappa > \frac{1}{\sqrt{2}}$, where the surface energy is negative, would not destroy superconductivity when the critical field was exceeded ($H > H_\mathrm{c}$), but instead promote the separation of the material into alternating normal and superconducting layers [**36**].

Abrikosov 1952 started investigated cases where $\kappa > \frac{1}{\sqrt{2}}$ [**37**]. He found that for cases of $\kappa > \frac{1}{\sqrt{2}}$ and below a second critical field, called the upper critical field, $H_{\mathrm{c}2} = \sqrt{2}\kappa H_\mathrm{c}$, flux was still able to penetrate the superconductor in the form of magnetic vortices [**15**]. He proposed that this case comprised a distinct class of superconductors, Type II superconductors. The vortices each carry one quantum of flux, and arrange themselves into a vortex lattice. The region between $H_{\mathrm{c}1}$ and $H_{\mathrm{c}2}$, is called the mixed state, also known as the Abrikosov phase or the Shubnikov phase. The mixed state is discussed in further detail in Section 2.3.2.

2.2.5. The Bardeen, Cooper and Schrieffer theory

The initial microscopic theory of Bardeen, Cooper and Schrieffer (BCS theory), was published in early 1957 [**38**], and an enhanced 29-page version was published later that year [**39**]. Gor'kov showed in 1959, that it was possible to derive GL theory from BCS around T_c [**40**]. Of fundamental importance was the identification of Cooper pairs, which are pairs of electrons coupled together by phonons, across large atomic distances, to produce a single coherent superconducting state.

As a negatively-charged electron passes through the crystal lattice, it attracts positively charged ions from the lattice, causing it to distort. The fastest possible response of the lattice is the highest possible frequency of the lattice, the Debye characteristic frequency of acoustic vibration. As the electron passes, the deformation in the lattice then attracts a second electron, due to the local increase in positive charge. Two electrons with opposite spin and momentum form Cooper pairs. With a total spin of zero, the Cooper pair acts as a boson, and occupy the same quantum BCS ground state. Condensation of electrons to Cooper pairs can therefore be described by a single macroscopic wavefunction. Cooper showed that an attractive force of any size between two electrons would result in the instantaneous paring of these electrons, changing the material properties [**41**]. At low temperatures, it is energetically favourable to form Cooper pairs, rather than maintain a normal state.

The primary experimental clue that indicated the involvement of the lattice with superconductivity was the isotope effect, where the transition temperature of a material was dependent on the isotopic mass. Discovered 1950 by Reynolds *et al* [**42**] and Maxwell [**43**], they found that the critical temperature of Mercury differed between isotopes in accordance with

$$T_\mathrm{c} \propto (m_\mathrm{i})^{-a}, \tag{2.71}$$

where m_i is the isotopic mass, and a is a dimensionless constant, which is typically around 0.5 for most superconductors. In non-elemental superconductors, each element that constitutes the compound or alloy will have its own a, so each element will produce its own isotope effect.

Critical temperature

The evidence from the isotope effect lead to the one of the major relationships contributed by BCS: the linkage between the critical temperature of the material to the lattice properties given by

$$k_{\mathrm{B}}T_{\mathrm{c}} = \frac{1}{\beta_{\mathrm{c}}} \approx 1.13\hbar\omega_{\mathrm{D}}\exp\left(-\frac{1}{\lambda_{\mathrm{ep}}}\right), \tag{2.72}$$

where ω_{D} is the debye frequency and λ_{ep} represents an electron-phonon parameter. The substitution $\lambda_{\mathrm{ep}} = VN(E_F)$ may be made, where V is an electron-electron attractive interaction representing the strength of electron-phonon coupling potential, and $N(E_F)$ is the density of states. With an experimentally determined average coupling of $\lambda_{\mathrm{ep}} = 0.3$, and with a typical frequency range of $\omega_{\mathrm{D}} = 10^{12} - 10^{13}$ Hz corresponding to a Debye temperature range of $\Theta_{\mathrm{D}} = 100 - 500$ K, the BCS upper limit for the critical temperature would be around 25 K[‡].

This BCS limit clearly does not directly apply to HTS, as the critical temperatures are certainly well above even the most extended predictions, but BCS still remains a foundation in the theory and understanding of all superconductors.

Energy gap

BCS theory makes use of the superconducting energy gap, Δ, that separates the superconducting state from normal state, with the minimum energy required to separate a Cooper pair, given as 2Δ. At $T = 0$, the gap, Δ_0, was shown to be

$$\Delta_0 = \frac{\hbar\omega_D}{\sinh\left(\frac{1}{V_0N(0)}\right)} \approx 2\hbar\omega_D\exp\left(-\frac{1}{V_0N(0)}\right), \tag{2.73}$$

and comparing with Equation (2.72) for the critical temperature, we find that the energy gap can be expressed as

$$2\Delta_0 = \beta_{\mathrm{c}}k_{\mathrm{B}}T_{\mathrm{c}}, \tag{2.74}$$

where for weak-coupled superconductors, $\beta_{\mathrm{c}} = 2\,\pi e^{-C} \approx 3.53$, with C Euler's constant. After substitution, the simple relation for the energy gap dependence on the critical temperature is given by

$$2\Delta_0 = 3.53k_{\mathrm{B}}T_{\mathrm{c}}, \tag{2.75}$$

which implies that the gap has a linear dependency on the critical temperature T_{c}. Away from $T = 0$, the superconducting gap has a temperature dependence of

$$\Delta(T) = 1.74k_{\mathrm{B}}T_{\mathrm{c}}\left(1 - \frac{T}{T_{\mathrm{c}}}\right)^{1/2}. \tag{2.76}$$

The normalised energy gap, $\frac{\Delta(T)}{\Delta_0} = \left(1 - \frac{T}{T_{\mathrm{c}}}\right)^{1/2}$, versus the reduced temperature, $t = \frac{T}{T_{\mathrm{c}}}$, is shown in Figure 2-9.

[‡] In 1967, McMillan published a formula to predict maximum T_{c} from the Debye temperature Θ_{D}, the electron-phonon coupling λ, and a Coulomb "psuedopotential", μ^* [**55**]. The maximum T_{c} for a class of materials is easily calculated from that, the upper limit being about the same as presented here.

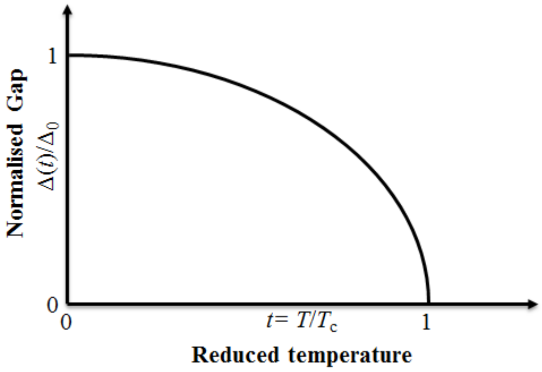

Figure 2-9 Theoretical temperature dependence of the normalised superconducting energy gap.

Coherence length

In BCS theory, the intrinsic BCS coherence length, ξ_0, describes the maximum distance over which the coherent electron-electron interactions of Cooper pairs can exist. Whilst not temperature dependent, it does, however, depend on the energy gap:

$$\xi_0 = \frac{\hbar v_{\mathrm{F}}}{\pi \Delta_0}. \tag{2.77}$$

Typically, most coherence lengths are in the range of 0.1–1 μm. For materials operating in the clean limit, $\xi_0 \ll l_{\mathrm{e}}$, the impurities hardly limit the electron mean free path, and hence should have little effect on the coherence length. In this case, the coherence length may be defined as

$$\xi(T) = 0.74\xi_0 \left(\frac{T_{\mathrm{c}}}{T_{\mathrm{c}} - T}\right)^{1/2}. \tag{2.78}$$

On the other hand, for materials operating in the dirty limit, $\xi_0 >> l_{\mathrm{e}}$, the impurities have reduced the electron mean free path length to well below the spacing of electrons in a Cooper pair, and thus can be expected to significantly affect the coherence length. The coherence length may be defined for this case as

$$\xi(T) = 0.85\sqrt{\xi_0 l_{\mathrm{e}}} \left(\frac{T_{\mathrm{c}}}{T_{\mathrm{c}} - T}\right)^{1/2}, \tag{2.79}$$

where a decrease in the electron mean free path length due to an increase of impurities results in an overall decrease in the coherence length.

Penetration depth

The penetration depth expression derived from BCS has a dependence of temperature dependence described by

$$\lambda(t) = \lambda_0 \left[\frac{\Delta(t)}{\Delta_0} \tanh\left(\frac{\beta_{\mathrm{c}}}{4t}\frac{\Delta(t)}{\Delta_0}\right)\right]^n, \tag{2.80}$$

where $t \equiv \frac{T}{T_{\mathrm{c}}}$ is the reduced temperature, and n is introduced to take into account the cleanliness of the specimen. The value of n for the dirty case is $n = -\frac{1}{2}$, whilst for the clean case it is $n = -\frac{1}{3}$. Thus in contrast with the BCS coherence length, the penetration depth increases as scattering from impurities that decreases the electron mean free path.

2.3. Characteristic properties of superconductors

Superconductors exhibit a large number of unique properties, and along with them, many theoretical problems to solve. Some of these properties and characteristics are discussed briefly: the two types of superconductors are discussed, and the mixed state that stems from Type II superconductivity is also discussed, along with the Bean critical state model for Type II superconductors.

2.3.1. Type I and Type II superconductors

As mentioned previously in Section 2.2.4, Abrikosov proposed that superconductors could be classified as either Type I or Type II, based on the response of the material to an applied magnetic field [**15**]. Most elemental superconductors are Type I superconductors, and conversely, most compounds and alloys are Type II superconductors, exhibiting the mixed state.

The perfect diamagnetism of the Meissner effect cannot be explained by perfect conductivity, as a perfect conductor operates as flux conserver. As a flux conserver, the material ensures that the rate of change of flux, $\frac{dB}{dt}$, is zero. Superconductors, on the other hand, act as flux expellers, and ensure that the flux density itself is zero. Obviously, this only holds for operation within certain bounds, defined by the critical field.

In Type I superconductors, flux is excluded up to the critical field, after which a further increase in the applied field will result in the superconductor transitioning to a normal state. In Type II superconductors the situation is slightly different as they have two critical fields, a lower and upper critical field. Up to the lower critical field, perfect diamagnetism is observed, after which the superconductor enters the mixed state, where it is energetically favourable for the superconductor to form normal regions called vortices through which flux can penetrate. These normal regions increase in density as the applied field is increased, up to the upper critical field where the superconductor is entirely normal, and there is no expulsion of flux. The different field profiles for the three states are shown in Figure 2-10.

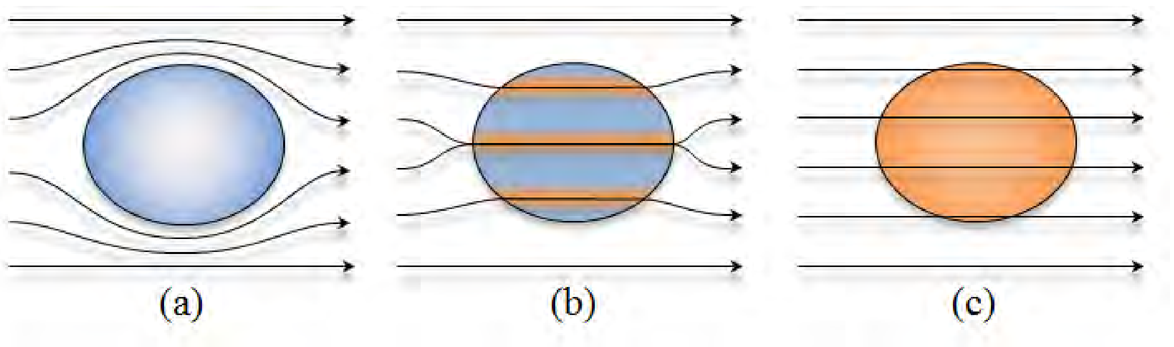

Figure 2-10 Field profiles for superconductors operating in the Meissner state (a), the Mixed state (b) and normal state (c). Type I superconductors move from (a) to (c) as $H > H_c$, whilst Type II move from (a) to (b) as $H > H_{c1}$, and from (b) to (c) as $H > H_{c2}$.

In a material, the flux B and applied field H_a are related by

$$B = \mu_0 (H_a + M), \tag{2.81}$$

where M magnetic moment per volume, known as the magnetisation. This implies that for diamagnetism, $M = -H_a$. The ideal reversible magnetisation response of Type I and Type II superconductors is shown in Figure 2-11, where the magnetisation plotted as $(-M)$ for ease of reading.

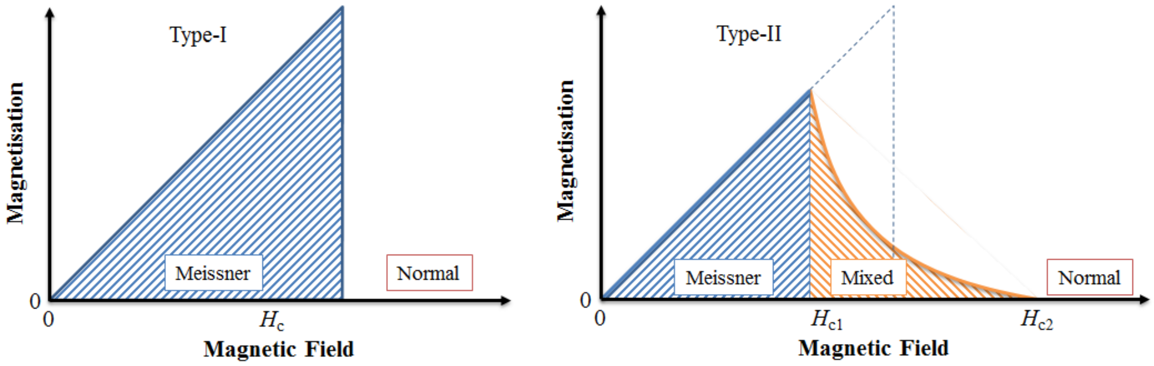

Figure 2-11 Magnetisation response of Type I and Type II superconductors, showing the Meissner state, the mixed state, and the normal state. The plots are inverted, effectively showing ($-M$) vs. T.

In practice this ideal response is not obtained due to the fact that vortex motion is inhibited by pinning centres, such as material defects and lattice dislocations. This results in hysteresis and the $M(H)$ curve becomes non-reversible.

A simple means to obtain H_{c2} is achieved by starting from within high field ($H > H_{c2}$), and then decreasing the applied field. When the applied field is reduced to H_{c2}, superconducting regions will nucleate spontaneously, and the measured magnetisation and resistivity will suddenly deviate from the normal state values, and a thus reading of upper critical field may be taken.

2.3.2. The mixed state

In the mixed state, the flux flowing through the vortices is quantised, with each vortex carrying exactly one flux quantum defined as

$$\Phi_0 = \frac{hc}{e^*} = \frac{hc}{2e}, \tag{2.82}$$

where h is Planck's constant, and c is the speed of light.

The vortex consists of a normal core surrounded by a circular supercurrent. The normal core is 2ξ wide, and the circular supercurrent surrounding the core falls off at one λ around the core. Vortex-vortex interaction is small at the onset of the mixed state, as the number of vortices is small and evenly distributed. As the field increases and the number of vortices increase, the supercurrents circulating each vortex interact with each other, causing a repulsion force. This repulsion force causes the formation of a 'vortex lattice'. Abrikosov originally determined that a regular square array arrangement of the vortices would minimise the free energy of the superconductor, and hence would be the most preferred arrangement [**15**]. Numerical calculations by Kleiner *et al* in 1964 showed that this was not true, instead showing that a triangular array resulted in a slightly lower free energy, and would thus be the preferred arrangement of vortices [**44**]. This triangular arrangement was confirmed by Essmann and Träuble in 1967 [**45**]. Figure 2-12 shows this triangular lattice arrangement.

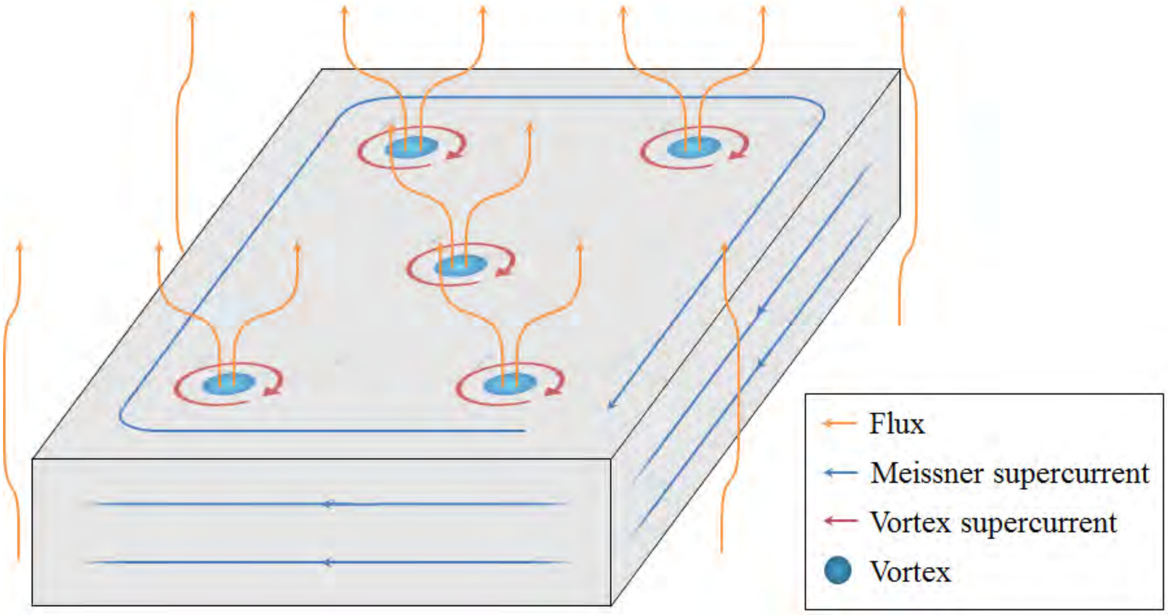

Figure 2-12 Vortex lattice of a superconductor in the mixed state. Flux penetrates the superconductor bulk through vortices, which are arranged in a triangular lattice, due to the interaction of the supercurrents that circulate the vortices.

Due to the circulating supercurrents surrounding the vortices, when a Type II superconductor is operating in the mixed state carries a transport current, there is an interaction force between the two currents. This interaction results in a Lorentz force on the vortices that acts against the pinning force, tending to push the vortices sideways. This Lorentz force is described by $\vec{F}_\mathrm{L} = \vec{J} \times \frac{\Phi_0}{c}$. If this force causes the vortices to move at a velocity v, they effectively induce an electric field described by $\vec{E} = -\vec{B} \times \frac{\vec{v}}{c}$. This electric field causes power dissipation in the superconductor, which is obviously highly undesirable.

To avoid power dissipation, it is necessary to ensure that the vortices do not move, which is accomplished by pinning the vortices, introducing a pinning force f_p that counteracts the Lorentz force. Pinning is accomplished by the spatial inhomogeneities in the material, and can be enhanced by doping and disorder. If the pinning force is equal to the maximum Lorentz force, the vortices will not move, and the critical current density can be defined as $J_\mathrm{c} = \frac{f_\mathrm{p}}{B}$ [**46**]. A current exceeding this value will result in depinning of the vortices, and power dissipation will occur. The vortices do not move in and out of the superconductor boundary one at a time, but instead as avalanches; large numbers of vortices suddenly moving at once [**47**].

The field dependence of $J_\mathrm{c}(H)$ is determined by the bulk flux pinning function F_P, known as the pinning force density, which is an approximate summation of all the localised pinning forces f_p's [**48**]:

$$F_\mathrm{P} = H_\mathrm{c2}^m f(h) \tag{2.83}$$

where $h = \frac{H}{H_\mathrm{c2}}$ represents the normalised point where the pinning force diminishes to zero. In reality, this field is not at H_c2, but instead much lower, at what is called the irreversibility field, H_irr. The irreversibility field is the maximum applied field that still permits a J_c high enough to be of practical use, as beyond this field limit there is a rapid suppression of J_c. The field is thus normalised to the irreversibility field as $h = \frac{H}{H_\mathrm{irr}}$.

The pinning force density has a maxima at a point h_max, to which the pinning force density is usually normalised, i.e.: $\frac{F_\mathrm{P}(h)}{F_\mathrm{P}(h_\mathrm{max})}$. Dew-Hughes proposed a scaling for the normalised pinning force density of

$$f_\mathrm{N}(h) \propto h^p (1-h)^q, \tag{2.84}$$

where $f_\mathrm{N}(h)$ is the normalised pinning force density, p and q are dimensionless parameters describing the particular pinning mechanism. In describing the mechanisms and taking into account only normal pins (non-superconducting) by setting $q = 2$, then the index p defines the pins in terms of mode, dimensions and spacing of the pins, as detailed in Table 2-1.

Table 2-1 Pinning modes and pin spacing for different values of the p index.

p	Pinning mode	Pin spacing
0	Normal volume pinning	$d < a, b, c$
0.5	Normal GB pinning	$d < a, b$
1	Normal point pinning	$d > a, b, c$

The parameters a, b, c, from Table 2-1 are the dimensions of the pin, and d is the vortex spacing. The scaling relation also implies that the normalised pinning force is independent of temperature, which is not entirely true, as some materials favour different pinning modes at different temperatures. The pinning mode is easily determined by the contour of the normalised pinning force, and thus for plots obtained at different temperatures, the mode of pinning at different temperatures can be easily determined.

2.3.3. Bean Critical State Model

1962 Bean developed a model for Type II superconductors where there is significant pinning, resulting in the magnetisation being distinctly non-reversible [**49**, **50**]. Under this condition, the critical state model (CSM) introduces specimen geometry, and assumes only two states for zero resistance: either $J = 0$, or $J = J_c$.

If a magnetic field is applied to an initially unmagnetised slab of Type II superconductor, bipolar screening currents will be established to cancel the field in the central region of the superconductor. These currents have a density of J_c, and extend from the surface into bulk and suddenly drop to zero where the field penetration reaches zero. There exists a limit, H_p, that the applied field may attain just as the screening currents reach full penetration, and the entire cross sectional area of the superconductor has a current density of $+J_c$ or $-J_c$. This peak value is defined as $H_p \equiv \frac{J_c}{10c} D$, where D is the slab thickness. The field penetration in increasing field is shown in Figure 2-13.

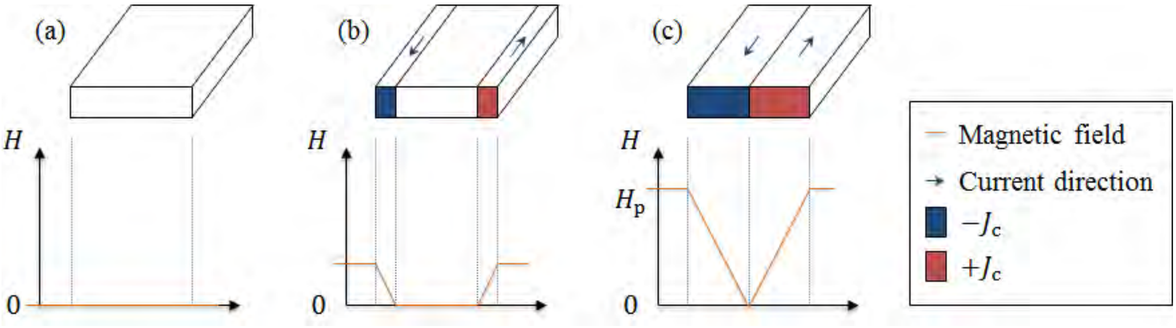

Figure 2-13 Magnetic field profile of a Type II superconducting slab in increasing applied field, according to the Bean model. The screening current penetrates deeper as the field increases, reaching full penetration at a limit H_p.

As the applied magnetic field is reduced, the superconductor surface experiences an emf that induces the formation of an additional pair of bipolar screening currents. These additional screening currents serve to cancel the field established by the inner screening currents. As the applied field reaches zero, there is still flux trapped inside the superconductor bulk. The field profile of for decreasing applied field is shown in Figure 2-14.

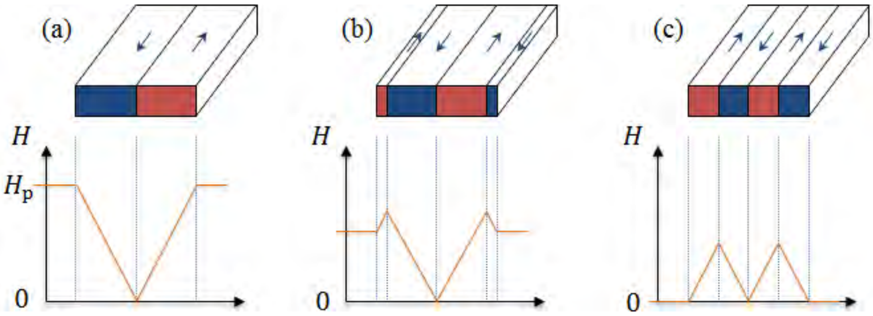

Figure 2-14 The Bean model magnetic field profile of a Type II superconducting slab for the case of decreasing applied field. Vortex pinning results in the formation of magnetisation hysteresis, causing flux to be trapped within the superconductor after the applied field has been removed.

The residual flux, B_r, trapped in the bulk can be shown to be $B_r = \frac{H_p}{4}$, and recalling that $B = \mu_0(H_a + M)$, in the absence of an applied field the magnetisation can be shown to be

$$M \propto \frac{J_c D}{10}, \tag{2.85}$$

implying that the magnetisation is dependent on the critical current density and specimen geometry. Rearrangement of Equation (2.85) leads to a useful expression of the critical current

$$J_c = \frac{\Delta M}{d}, \tag{2.86}$$

where d is a particular length parameter determined by specimen size and geometry. In this scenario, ΔM refers to the magnetisation hysteresis width, the difference in the measured magnetisation in an increasing field (M^+) and decreasing field (M^-), i.e. $\Delta M = M^- - M^+$. Thus, from contactless magnetisation measurements, the critical current density can be easily determined.

In the original CSM proposed by Bean there is an assumption that J_c is independent of B, which is obviously a simplification, and others such as Kim *et al,* have developed the CSM for the case where $J_c = f(H)$ [**51**].

2.4.Summary

A brief history with the significant milestones was discussed; the discovery of superconductivity, the Meissner effect, the two types of superconductors and their properties, and the discovery of some important superconductors. The empirical London and GL theories were discussed, and the BCS microscopic theory of superconductivity was investigated. Finally some characteristic properties of superconductors were described. These theories and properties provide vital background information for the understanding of superconductivity.

Chapter 3 Magnesium diboride and its applications

3.1. Discovery and physical structure

The superconductivity property in MgB_2 was discovered in 2001 by Nagamatsu *et al*, showing a highest-yet T_c for non-cuprate compounds, of 39 K [**26**].They showed in their preliminary tests that the superconducting fraction was 49%, with such a high fraction indicating that the superconductivity was bulk in nature.

MgB_2 is a simple intermetallic compound known since the 1950's with the AlB_2-type structure – a structure identified by Matthias as a possible candidate for high T_c superconductivity [**52**]. The two constituent elements are abundant and inexpensive, both featuring low mass density. The boron atoms are arranged in graphite-like honeycomb planes, interleaved by hexagonal planes of magnesium. Each magnesium atom is centered about the boron hexagon, giving lattice parameters of $a = 3.08$ Å and $c = 3.51$ Å [**53**], a structure that is stable to pressure over 40 GPa and below 2 K. The structure is shown in Figure 3-1.

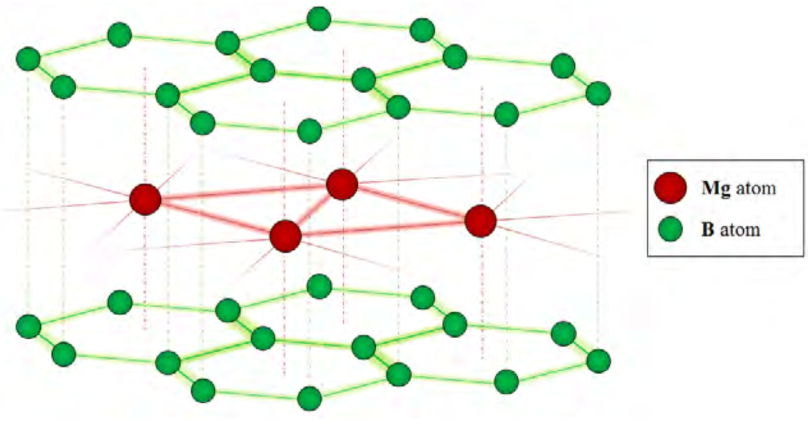

Figure 3-1 Crystal structure of MgB_2. Hexagonal planes of boron atoms are andwiched between layers of Mg atoms, with the Mg atoms centered about the hexagon center.

The discovery came about as a search for light quaternary and ternary compounds with high density of states, typically realised by the use of transition metals with partially filled d-shells. Before finding superconductivity in MgB_2, Akimitsu had been exploring the ternary systems with titanium, boron and magnesium, which the titanium providing 3 d-electrons to increase the density of states.

MgB_2 was confirmed as a phonon-mediated BCS superconductor [**54**], with superconductivity provided by Cooper pairs formed via the interaction between phonons and electrons; phonons were found to be able to produce an attraction between like-charged electrons. With a T_c of 39 K, it exceeds, or is at, the limit set by the BCS framework, which was expected to be ~30 K [**55**].

The isotope effect is a clear indicator for phonon-mediated superconductivity, as BCS theory predicts a decrease in T_c based on an effective increase in isotopic mass, due to the lowering of the Debye frequency of acoustic lattice vibrations, ω_D [**56**]. In MgB_2, the isotope effect was observed as T_c increased by about 1 K due to change from ^{11}B to ^{10}B, corresponding to a boron isotope exponent of $\alpha_B = 0.3$ [**57**]. In Mg isotope experiments, however, the change was less than 0.1 K ($\alpha_{Mg} = 0.02$), highlighting the highly selective phonon coupling related to the vibration of the boron atoms rather than magnesium atoms. The BCS mechanism in MgB_2 has also been confirmed by other experiments, such as scanning tunnelling microscopy [**58**] and high-resolution photoemission spectroscopy [**59**].

3.2. Electronic structure & two-band superconductivity

The band structure of MgB_2 is similar to graphite, featuring two interacting bands; the 3D π bands from the boron p_z orbitals, and the 2D σ bands from the p_{xy} orbitals. Charge density experiments have identified that the bonds between the boron layers are metallic, with the Mg atoms ionised, donating their electrons to the conduction band allowing for conduction in the *c*-axis perpendicular to the boron basal plane [**60**]. Charge density experiments also identified strong covalent bonding between boron atoms; this bond strength results in the coupling of the boron states to the σ band.

In conventional superconductors, there is a single temperature-dependant superconducting energy gap, $\Delta(T)$, which is non-zero below T_c but closing to zero at T_c as superconductivity ceases. This gap determines the minimum energy, $2\Delta(T)$, required to separate Cooper pairs into two separate quasiparticles [**61**]. Initial experiments revealed what appeared to be a single gap of 2-5.9 meV, but was not conclusive, as some experiments such as specific heat measurements showed evidence for two band superconductivity [**62**, **63**]. A variety of further experiments on optical properties [**64**], magnetic properties [**65**], and scanning tunnelling experiments [**66**] indicated a superconductor with two superconducting energy gaps, confirming the long-standing theory predicted by Suhl *et al* [**67**]. Based on the electronic structure and calculations on the electron-phonon coupling, a two band model was proposed [**27**]. Although evidence for two band superconductivity had been identified before, MgB_2 was the first superconductor with such pronounced effects. Scanning tunnelling microscopy clearly showed two energy gaps, with each gap obeying the temperature dependence predicted by BCS theory, and closing at the same T_c [**68**]. These two gaps arise from the different strengths in electron-phonon coupling in the two bands. Individual treatment of the bands with $2\Delta(0) = 3.53kT_c$ from BCS theory showed that the gaps should have two different T_c's of 15 K and 45 K. If the two gaps were independent, there would be two superconducting condensates within the same crystal structure with different T_c's and superconducting properties. Instead, finite coupling due to small-scale interband scattering between the two bands results in a single value of T_c, with the two bands able to retain some of their distinct characteristics.

At the Fermi surface, the weak k_z dispersion in the σ bands produces two bonding (hole-like) columns, whilst the π bands produce two 3-dimensional tubular networks, one bonding (hole-like) and one anti-bonding (electron-like) type [**60**].

There are four conduction bands, with four phonon modes: B_{1g}, E_{2g}, A_{2u}, E_{1u} at the Brillouin zone centre, Γ [**69**]. There is one high energy symmetrical optical phonon gap, E_{2g}, is associated with the in-plane movement of the boron atoms. It is anharmonic, and the phonon energy has a term that is dependent on a fourth-order boron displacement [**54**]. E_{2g} has large impact because it affects the conduction electrons and sets the energy scale for superconductivity, effectively replacing $\bar{h}\omega_D$ term in Equation (2.72), the BCS critical temperature formula, to give the correct T_c despite the relatively low $N(E_F)$ [**70**].

Due to the similarities of the two σ bands and the two π bands, the 4 bands are reduced to 2 bands. The electron-phonon coupling constant is thus reduced from a 4 x 4 matrix that considers phonon-mediated scattering from *any* of the 4 bands to *any* other of the 4 bands, to a 2 x 2 matrix considering scattering within and between the two *types* of bands. Measurements of the matrix elements shows that the electron-phonon coupling strength is very strong in the σ bands, significantly larger than the π bands, whilst interband coupling is further reduced, as shown in Table 3-1.

Table 3-1 A comparison of electron-phonon coupling matrix elements obtained experimentally. Coupling in the σ bands is strongest, resulting in the greatest contribution to T_c.

Coupling matrix element	Floris *et al* [71]	Choi *et al* [72]§	Liu *et al* [27]§	Golubov *et al* [68]	Mazin *et al* [73]
$\lambda_{\sigma\sigma}$	0.83	0.78	0.96	1.02	0.79
$\lambda_{\pi\pi}$	0.28	0.21	0.29	0.45	0.37
$\lambda_{\sigma\pi}$	0.22	0.15	0.23	0.21	0.30
$\lambda_{\pi\sigma}$	0.16	0.11	0.17	0.16	0.09
λ	0.71	0.61	0.77	0.87	-

As can be seen from Table 3-1, the anisotropy in multiband MgB_2 differs in superconducting state compared to normal state. Tsuda *et al* determined a relationship between the global coupling constant to the individual matrix elements [**74**]:

$$\lambda = \frac{(\lambda_{\sigma\sigma}+\lambda_{\pi\pi})}{2} + \sqrt{\left[\frac{(\lambda_{\sigma\sigma}-\lambda_{\pi\pi})}{2}\right]^2 + \lambda_{\sigma\pi}\lambda_{\pi\sigma}} \tag{3.1}$$

It is interesting to note that in the absence of interband coupling ($\lambda_{\sigma\pi}, \lambda_{\pi\sigma} = 0$), the global coupling parameter is identical to the coupling in the σ bands, irrespective of any coupling in the π bands:

$$\lambda = \frac{(\lambda_{\sigma\sigma}+\lambda_{\pi\pi})}{2} + \sqrt{\left[\frac{(\lambda_{\sigma\sigma}-\lambda_{\pi\pi})}{2}\right]^2 + (0)} = \frac{(\lambda_{\sigma\sigma}+\lambda_{\pi\pi})}{2} + \frac{(\lambda_{\sigma\sigma}-\lambda_{\pi\pi})}{2} = \lambda_{\sigma\sigma} \tag{3.2}$$

This supports the idea that it is the small, but non negligible interband coupling that results in the π band playing a role in determining the superconducting properties.

The coupling matrix also determines the critical temperature, given by the eigenvalue of the matrix (a value similar to the largest element in the λ matrix). The sum of all the conducting paths determines the conductivity of the specimen, as these channels are effectively parallel conductors.

The two-band nature of MgB_2 contributes significantly to the scattering mechanisms and to the anisotropies in the current and magnetic properties. Understandably, due to the fact that this is the first superconductor with such pronounced two-band effects, much research on this feature has been conducted, but beyond the coupling matrix and the effects of the interband and intraband impurity scattering on current and magnetic properties, much of the theory falls out of the scope of this research.

---

§ Obtained via integration by Mazin and Antropov [**60**]

3.3.Properties

3.3.1. Normal state and crystalline properties

As the Mg atoms in the lattice are fully ionised, MgB_2 features metallic properties in the normal state. The normal state conduction is thus in the *c*-axis direction, orthogonal to the boron planes.

Whereas electrical conductivity is determined solely by charge transported by electrons, the thermal conductivity is determined by the summation of the contributions from heat carried by both electrons and phonons [**75**]. In MgB_2, the temperature and magnetic field dependence of the thermal conductivity can be expressed as the summation of *three* contributions, as the electronic contribution can be split due to the discrete characteristics of each of the two bands [**76**]. As a benchmark, the thermal conductivity in the *ab*-plane at 273 K is 70 $W.m^{-1}.K^{-1}$ and at 100 K is ~100 $W.m^{-1}.K^{-1}$, which is slightly higher than the thermal conductivity of brass at low and moderate temperatures [**77**].

Thermal expansion of MgB_2 from room temperature shows significant anisotropic behaviour, with expansion in the *c*-axis being twice as much as the expansion in the *a*-axis [**78**]. This anisotropy arises from the fact that the bonds between the Mg atoms and the B planes are weaker than the in-plane bonds.

Grain size and distribution play a significant role in determining the superconducting properties, with dense smaller grains giving better superconducting properties [**79**]. Bimodality in the precursor boron results in easily identifiable bimodality in MgB_2 product [**80**], and unsurprisingly, this bimodality also appears from precursors obtained from mixtures [**81**]. Superconductivity is maintained in porous specimens down to a critical density $\gamma_c \cong 0.16$ [**82**], which corresponds to the 3D percolation theory limit [**83**].

3.3.2. Resistivity

Unlike HTS, MgB_2 has a low bulk normal resistivity of 1 μΩ.cm [**84**]. Canfield *et* al have demonstrated dense wires with a normal state resistivity of 0.38 μΩ.cm [**85**]. Substantial magnetoresistivity is noted in the normal state, where the resistivity is a function of the applied magnetic field, and is a due to the low resistivity [**86**] and within the multiple-band structure, due to the fact that 3 bands are hole-like, and only one electron-like [**86**, **87**]. Partially as a result of the low values of resistivity, there is a pronounced magneto resistivity in MgB2, with the normal state resistivity dependent on the applied magnetic field [**88**].

The resistivity of metals can be expressed as a combination of a temperature independent factor and a temperature dependent factor. The temperature independent contribution to the resistivity, ρ_0, results from electron scattering at defect points in the structure, whilst the temperature dependent contribution, $\rho_{ph}(T)$, is determined by scattering due to phonons. The resistivity can therefore be expressed as $\rho(T) = \rho_0 + \rho_{ph}(T)$.

A useful parameter that describes the temperature behaviour of the resistivity is the residual resistivity ratio (RRR), defined as the ratio between room temperature resistivity and the residual resistivity right before transition to superconducting state, i.e. R(300 K)/R(40 K). The RRR can therefore be utilised when comparing specimens with different resistivities, as it is merely a ratio and discards the absolute values of specimen resistivity. For further investigation, the change in resistivity can be calculated and approximated as $\Delta\rho = \rho(300\text{ K}) - \rho(40\text{ K}) \approx \rho_{ph}(300\text{ K})$, giving access to the isolated phonon contribution.

In MgB_2, the normal state resistivity obeys a power law in accordance with the Bloch-Grüneisen behaviour, where resistivity is of the form $\rho(T) \propto T^{\alpha}$, but the coefficient α varies from 2-5 among specimens due to differences in cleanliness [**89**].

Measurements on numerous specimens have shown a large variation in the reported specimen resistivities, yet similar T_c's [**90**]. The fact that T_c remains unchanged is largely attributed to differences in specimen connectivity arising from the vastly different methods of manufacture [**90**], but also as a consequence of the weak interband scattering in MgB_2 [**73**]. The variation in residual resistivities is due primarily to scattering *within* the π and σ bands, not from scatting *between* them. In MgB_2, the interband scattering rate is very small, and the intraband impurity scattering in the σ is much smaller than the intraband impurity scattering in the π band. Despite that impurities significantly affect intraband impurity scattering in the π bands and hence the normal state conductivity, they do not have as large an effect on the interband scattering rates and T_c.

The resistivity in MgB_2 is anisotropic, with the out-of-plane resistivity being higher than the in-plane resistivity. In polycrystalline specimens therefore, the randomly oriented grains give a resistivity that is a combination of the two resistivities [**91**].

3.3.3. Magnetic properties

The two magnetic properties of MgB_2 that are of particular interest are the upper critical field H_{c2}, and the magnetic irreversibility field H_{irr}. The upper critical field determines the maximum possible field that may be applied to the superconductor whilst still maintaining superconducting state. The magnetic irreversibility field determines the maximum operating field for non-zero current transport that will still maintain superconducting state.

The irreversibility line, $H_{irr}(T)$, defines the reversible and irreversible regions of the field-temperature phase diagram of the superconductor. Non-zero critical currents are confined to below this line, making it a vital parameter for applications.

Experiments have revealed that high purity MgB_2 can operate deep in the clean limit, as the clean case requirement of $l \gg \xi$ is easily satisified for an electron mean free path length of $l \approx 60$ nm and a coherence length of $\xi \approx 5$ nm [**85**].

MgB_2 wires initially showed critical fields as low 3 T [**92**], but doping and other methods can easily increase this to over 33 T [**93**]. It was shown in 2005 by Braccini *et al* that an H_{c2} of over 70 T could be obtained for dirty thin films, which indicated possible upper limits to the value of H_{c2}, which at the time were still somewhat low for bulks [**94**]. If the properties of bulks could reproduce the magnetics shown in films, MgB_2 would truly be poised for serious consideration in a number of applications.

In single-gap superconductors in the dirty limit, there exists an upper critical field of $H_{c2}(0) = 0.69T_c(dH_{c2}/dT)_{T_c}$, with $(dH_{c2}/dT)_{T_c} \propto \rho_n$. This implies that H_{c2} is affected by the specimen resistivity, which is easily altered by the addition of impurities and defects. In two-gap superconductors, however, the presence of two bands results in the ability for H_{c2} to exceed $0.69T_c(dH_{c2}/dT)_{T_c}$ [**95**].

There is a pronounced anisotropy between H_{c2} values in the *c*-axis and in the basal plane. H_{c2} values for fields oriented in the *c*-axis direction are much smaller than for fields oriented in the *ab*-plane. The GL anisotropy parameter for the upper critical field is $\gamma_H \equiv H_{c2}^{\parallel ab}/H_{c2}^{\parallel c}$, which is effectively an anisotropy of the coherence length, γ_ξ. Similarly, there exists an anisotropy parameter γ_λ, for the penetration depth which is considered to be the same for certain cases of anisotropic GL theory, but this does not hold true for MgB_2 due to the two-band effects [**96**]. A graph of the upper critical fields of MgB_2 thin films along with LTS bulks is shown below in Figure 3-2, showing clear possibilities for replacement of Nb_3Sn and NbTi if these properties can be replicated in bulk MgB_2.

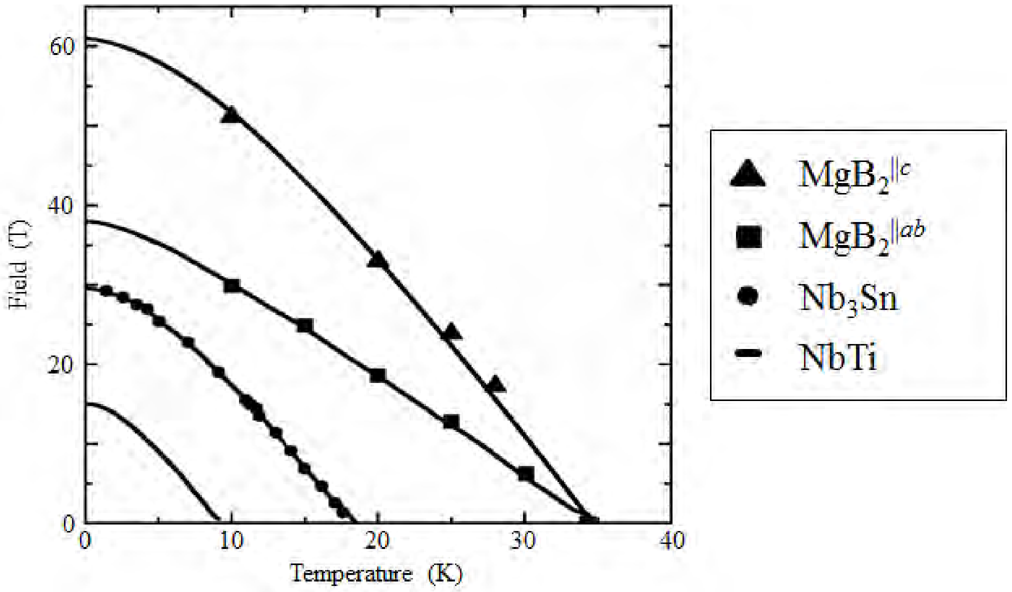

Figure 3-2 Upper critical field data of MgB_2 thin films and LTS bulks. MgB_2 thin films presently have greater critical fields and a higher critical temperature than conventional LTS, but these properties need to be transferred to bulk forms before it can replace LTS. From [97].

At T_c, the upper critical field anisotropy tends to zero, but at low temperatures the anisotropy can reach a value as high as 6 or 7 [**98**], which is in contrast with GL theory where it is not strongly temperature dependent [**99**]. The temperature dependence is due to the two-band effects, where the anisotropic σ band typically dominates in the clean case, except at higher temperatures where there is an escalation of the isotropic π gap contribution. For the dirty case, the π band contribution is just favoured at lower temperatures, accompanied by the reduction anisotropy within that temperature range accordingly. It is not only the anisotropy that has unusual temperature dependence, as the $H_{c2}||$ curve has a positive curvature around T_c, a feature which deviates from the well-established parabolic temperature dependence of Equation (2.11). Similarly to the anisotropy, the curvature near T_c is due to the influence of the π bands, explained by two band conductivity that introduces individual scattering times for each band: D_π and D_σ [**95**]. The upper critical field near T_c and at zero temperature can be expressed as having the dependence [**95**]:

$$H_{\mathrm{c2nearTc}} \propto \frac{1}{\lambda_1 D_\sigma + \lambda_2 D_\pi} \tag{3.3}$$

$$H_{\mathrm{c20}} \propto \frac{1}{\sqrt{D_\sigma D_\pi}} \tag{3.4}$$

With λ_1 and λ_2 representing coupling elements. Here H_{c2nearTc} depends on the weighted arithmetic mean, whilst at zero temperature it depends on the geometric mean. For the dirty vs. clean cases, the dependencies change as listed in Table 3-2, and clearly show H_{c2nearTc} is dependent on the larger of the diffusivities, with the converse true for H_{c20}.

Table 3-2 Critical field dependencies near T_c and zero temperature for the dirty and clean cases.

Case	H_{c2nearTc}	H_{c20}
Dirty $D_\sigma \gg D_\pi$	$H_{\mathrm{c2nearTc}} \propto \frac{1}{\lambda_1 D_\sigma}$	$H_{\mathrm{c20}} \propto \frac{1}{D_\pi}$
Clean $D_\pi \gg D_\sigma$	$H_{\mathrm{c2nearTc}} \propto \frac{1}{\lambda_2 D_\pi}$	$H_{\mathrm{c20}} \propto \frac{1}{D_\sigma}$

Within BCS theory, the paramagnetic limit is an underestimation of the true value by a factor $(1+\lambda)$, hence with the high values of coupling found in MgB_2, the paramagnetic limit of 60-70 T [**100**] could actually be as high as 130 T [**101**]. To obtain these values, it is necessary to provide optimal homogenous doping.

3.3.4. Critical currents

In MgB_2, the first $J_c(H, T)$ experiments revealed that J_c decreased rapidly with applied field and temperature, leaving satisfactory J_c values confined to low field and low temperature regions. Due to the large coherence length, the grain boundaries in MgB_2 are transparent and thus specimens do not exhibit weak-link effects [**102**]. In an HTS mind-set, the rapid decrease in J_c with applied field would suggest a GB problem, but since the grain boundaries are transparent, it instead points to a lack of vortex pinning.

The critical currents in MgB_2 depend on a number of factors, namely the connectivity (via the superconductor density and effective cross-sectional area) and the flux pinning. Recalling Equation (2.61 in Section 2.2.4, the maximum permissible current is set by the depairing current density, which can be evaluated for MgB_2 as:

$$J_\mathrm{d} = \frac{\phi_0}{3\sqrt{3}\pi\lambda^2\xi\mu_0} \sim 8.7 \times 10^8 \text{ A.cm}^{-2} \tag{3.5}$$

The highest self-field J_c's have been found in high purity thin films produced by hybrid physical vapour deposition (HPCVD), with Zeng *et al* producing specimens capable of attaining a J_c of $3.4 \times 10^7 \text{ A.cm}^{-2}$ at 4.2 K, corresponding to 4% of the depairing current [**103**], and with Zhuang *et al* producing films capable of a current density of $1.6 \times 10^8 \text{ A.cm}^{-2}$ at 2 K, corresponding to 18% of the depairing current [**104**].

Multi-filamentary wires formed by the powder-in-tube (PIT) process offer high practicality due to stability and form, and near endless construction configurations available to optimise the wire for each application. Hyper Tech Research, Inc. has produced wires that can attain 4 K current densities of 10^5 A.cm^{-2} at 4.5-5 T, and 10^4 A.cm^{-2} at 8 T. Carbon doped multi-filamentary wires boast the highest current density of 10^4 A.cm^{-2} in an applied field of 13 T [**105**].

As discussed in Section 2.3.2, there are a number of different flux pinning types that aid J_c, namely grain boundary pinning, volume pinning and point pinning. In polycrystalline MgB_2, it is grain boundary pinning that is the most prominent mode of pinning [**106**].

3.3.5. Connectivity and porosity

Porosity hinders current flow and limits J_c, and aids the introduction of current-inhibiting surface-phases that cover the grain boundaries. Although the grain boundaries are transparent in MgB_2, a surface phase covering the grains will decrease J_c.

PIT wires suffer porosity issues, as equal-sized *ex situ*[**] particles can only be packed to 65% volume density, and therefore PIT MgB_2 density can be at most 65% for uniform particle size. For the case of *in situ* [††]it is even less, because of the volume shrinkage during the reaction, which accounts for an additional 25% loss in density. Thus for equally-sized Mg and B particles packed to 65% volume density, the final density will be just 49% after reaction. The assumption of equally-sized particles is perhaps an over simplification, and for different sizes of Mg and B particles, it is found that the density may reach up to 62% [**107**]. This is far from ideal, as maximal critical current densities will only be achieved with full densification.

[**] *Ex situ* here implies the use of MgB_2 powder as the starting material, such as those commercially-available.

[††] *In situ* refers to the use of separate Mg and B powders, with the MgB_2 phase formation taking place only during heat treatment of the packed tube.

3.4. Disorder and doping

3.4.1. Mechanics

Disorder in MgB_2 plays a major role, and can be introduced intentionally via doping and irradiation, or unintentionally by contamination of the specimen from the preparations conditions and processing methods [**89**]. For example, the boron powder purity to be discussed in Section 3.5, can introduce disorder from impurities and oxygen contamination, whilst inadequate heat treatment may result in growth of secondary phases, which increase disorder. Incorrect stoichiometric ratios and ball milling for *in situ* manufacture of MgB_2 from powders also increase disorder. The disorder puts strain on the crystal lattice, the extent of which can be well measured from XRD peaks. An increase in disorder is accompanied by an increase in resistivity and generally a decrease in T_c.

Doping of MgB_2 provides a means to perform intentional atomic substitutions which alter the impurity scattering and hence the two bands and two gaps, resulting in a change in superconducting properties. Many different dopants have been tested, but successful dopants are limited, with only a limited number being successfully substituted [**108**]. The most frequently substituted elements are Al, C, Li, and Mn.

Disorder decreases coupling elements, resulting in decrease in T_c. A collective of experimental evidence of this is shown in the review of Buzea and Yamashita [**109**]. As mentioned in Section 3.2, T_c is largely determined by the σ coupling constant, and hence the reduction of holes in the σ band will lead to lower coupling constant, and hence lower T_c [**110**].

As the π bands are linked to the Mg atoms, Mg lattice distortion from atomic substitution affects the π band scattering. As the boron atoms are both in the σ band and also at the centres of the π bands, atomic substitution of B results in increased scattering in both the σ and π bands.

The upper critical field can be radically improved by impurity scattering [**5**]. Doping affects flux pinning, via enhancement of the upper critical field and irreversibility field, by introduction of localised lattice distortions, or by introduction of pinning centres [**107**]. The introduction of pinning centres by doping with TiO_2 has shown to provide an effective increase in H_c for doping concentrations up to 3% [**111**]. With such small doping concentrations required, it is essential that the dopants are distributed homogenously to ensure that the final product properties are also homogeneous. In addition, as various dopants have their own anisotropies, doping may reinforce or detract from the global anisotropy.

3.4.2. Dopants

Aluminium

Substitution of Mg by Al dopes electrons, which reduces the number of holes, and therefore has a suppressive effect on T_c. Since the Mg atoms are not located in the basal plane and hence not in the σ bands, substitution of Mg by Al mainly affects the scattering within the 3D π bands [**112**]. Without any substantial effect on the σ bands, there is no surprise that that Al doping hardly improves H_{c2} [**112**]. The interband impurity scattering remains small even at high doping levels, ensuring that the two superconducting gaps to do meet [**113**].

Carbon

Substitution of B by C dopes electrons, reducing the number of holes, and hence like Al doping, it lowers T_c. The T_c suppression versus doping fraction rate is about twice as much as that of Al [**110**]. Carbon doping enhances impurity scattering in both the π and σ bands, giving rise to different effects.

The enhanced impurity scattering in the σ band results in higher resistivity, whilst the enhanced impurity scattering in the π band is effective at increasing H_{c2} [**114**]. The enhanced impurity scattering in the π bands has been found to be an intrinsic property of carbon substitution [**115**]. Although both the resistivity and H_{c2} increase, they are not directly linked; each is a distinct function of the impurity scattering in each band [**100**].

The carbon doping also enhances the irreversibility field, indicative of stronger flux pinning [**116**]. Again, the increase in H_{c2} and simultaneous increase in H_{irr} are not necessarily directly linked, as H_{irr} is significantly influenced by the different pinning mechanisms, such as GB pinning [**106**]. The flux pinning does, however, aid the enhancement of J_c [**116**].

Among many others, carbon has been sourced from SiC, carbohydrates, acids, and via chemical vapour deposition of hydrocarbon gases. Doping with silicon carbide (SiC) has been rather successful at enhancing properties, aided by the fact that Mg decomposes SiC before reaching the MgB_2 reaction temperature. It has shown to enhance the H_{c2}, H_{irr} and J_c [**117**] [**118**] [**119**]. In these specimens, plots of the normalised pinning force show that different regimes are favoured at different temperatures, with point-type pinning dominating in the 20-30 K temperature range [**120**]. The use of SiC nano-powder is also highly effective, with the carbon substitution enhancing H_{c2}, whilst the defects, small grain size and nano-scale inclusions improve J_c [**121**].

Sucrose ($C_{12}H_{22}O_{11}$) as a carbon source has been investigated, showing a ~2.5% decrease in T_c, for an enhancement of H_{c2}, by ~52% [**122**]. Tartaric acid ($C_4H_6O_6$) doping resulted in J_c values that were significantly improved in the doped specimens, reaching 10^4 A.cm^{-2} at 5 K and 8 T, a factor of 6 higher than that of un-doped MgB_2, for a ~6% decrease in T_c [**123**]. Vajpayee *et al* tested adipic acid ($C_6H_{10}O_4$) as a carbon source, achieving similar results, concluding that the impacts of the various organic dopants are much the same [**124**]. Similar improvements were found by the doping of malic acid (), where H_{irr} and J_c were found to increase significantly for only a modest decrease in T_c [**125**].

Doping with acetone $(CH_3)_2CO$ on MgB_2 tapes showed and initial increase in J_c, but higher concentrations had little effect on the lattice parameters, and instead there was a lowering of J_c due to MgO phase formation [**126**].

Manganese

The substitution of Mg by Mn results in doping of neither electrons nor holes, as Mg and Mn are isovalent. Despite the number of holes being unchanged, there is a rapid suppression of T_c with Mn concentration, with superconductivity destroyed at just 2% [**127**]. This suppression is associated with very strong magnetic pair breaking [**127**].

Lithium

Theoretically, increasing the σ band coupling constant via hole doping should produce an increase in T_c. This has been tested experimentally by the substitution of Mg with Li, but actually showed a slight *decrease* in T_c [**128**]. To determine the cause of the decrease, it became necessary to de-convolute the contributions to T_c from lattice effects and from charge doping. Erwin and Mazin suggested co-doping of MgB_2 by Na and Al, an isoelectronic substitution that would indicate purely lattice effects [**129**]. Monni *et al* performed this with Li and Al, as Li was more practical to deal with than Na [**130**]. The results indicated that all of the observed effects were almost entirely due to the Al doping, as the Li hole doping occurred almost entirely in the π bands, which do not contribute to T_c [**131**].

3.4.3. Doping techniques

There are many means available to perform doping on MgB_2, with the most prominent being the addition of powdered dopants for *in situ* reactions, and chemical vapour deposition for both *in situ* and ex situ reactions. The choice of doping method is typically determined by the dopant used, as the form and packaging of certain dopants may exclude certain methods.

In situ doping of MgB_2 is achieved by means of dopants being added directly in powder form to the precursor powder mix, or alternatively the precursor powders may be exposed to a dopant in liquid form. Aluminium substitutions are typically performed by the addition of fine aluminium particles to the Mg+B powder mix, as are carbon substitutions by the addition of, for example, SiC.

Chemical vapour deposition

Chemical vapour deposition (CVD) can be used to perform doping. CVD has the benefit that provides *intrinsically* homogenous distribution of dopant [**10**]. CVD is performed at elevated temperatures with a process gas that is either charged prior to heat treatment, or flowed through the furnace during heat treatment. At high temperatures, the dopant either decomposes or reacts with the precursor powder to give the desired doping. Doping level is a function of time and mass of reagents. To perform high doping concentrations using CVD, it may be necessary to perform the CVD process multiple times, or otherwise to replace the process gas regularly. In addition, CVD may be used on either *in situ* or *ex situ* reactions, for different purposes. CVD for *in situ* reactions may be used to achieve substitutions and the various parameter enhancements, whilst CVD for *ex situ* reactions may be used to deposit inclusion and point defects to aid flux pinning.

3.4.4. Selection of doping technique and rationale

One of our long-term research goals is to develop a process that will allow for the ability to produce specimens with a predetermined critical current rating and resistivity that can be used in a modular fashion in the construction of a resistive SFCL.

The setting of the critical current density is to be accomplished by carbon doping. Doping, however, also affects T_c, so as a benchmark, all tests would be done at, say, 20 K. This allows for a significant decrease in T_c, as well as headroom for the transport current. Another long term design goal is the use of solid nitrogen as a cryogen and thermal battery to absorb heat energy during a fault. Here, operation below 33 K has the advantage of an additional solid-solid phase change at 36 K, which will absorb additional fault energy.

Doping of specimens produced for this dissertation was achieved by CVD of carbon onto the boron precursor powder before the *in situ* RLI technique was used to produce the bulk. The decision to use CVD for the carbon doping was made due to simplicity; the process effectively requires only a tubular furnace and a hydrocarbon gas for the carbon source.

3.5. Precursor powder

As with many of the other superconductors, superconducting properties are sensitive to processes and materials used, and as such it was necessary to investigate which forms and purities of boron powder can be used to produce high quality bulk MgB_2.

Boron powder can be obtained in two forms: crystalline and amorphous, both sourced from boron-containing compounds. Crystalline boron is black and extremely hard, having a hardness of 9.5 on the Mohs scale of mineral hardness, placing it 2nd only to diamond-carbon (10) in elemental hardness. Amorphous boron is a brown powder relatively unreactive to air, water, acids and alkalis. High purity crystalline boron can be obtained through vapour phase reduction of boron trichloride (BCl_3) or boron tribromide (BBr_3) with hydrogen gas. Amorphous boron can be obtained via high temperature magnesium reduction of boron trioxide and subsequent acid leaching which, unsurprisingly, means that most of the residual impurities in the powder are B_2O_3 and Mg [**132**].

Research has been done on precursor powder form and found that specimens made from crystalline boron have a J_c that is typically an order of magnitude lower than specimens manufactured from amorphous boron powder [**80**]. This has been attributed to the formation of (Mg)B-O phases that reduce the current-carrying cross sectional area of the superconductor. Zhang *et al* found that ball milling the precursor powders provided a significant increase in J_c, and in contrast, that the best properties were actually found with ball milled crystalline due to H_{c2} enhancement from increased disorder [**133**].

Investigations on precursor purity have also been performed, indicating mixed results. Xu *et al* have found that using 99.99% purity amorphous boron has yielded specimens with the higher J_c

values, compared to specimens manufactured from 92% and 96% purity precursor powders [**134**]. Similar results were found by Zhou *et al*, where a 40 times increase in J_c was noted when comparing specimens manufactured using 99% purity boron versus 90% purity precursor powder [**135**]. Ribeiro *et al* found that T_c is improved with an increase in precursor purity, and also noted that the *RRR* could be increased using high purity boron [**136**]. Chen *et al* found that, when comparing high and low purity amorphous and crystalline boron precursor powders, there was no difference in T_c between the high and low purity amorphous specimens, in contradiction with the Ribeiro findings [**80**].

The reactivity of amorphous boron was found to be much greater than that of crystalline boron, and is enhanced by smaller particle size [**137**]. The lower reactivity of crystalline boron means slower formation of MgB_2, hence requiring a longer reaction time. During extended reaction periods, there is increased formation of $(Mg)B_xO_y$ phases which decrease J_c [**80**].

The economics of precursor powder also play a large role, as a high purity amorphous boron powder is significantly more expensive than the technical grades of boron powder. In some situations the increase in J_c due to higher purity precursor powder may be outweighed by the increase in cost, as >99% purity boron may be as much as 10 times more expensive than 92% or 96% purity boron [**134**].

Research has also showed an innovative means to increase J_c values by mixing low purity and high purity boron powder [**81**]. In comparison with doping as a means to increase J_c, mixing different purity powders offered doubling in J_c compared to the better of the two single precursor specimens, without compromising the *RRR*. The specimen resistivity and *RRR* are affected by both intergranular and intragranular defect scattering [**90**]. Mixing precursor powders thus provides a means of increasing J_c and decreasing cost, with further improvements possible by the use of chemical doping and additional pinning techniques.

Different boron powder purity and forms also affects the thermal conductivity of superconducting MgB_2 bulk obtained by RLI, via the formation of the Mg_2B_{25} phase, which is detrimental to the thermal conductivity, but not necessarily the transport properties [**138**].

3.6. Degradation

It is well known that HTS have a high sensitivity to water and moisture; YBCO and TBCCO degrade in water, acids, carbon dioxide and carbon monoxide [**139**], and BISCCO is also known to degrade and lose superconductivity after immersion in water [**140**]. To be a practical superconductor, it is necessary to evaluate the chemical stability and ageing of MgB_2, to ensure that long term performance is not compromised, and that devices based on MgB_2 meet certain reliability metrics. In this light, soon after the discovery of superconductivity, research was conducted to evaluate the degradation behaviour of MgB_2.

In 2001, research conducted by Zhai *et al* investigated the material stability of MgB_2 thin films after direct exposure to de-ionised water [**141**]. It was found that the surface of the films degraded to an inhomogeneous layer, and that the superconducting transition width increased with exposure time. The T_c onset value, however, remained unchanged at ~39 K despite exposure up to 15 hours, indicating that some bulk-like properties were still retained. Surface morphology analysis by SEM shows that water exposure resulted in the removal of small crystallites, and the rounding of the faces of the remaining MgB_2 platelets. This decrease in connectivity is evident in the resistivity measurements, which show an increase of 2 orders of magnitude, from 1.08 Ω to 153.8 Ω.

Subsequent investigations by Cui *et al* found that high purity specimens prepared by hybrid physical chemical vapour deposition (HPCVD) showed a full degradation of the film to a transparent amorphous insulating layer [**142**]. In contrast to Zhai *et al* [**141**], exposure to water resulted in both T_c onset shifts as well as increases in the transition width. They concluded that the oxygen contamination of films prepared by other methods actually reduced the water degradation, by forming a protective buffer to underlying MgB_2. It was found that the films degraded faster in water that was not de-ionised, and that the degradation rate was *strongly* linked to the temperature of the water.

The emphasis of the research by Cui *et al* was the evaluation of compounds used during thin film processing; evaluating the degradation of the MgB_2 superconducting properties, to ensure that degradation did not take place during processing. They investigated the degradation due to photoresists used in film processing, as well as methanol, acetone and isopropanol solvents. It was found that of the solvents tested, methanol degrades MgB_2 fastest, indicated by the increase in film resistivity by a factor 2 for an exposure duration of less than 80 minutes. Acetone degradation showed a resistance increase of 20% for duration of about 16 hours, and isopropanol only showed an increase of 2% in resistance for a period of 2 weeks. It was also speculated that the mechanism of degradation could possibly be water related, due to the water content or water absorption in the solvent itself.

Song *et al* also evaluated the degradation of MgB_2 powder after exposure to solvents [**143**]. XRD analysis on powders exposed to water, acetone, and ethanol showed that phase changes only occurred for the powder exposed to water. The analysis of this specimen revealed no peaks, indicating that the powder had undergone complete dissolving of either B and or Mg to an amorphous powder, with an accompanying change in colour from black-grey to white-grey.

Aswal *et al* confirmed the strongly hygroscopic nature of MgB_2 in bulk polycrystalline specimens prepared by a sintering method [**144**]. Consistent with the findings of thin films, it was found that the room temperature resistivity increased with exposure time. It was also noted that after exposure to water, the temperature dependence of the specimen resistivity deviated from the intrinsic T^2 dependence. It was found that the exposure to water resulted in the gradual disconnection of MgB_2 grains, to such a point where they insulate. The increase in size and concentration of the voids and non-superconducting regions eventually results in the total destruction of superconductivity. XPS analysis identified the presence of $Mg(OH)_2$, $MgCO_3$ and B_2O_3, which were explained via the water reaction of:

$$\mathrm{MgB_2 + 2H_2O \rightarrow Mg(OH)_2 + 2B + H_2}$$

to which further exposure to air allowed for the reactions of:

$4B \quad 3O_2 \rightarrow 2B_2O_3$

$Mg(OH)_2 \quad CO_2 \quad MgCO_3 \quad H_2O$

Serquis *et al* found that specimens with different morphology stemming from different manufacturing procedures degrade in ambient environment [**145**]. It was found that specimens with poor connectivity and small grain sizes were substantially more susceptible to degradation, as the degradation took place at the grain boundaries, increasing the transition width whilst leaving the T_c onset unchanged. Specimens prepared by hot isostatic pressing (HIP) and specimens sintered in high purity argon were found to remain stable after several months exposed to ambient atmosphere. The XPS analysis showed a rapid decrease in boron content at the surface, and a concurrent increase in carbon and oxygen content, possibly from the reaction with O_2, CO_2 and H_2O in air. The main product identified in the degradation was $Mg(OH)_2$, which formed a layer at the surface, and possibly in the grain boundaries. For spherical grains of 5 μm and 0.2 μm diameters, the percentage $Mg(OH)_2$ for a 20 Å covering film over the grain would be 0.1% and 6 % respectively, easily explaining the increased degradation of specimens with small grain distributions.

Annabi *et al* further investigated ambient atmosphere degradation, investigating the particular components responsible for the degradation [**146**]. Bulk specimens prepared by a solid state method were tested after exposure to atmospheres consisting of pure CO_2, air + water vapour, and pure water vapour. It was found that the degradation in ambient humidity is slow. Degradation due to CO_2 was not exhibited, and it was concluded that the water acts as a catalyst for the degradation process in air, confirming the process reactions suggested by Aswal *et al* [**144**]. They observed that the degradation occurs at the surface and grain boundaries.

More recently, Rajput *et al* confirmed that the degradation was a function of the prior form and quality of the specimens, finding that specimens prepared via modified solid state reaction under vacuum conditions produced specimens that were stable for up to 2 months in ambient atmosphere [**147**]. There were no signs of phase decomposition, nor any degradation of the superconducting properties. The AC susceptibilities of specimens of varying grain connectivity were tested after exposure to water. It was found that water exposure causes an increase in transition width, with excessive exposure resulting in the development of two peaks in the complex susceptibility component, which is indicative of the inter- and intra-granular effects that have been noted in HTS. The peak at higher temperature corresponds to the intra-granular normal-superconducting transition of the individual grains, whilst the lower temperature peak corresponds to the inter-granular transition, where the grains are coupled together to give bulk superconductivity, as discussed in Section 4.7.

3.7. Methods of fabrication

Without the grain boundary effects noted in so strongly in HTS, much simpler processes may be used in fabrication of MgB_2 specimens. In addition, unlike HTS where oxygen-permeable sheaths such as Ag are required for optimal properties, MgB_2 can be surrounded by many more economical sheaths. The different processes can be classified as either *ex situ* or *in situ*.

Ex situ reactions involve the use of commercially available MgB_2 powder subjected to heat treatment. It is a cheap and simple route, but in order to obtain optimal J_c and T_c values, the heat treatment typically requires temperatures that exceed the decomposition temperature of 900-950 °C. Care needs to be taken to ensure that reaction of MgB_2 with the surrounding barriers and sheath does not take place, as the barriers and sheath may be more likely to undergo decomposition at these elevated temperatures.

In situ reactions involve the heat treatments of either a mixture or an arrangement of Mg and B to produce MgB_2, noting that the MgB_2 phase does not exit prior to heat treatment. These reactions offer specimens with excellent grain connectivity, but more importantly, require a much lower reaction temperature, typically around the melting point of Mg at 650 °C. As the reagents are separate prior to heat treatment, it is very easy to introduce and homogenously distribute dopants in the desired quantities to obtain the required lattice substitutions or defects.

3.7.1. Reactive liquid magnesium infiltration

The reactive liquid magnesium infiltration (RLI) technique was developed by Giunchi *et al*, and can be used to produce large superconducting bulk pieces [**148**]. The technique is *in situ*, enclosing the two precursor powders in a sealed metallic container that allows for large pressure increases to be generated during heat treatment. According to the Mg-B system phase diagram, favourable formation of MgB_2 takes place at temperatures above the melting point of magnesium, and at moderate pressures [**149**].

The precursor boron powder is loaded into the metal container, and pressed to obtain a density that is about 50% the natural density of boron (δ_{boron} = 2.37 g.cm^{-3}). According to the required stoichiometric ratio, a solid magnesium bulk is then placed in direct contact with the boron preform. The container lid is then inserted and the container is sealed by conventional welding techniques such as tungsten inert gas (TIG) welding. The container is designed to ensure maximum contact surface area with the boron preform, and the lid is designed to ensure there is no free space remaining after the container has been charged with the reagents. The preforms are frequently wrapped in tantalum foil, acting as barrier between the reaction and the stainless steel crucible walls. A typical container used to produce an MgB_2 pellet is shown in Figure 3-3 below.

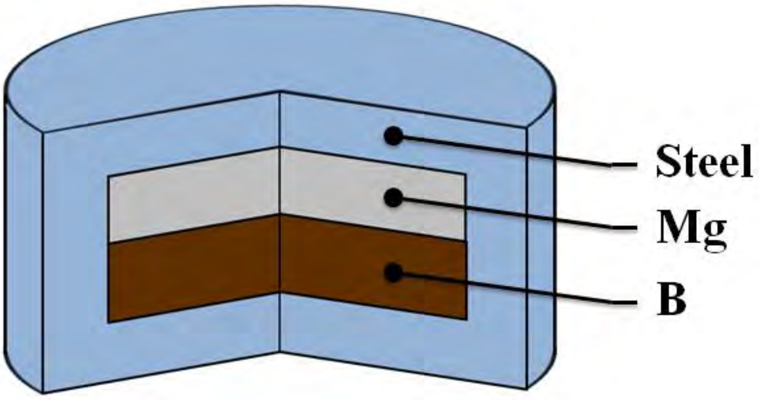

Figure 3-3 A sealed RLI container with the boron preform and magnesium pellet, prior to heat treatment.

The sealed container is then subjected to thermal treatment in the range of 750-950 °C, for durations from 0.5 hour to several hours, after which the container is cooled and machined open. After reaction, the MgB_2 product occupies almost all the boron preform space, accompanied by any excess magnesium that may not have reacted, and the rest of the space is void.

For optimal infiltration, the boron precursor powder should be of crystalline form, ground to a particle size of less than 100 µm. Infiltration of amorphous boron powder preforms is more difficult, but successful infiltrations with these preforms produces specimens with significantly improved superconducting properties [**148**].

3.7.2. Sintering

MgB_2 specimens may also be manufactured an *ex situ* manner by the sintering of pressed MgB_2 powder at high temperatures. At the elevated temperatures, however, the loss of Mg to vapour results in degradation of connectivity, and so successful sintering typically depends on ensuring that sufficient excess Mg is added to the powder mix. Sintered specimens typically have lower density and poorer mechanical properties.

There are techniques to enhance the product of sintering, namely in schemes such as field assisted sintering technique (FAST) and spark plasma system (SPS). FAST uses resistance heating in conjunction with a pulsed current that is periodically applied to the specimen under uniaxial pressure, to enhance the density and reduce process time [**150**]. SPS uses the spark plasma generated by a pulsed DC current between two electrodes to heat the specimen, and allows for rapid heating and cooling of the specimen [**151**]. Zhou *et al* found that the sintering atmosphere has a significant effect, revealing that an atmosphere of high purity Ar with 5% H_2 improved J_c, H_{c2} and H_{irr} compared to a pure Ar atmosphere [**152**].

3.7.3. High pressure

High pressure (HP) synthesis is a method for manufacturing bulk MgB_2 superconductors. In this approach, the precursor boron and magnesium powders are mixed, and subjected to thermal treatment under high pressures of the order of 1 GPa. HP synthesis was first investigated on HTS, and resulted in increased critical current density, physical density and improved mechanical properties [**153**]. Hot pressing is used because thermal instability at high temperatures results in the reaction favouring the phase of MgB_4, for both *in situ* and *ex situ* processes [**154**]. HP synthesis has also been applied to the manufacturing of MgB_2, yielding similar improvements, as well as improvements in the irreversibility field [**155**].

HP synthesis has been the subject of much research, with investigations being performed on the effect of doping and the effect of additions on the superconducting properties. The wrapping of specimens in tantalum foil sees increases in critical current density and irreversibility field compared to specimens wrapped in either hexagonal BN or ZrO_2 for the same experimental procedures and thermal treatment [**156**]. The addition of tantalum powder, also by Prikhna *et al*, to the precursor B and Mg powder mixtures showed further increases in these parameters [**156**].

3.7.4. Powder in tube

For the manufacture of mono- and multi-filamentary wires, the powder in tube (PIT) techniques are used, utilising commercial MgB_2 powder within a barrier and sheath arrangement, which is drawn and heat treated.

Continuous tube forming and filling (CTFF) is a patented technique invented by Hyper Tech Research, Inc., that can utilise either *in situ* or *ex situ* reactions [**157**]. CTFF allows for longer lengths of wire to be manufactured and requires less wire drawing, resulting in wire long enough for magnet winding, at a decreased manufacturing cost [**158**].

As mentioned in Section 3.3.5, PIT techniques suffer from the drawback of low density, which can be partially overcome by drawing and densification, but requires further annealing at high temperatures.

3.8. Technologies and applications

As MgB_2 is less expensive than HTS and provides adequate performance under magnetic fields, is it poised to enter many different areas of operation, most of which would be operating in the 20-30 K range, thereby eliminating the need for expensive and limited liquid helium cooling. These moderate temperatures can be achieved by cooling with liquid neon (LNe), liquid hydrogen (LH2), solid nitrogen (SN2), or by conventional closed-cycle cryocoolers. Possible applications using MgB_2 would be in magnetic resonance imaging (MRI), fault current limiters (FCL), transformers, magnetic separation, motors, generators, superconducting magnetic energy storage (SMES) devices, adiabatic demagnetisation refrigerators as well as in high energy physics (HEP) applications.

The key to successful adoption of MgB_2 in these applications primarily depends on the price per kA.m. With MgB_2, the cost of materials is low and the processes used in manufacture are relatively simple, which allows for low cost from the outset, but should also decrease as these processes improve and become cheaper. Manufacture of HTS relies on far more advanced and complicated processes to enhance texturing for optimum performance, often with the use of Ag as a stabiliser, which increases cost considerably. In comparison, the cost of copper wire is about \$20 /kA.m, whilst HTS costs \$150 /kA.m. The costs continually decrease as technology and processes improve, and the projected cost for YBCO HTS wire manufactured via techniques such as metalorganic chemical vapour deposition (MOCVD) is \$50 /kA.m [**159**]. MgB_2 has an envisioned cost of less than \$3 /kA.m [**160**], making it financially attractive if it can meet the application-specific performance metrics.

In order to be commercially viable, the performance of MgB_2 effectively needs to equal or exceed the performance of other LTS such as NbTi and Nb_3Sn. The main limiting feature is that whilst doping increases H_{c2} to respectable levels, it can begin to degrade the connectivity, and hence J_c, resulting in J_c's that are below that of NbTi. The connectivity, which is presently very low amongst most specimens, needs to be improved so that J_c may be improved and commercial viability met.

3.8.1. Superconducting magnets

In magnet systems, superconductor-based systems achieve higher fields than conventional iron-cored systems with copper windings, largely due to the lack of resistive losses. Particularly useful in persistent magnetic field applications, the lack of resistance in superconducting state ensures minimal field decay over period of months, requiring only conservation of the coolant. In addition, the high current density in the superconductor results in a size decreases.

At present, Nb_3Sn and NbTi operating at LHe temperatures dominate this application, due to the impressive performance figures and the development of superconducting joins that allow for lossless current flow throughout the superconductor and across joins. This milestone is likely the greatest contribution towards feasible use of Nb_3Sn and NbTi in NMR and MRI applications [**97**]. For MgB_2 magnets operating in persistent mode, solutions are required to overcome the issue of joins. Joins have been accomplished by introducing superconducting NbTi as an interface, and locating the join at a low field point [**97**]. The disadvantage is clearly due to the fact that the join would obviously be cooled down much further, to a temperature where NbTi is superconducting.

A practical issue for superconducting magnets is that of quench. For protection of superconducting devices when a coil quenches, it is best for the coil material to have a high normal zone propagation rate. The high normal zone propagation rate ensures that current in the superconductor is rapidly decreased, with dispersion of the energy taking place across a rapidly increasingly normal zone. This avoids the creations of hot spots that may burn out and cause damaged to the superconductor. YBCO coated conductors have a rate of 0.2-1.0 cm.s^{-1}, MgB_2 multi-filamentary wires may have rates of 15-50 cm.s^{-1}, whilst LTS such as NbTi and Nb_3Sn have rates that range between 1-100 m.s^{-1}. As a real-world example, an experimental conduction-cooled MRI prototype using an MgB_2 solenoid wound from a multi-filamentary conductor, achieved quench propagation of 7 cm.s^{-1} at 32 K [**161**].

A simulation comparison of a conceptual 1.5 T MRI for a hand imaging using an ellipsoidal racetrack coil configuration, showed that between NbTi operating at 4.2 K and MgB_2 operating at 10 K, the performance of the MgB_2 wire was sufficient to allow near-term feasibility [**162**]. In another test coil for MRI, a 1.5 T MgB_2 solenoid was cooled by SN2 [**163**]. The use of SN2 as a cryogen is appealing for superconducting magnets, as it allows for continued operation of magnets operating in persistent mode during brief power disruptions.

Superconducting magnetic energy storage

Superconducting magnetic energy storage (SMES) devices are used for the lossless storage of large amounts of energy in a superconducting magnet, the only such system that to store electrical energy in the form of electric current [**164**]. The devices can store up to mega joules of energy, and are used to increase power quality and perform load-levelling in power systems.

Due to the increased penetration of renewable energy sources (RES) into power systems – particularly photovoltaic (PV) and wind generation – SMES systems offer a high power and energy density solution to potential instabilities caused by the RES [**165**]. These two RES sources in particular suffer from both predictable and unpredictable time-dependant variability in generation capacity. The generation capacity of PV panels depends on the solar irradiance, which is affected by atmospheric conditions, weather seasons, and the temperature of the module. The generation capacity of wind turbines varies greatly due to the volatility of wind speed. As a result, the generation capacities follow a diurnal cycle, but remain otherwise highly unpredictable. SMES devices may be used to supply power to the grid in situations where this generation capacity decreases temporarily [**166**].

SMES devices are high speed devices able to respond to demand changes within milliseconds, and allow power response in all four quadrants to provide transient and dynamic compensation [**167**]. The fast response of SMES devices results in an increase in system damping and hence increased dynamic stability of the system [**168**]. The power conditioning system (PCS), which interfaces the superconducting coil to the power system, determines the performance of the SMES device, as power flows through it on both charge and discharge cycles; a high efficiency cycle with fast response times is required of the PCS [**165**]. It is also the PCS that allows the SMES to independently provide active and reactive power, damping oscillations and increasing system stability [**169**]. The advancement in the PCS and power electronics have resulted in SMES devices with excellent conversion efficiencies of over 95% [**165**, **170**]. A schematic is shown below in Figure 3-4.

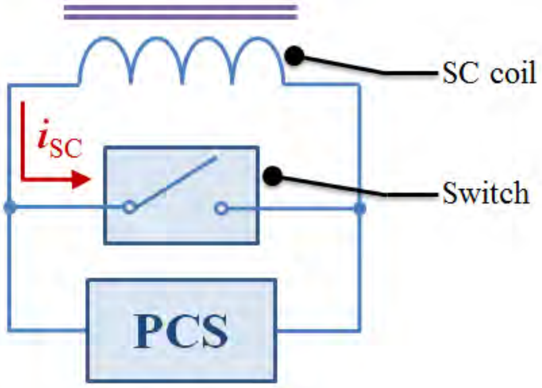

Figure 3-4 Schematic of a SMES device. The PCS injects current into the coil, and a short circuit switch then closes, keeping the coil operating in persistent mode.

SMES devices are solid state devices that do not suffer from time-based deterioration of the stored energy, resulting in devices with long lifetimes – over 100,000 charge/discharge cycles – making SMES devices appealing for loads requiring reliable, continuous modes of power operation [**171**]. Environmental impacts are minimised by the use of toroidal coils that reduced the magnetic field leakage [**172**].

At $10,000 per kWh [**173**], the devices are costly and it is essential that optimal sizing of the coil is performed, as determined by the application-specific power fluctuation levels and taking into account the losses during charging and discharging [**174**].

A major application area for SMES devices are for distributed energy storage and in microgrids (MGs). Microgrids are small, semi-connected grids, consisting of generation, storage and loads, and typically operate within a small area. Within the MG, the SMES offers numerous benefits [**169**]:

- It provides spinning reserve for contingency plans in the event of generation failures
- It promotes on site generation, thereby reducing transmission losses and contention
- It allows for the MG to provide bidirectional transfer of power to the main power system
- It allows the MG to operate in either grid-connected or island mode
- It increases the MG stability, due to the increase in damping
- It provides ride-through during generation dips, maintaining the MG for sensitive loads.

Typically NbTi has been used for the coil in SMES devices operating at 4.2 K [**175**], but recently MgB_2 has been found in an experimental SMES prototype operating at 20 K, cooled by LH2 [**176**]. In this prototype, the intended application involves installation next to a LH2 filling station for vehicles, providing a convenient cooling opportunity for the coil, which is rated at 100 MJ [**176**].

The primary challenges for the use of MgB_2 in the SMES coil are the low engineering current density, J_e, when operating in the 2-5 T range, and reduction of cost, as a large amount of superconductor is required for the coil [**157**]. It is predicted that J_e in multi-filamentary wires at 20 K will be improved from 200 $A.mm^{-2}$ at 2 T to 200 $A.mm^{-2}$ at 5 T, allowing MgB_2 to be competitive in this application [**176**].

3.8.2. Light-weight & space

Being composed of two elements with low densities, MgB_2 is well suited to light weight applications such as aircraft and space flight [**177**], where the cost of launch is determined by weight. In these applications, the superior performance of superconductors compared to conductors results in size and weight reduction. In addition, practical MgB_2 wires and tapes can be sheathed using other light weight elements, such as Ti [**178**] and Al [**179**].

Sheathing of the superconductor by Al is achieved using an *in situ* PIT technique with a 10 μm Mg particle size, allowing for low temperature processing at 600 °C [**179**]. Reduction in Mg particle size has been shown to allow good MgB_2 wires to be fabricated at temperatures as low as 540 °C [**180**]. A MgB_2 wire with an Al sheath can be a factor of 3 less dense than a NbTi conductor sheathed by Cu, whilst having comparable thermal conductivity at 20 K [**179**].

Sheathing by non-magnetic Ti results in significant improvements in mechanical properties, and doesn't require low temperature processing, allowing high temperature annealing for increasing J_c. The yield stress of Ti is a factor of 3 times higher than steel, yet is just half the weight, effectively bringing a 6 times increase in the weight-stress metric [**178**].

MgB_2 in particular is well suited for space applications, as it not only is it light weight, but also has the ability to operate at 20 K, which is above the temperature margins of NbTi and Nb_3Sn [**181**]. Unlike the fabrication techniques of HTS that constrain the final wire geometry to tapes, MgB_2 wires may be of circular cross section, which is advantageous for winding coils and reducing wire diameter. The HTS tapes, although thin, have very particular bending restraints that limit their application in small coils. As stainless steel (SS) sheathed MgB_2 wires may be drawn down to 50 μm, with much relaxed bending constraints compared to HTS, multilayer winding of coils is highly achievable.

Particular applications for superconductors in space are current leads, cryogen level sensors and for the magnets in active ionizing radiation shields. For current leads, 310 μm diameter SS sheathed MgB_2 wires were used in the 'Suzaku' satellite, designed to allow sufficient current transport whilst simultaneously providing a low thermal conductivity link over the operating temperature differential from 17 K to 1.3 K [**182**].

Cryogen level sensors can easily be constructed using a single superconducting wire with small diameter and hence low thermal conductivity. A current pulse with a magnitude of just less than the critical current of the wire is periodically applied, which turns the unsubmerged section of the wire into normal state. The length of uncovered wire in the normal-state determines the overall resistance, and hence the cryogen level can be measured by determining the resistance of the wire. Here only HTS and MgB_2 sheathed by SS can be used for LH2 level sensors, as the operating temperature of 20 K is above the critical temperature of LTS [**183**]. MgB_2 has shown to be effective in this application, due to the ease of manufacturing ultrathin wires, and the sensors based on MgB_2 show high linearity and reproducibility, small measurement error and no pressure dependence [**184**]. A diagram of the system is shown in Figure 3-5.

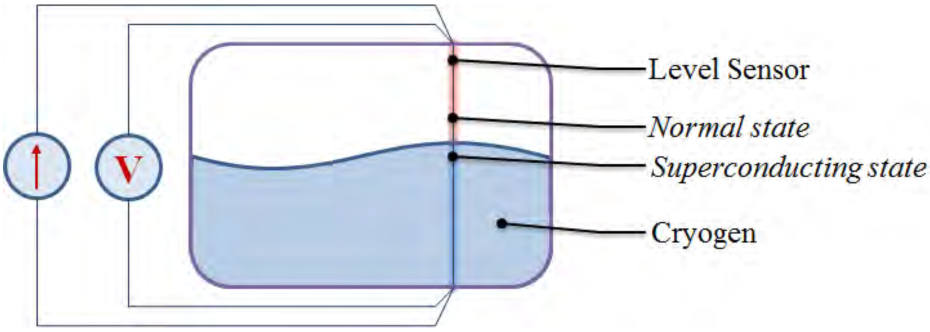

Figure 3-5 A superconducting cryogen level sensor. Through joule heating, a high current turns unsubmerged sections of wire normal, and a voltage is developed across the wire. Measurement of the resistance yields the length of wire exposed, and hence the cryogen level.

A long term application goal for the use of MgB_2 is in superconducting magnets as part of active shielding of space habitats against ionizing radiation for long duration manned spaceflight. In a passive scheme, an absorber is used to provide shielding, whilst in an active system, the radiation is deflected, as shown in Figure 3-6.

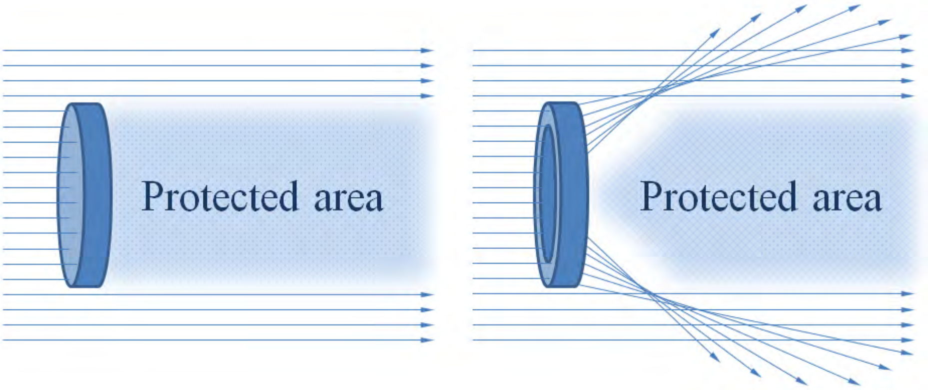

Figure 3-6 Passive and active shielding. A protected are may be established by the use of a passive absorber, or by an active magnetic lens.

In the choice between passive and active shielding schemes, the use of an active magnetic defocussing lens and support structure can weight 3 times less than a passive absorber, leading to immediate savings right from launch cost [**185**]. To optimise the power cost metric in the active scheme, it is necessary to achieve the required ampere turns for the magnet by minimisation of the current, and hence a maximisation of the number of turns. For winding such high numbers of turns, it is easier to use the smaller diameter wires provided by drawn MgB_2, instead of HTS tapes. The coils would typically be wound into a ‘Double D’ toroidal configuration around the habitat, a coil design that eliminates the magnetic bending moment, resulting in only hoop stress on the wire [**186**].

In many space missions there are large amounts of LH2 readily available, providing convenient access to cooling for MgB_2 or HTS. Alternatively, feasible cooling at 20 K may be achieved by passive cooling, via geometry design and maintenance of specific attitude to the sun, matching the heat absorbed to the heat radiated out to space [**187**]. Large magnetic system composed of MgB_2 wires can be passively cooled, aided by minimal additional (complimentary) cooling by either cryogens or cryocoolers, as a backup in case of passive cooling failure. Operation of LTS by passive cooling is incredibly difficult, if at all practically possible, due to the extreme geometric configurations required obtaining such a low temperature equilibrium.

3.8.3. Fault current limiters

In power systems, fault currents continue to be both difficult and costly to deal with. As grid complexity and distributed generation increases, the effective system impedance decreases, resulting in increased magnitude of fault currents. Various components in substations such as the switchgear and transformers need to have specifications great enough to withstand fault currents, which can be 20-30 times the nominal line current. These high currents result in a substantial increase in the cost to build a substation for a scenario that could never occur. In addition to the cost of the components in the substation, the support structures also need to be increased, as the 20-30 times increase in current results in a 400-900 times increase in the magnetic forces [**188**]. Fault current limiters (FCLs) are devices used to reduce the magnitude of fault currents. They have the ability to impose minimal influence to the power system under steady state, whilst providing automatic, near instantaneous current limiting. If FCLs are installed, the substation specifications can be relaxed, reducing costs. In addition, FCLs also facilitate the installation of new equipment at sites where previously, under-rated equipment or equipment operating at its upper limits prevented further installation.

Another issue is the impending arrival at the upper limit of switchgear, as increasing the interruption capacity of high voltage circuit breakers is especially difficult [**189**], and the introduction of FCLs may enable generation upgrades despite switchgear operating at the upper limits. Presently switchgear is used to interrupt the fault currents, but the break is made at the zero crossings, with full interruption only cycles later with the extinguishing of the arc [**188**]. In future, with proposed DC links between generation plants such as wind farms, there are no zero crossing for interruption by conventional switchgear to interrupt at, requiring the need for alternative interruption mechanisms. Superconducting FCLs (SFCLs) will be shown to be well suited to this, due to lack of AC losses.

FCLs may be active or passive. The passive variants typically utilise large inductors with high reactances to limit the current, but unfortunately dissipate considerable power under nominal load conditions, leading to a reduction in efficiency. Active FCLs may consist of high speed switches and superconducting devices that are able to minimise losses at steady state, whilst still offering adequate current limiting.

SFCLs are active devices that utilise the superconducting-normal transition and the accompanying zero-normal resistance and diamagnetic-paramagnetic state changes to limit the current. It then follows that there are two types of SFCLs: resistive and inductive.

Resistive

The resistive SFCLs utilise a series-connected superconducting element to limit the current via resistive losses in the conductor after a superconducting-normal transition. To minimise excessive conductor heating, shunt resistance is frequently added, from either conductor cladding and substrates, or intentional inclusion of discrete resistors. In superconducting state, the shunt resistor is shorted, but upon transition starts sharing current in the shunt element. This aids recovery time, as less energy is dissipated in the element that needs to be cooled again. A schematic of a resistive SFCL used with a circuit breaker (CB) is shown in Figure 3-7.

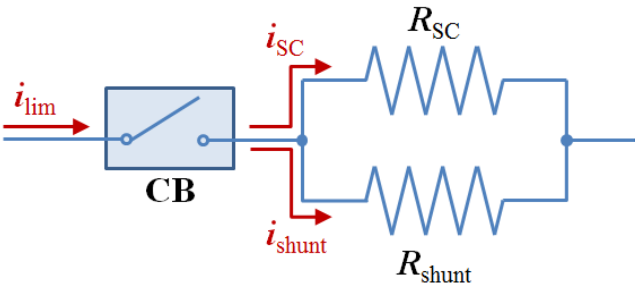

Figure 3-7 Schematic of a resistive superconducting fault current limiter with a circuit breaker (CB). Under normal conditions R_{SC} shorts R_{shunt}, and neglible impedance is referred to the power system. Under fault conditions, R_{SC} rises rapidly, and current is diverted through R_{shunt}, which then performs the current limiting.

Resistive SFCLs do not require iron cores, thereby reducing weight, size and cost, whilst also offering for more flexibility in layout options [**190**]. As the design is so simple, featuring only resistive impedance, the decay speed increased and the overall inductance of the power system can be reduced [**2**]. Internally, the coils are typically wound in a bifilar configuration, which is used for cancelling the generated magnetic field, thereby reducing the inductance of the coil and hence the AC losses [**191**]. The SFCL also helps in other areas of stabilisation, such as in the damping of the transient recovery voltage across the circuit breakers used to interrupt and reconnect the fault current, as well as damping upstream transient overvoltages [**190**]. This damping from the introduced resistance also reduces the power swing and torque oscillations on upstream generators [**2**]. In simulations, a resistive SFCL connected to a wind farm dramatically improved the voltage drop at the wind turbine terminals during a grid-side 3-phase short circuit fault [**4**].

For effective use in power systems, the device needs to return to zero resistance as soon as possible after a fault condition. Most utility operators will require SFCLs that can reclose on a subsecond timescale, which can be achieved in resistive SFCLs only if the conductor is kept within the superconducting bounds, which increases size, complexity and obviously cost of the SFCL [**3**].

A hybrid resistive SFCL provides another iteration of improvement, in that a fast switch is included in series with the superconducting element, allowing for full current diversion to the shunt element. This results in the least heating of the superconducting element, but requires high speed switching in order to be effective.

In designing resistive SFCLs, it is necessary to tune the parameters to achieve the desired limiting properties. The SFCL should present enough resistance to limit the fault current, which is achieved by design of the cross sectional area and length. An alternative approach is to reduce the volume of superconductor conductor required, by manipulation of the normal resistivity of the superconductor. From [**3**], it can be shown that

$$R = \frac{V_0}{I_{\mathrm{lim}}} = \frac{\rho L}{A} \tag{3.6}$$

Where R is the FCL resistance during fault, V_0 is the system RMS voltage, I_{lim} the desires fault current magnitude, ρ is the effective resistivity of the superconductor, and L, A are the superconductor length and cross sectional are respectively. The denominator of the rearrangement shown below indicates that for a constant cross sectional area, the length of superconductor required may be reduced as the resistivity is increased:

$$I_{\mathrm{lim}} = \frac{V_0 A}{\rho L} \tag{3.7}$$

The increase of resistivity does have implications on the thermal performance, as under fault conditions, a larger quantity of heat is dissipated per unit length of superconductor, but for a given cross sectional area, the length of superconductor (and hence volume, cost) can be reduced by increasing the effective resistivity.

Inductive

Inductive SFCLs use the diamagnetic and screening properties of superconductors to provide current limiting. The two main types that are used are shielded-core and saturable-core types.

In the shielded-core variant, a superconducting coil is placed between a core and a large copper winding. Under nominal load, the superconducting coil shields the core from the magnetic field established by the primary coil, and the core has no limiting effect. Under fault conditions, the screening current in the superconducting coil exceeds the critical current, and the superconductor transitions to normal state. Once in normal state, the superconductor no longer shields the core from the magnetic field established by the primary, from which point on the core properties will determine the current limiting action. The schematic is shown in Figure 3-8, where the system is shown as a transformer with a superconducting coil as the secondary, limiting after exceeding the critical current rating.

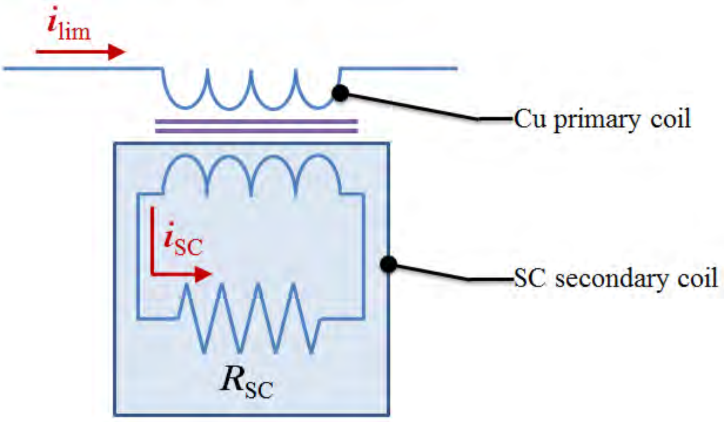

Figure 3-8 Schematic of a shielded iron core inductive superconducting fault current limiter. Current flowing in the primary causes current flow in the superconducting secondary

The saturable-core SFCL is similar to the shield core approach, but uses a DC superconducting coil to establish a large DC magnetic field in a core and driving it into saturation. AC windings on the core carry the load current, and the resultant AC magnetic field boosts and bucks the DC field, but under nominal conditions is not sufficiently large enough to drive the core out of saturation, and the current undergoes only minor distortion from the core. Under fault conditions, the magnetic field from the line current is sufficient to drive the core out of the extreme saturation region into the steep unsaturated section of the magnetisation curve. This results in a large increase in inductance, and the device behaves like an iron core reactor. The schematic is shown in Figure 3-9, where two cores are used to provide both in-phase and anti-phase limiting.

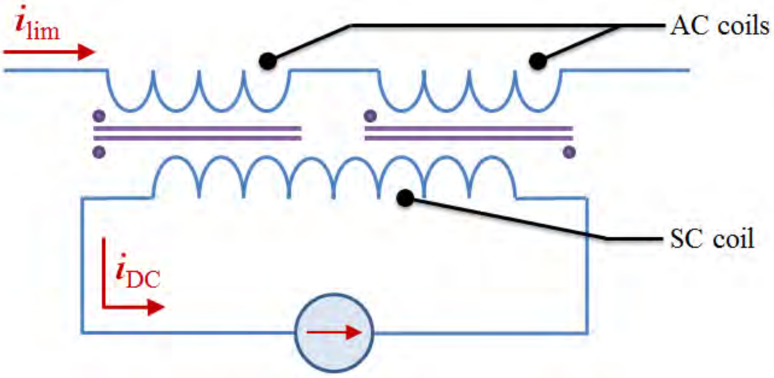

Figure 3-9 Schematic of a saturated core inductive superconducting fault current limiter. Both cores are saturated by the DC current in the superconducting coil. Any current through the AC windings that generate a great enough magnetic field will drive one of the cores out of saturation, introducing inductance that limits the fault current.

MgB_2 in FCL

MgB_2 is well suited to resistive fault current limiters, as it is low cost, features a sharp superconducting-normal transition, is easily manufactured in bulk, and can be operated at moderate temperatures [**157**]. The current limiting properties have been confirmed on desktop-scale tests [**192**].

As mentioned in Section 3.8.1, the normal zone propagation velocity is higher than HTS, which is useful for the avoidance of hotspots. In the case of HTS, sheaths need to have high thermal conductivity to stabilise the wire, which typically means a metal sheath likely to have low electrical resistivity too. In the case of MgB_2, the normal zone propagation velocity is high enough to negate the need for excessive thermal stabilisation, and instead the sheath can be manufactured with high resistivity materials [**157**]. Additionally, the use of SN2 introduces a phase change at 63 K, which consumes large amounts of heat energy during fault conditions. This has been found effective in HTS based SFCL systems [**193**], and the benefits are likely to be seen with MgB_2 systems.

Majoros *et al* compared mono- and multi-filamentary MgB_2 wires, finding that a multi-filamentary configuration with barriers of Nb, Cu, and a CuNi sheath showed the best performance in terms of low AC losses and high thermal stability [**194**]. Ye *et al* also compared mono- and multi-filamentary MgB_2, finding that both performed current limiting, but with different characteristics, indicating that the sheath plays an important role in quench behaviour [**195**]. Ye *et al* also found that the performance of the wire degraded as a function bending radius, and thus coils should be wound before annealing to avoid winding-process induced defects [**196**]. The use of bulk MgB_2 instead of wires is also possible, with bulk presenting the advantage of much higher density, especially when prepared using high pressure techniques [**197**].

3.9.Summary

Discovered to be superconducting in 2001, MgB_2 is the first superconductor with pronounced features of two-band superconductivity, and a rather high critical temperature of 39 K, placing it in competition primarily with the well-established NbTi and Nb_3Sn LTS markets.

MgB_2 does not suffer from grain boundary problems, and can hence be produced via many simple techniques whilst still retaining good magnetic properties. The upper critical field can be enhanced by doping, but consequently degrades the connectivity and critical current density.

Precursor powder plays a definitive role in determining the superconducting properties of MgB_2, with oxygen contamination resulting in formation of (Mg)B-O phases that reduce the current-carrying cross-sectional area, resulting in decreases in J_c.

Fabrication of MgB_2 can be performed via *in situ* reactions of Mg and B powders, or *ex situ* reactions involving MgB_2 powder. The reactive liquid magnesium infiltration technique offers a simple means to obtain high quality MgB_2 bulks with high density without the need for expensive or technical equipment used in other techniques such as high pressure.

Chemical doping of MgB_2 can be achieved by doping the precursor powders before an *in situ* reaction. Carbon can be introduced via chemical vapour deposition using a hydrocarbon gas source, but can also be introduced from the addition of solid or liquid hydrocarbons to the boron powder.

Different doping schemes may be implemented to modify the intra and interband impurity scattering rates for different purposes.

MgB_2 degrades in water and humid atmospheres, but the extent of this degradation is very much a function of the specimen morphology. Higher quality thin films undergo greater degradation at a faster rate, as contaminants found in lower quality films offer protection. In bulk specimens, specimens with poor connectivity and high porosity suffer most, as water can easily penetrate the grain boundaries, and results in the removal of platelets from the structure. Water from air acts as a catalyst in the phase decomposition of MgB_2 to primarily B_2O_3 and $Mg(OH)_2$.

Possible large-scale applications are: small diameter MRI for body extremities, space and lightweight technologies, SMES devices, and fault current limiters. Prototypes of all these potential applications have been developed. A key milestone for the use of MgB_2 in persistent mode superconducting magnets will be the development of superconducting MgB_2 joins.

For successful penetration into markets and to replace Nb_3Sn, it is necessary to obtain low-loss superconductor-superconductor joins, and to further enhance both the pinning properties and critical current densities simultaneously, at an overall cost that is commercially comparable to Nb_3Sn and NbTi.

Chapter 4 Experimentation

For the investigation into carbon doping on the normal resistance of MgB_2, specimens were prepared by the reactive liquid infiltration technique, with the precursor boron powder doped by carbon chemical vapour deposition using ethylene gas. Bulk specimens were cut into slices and bars, and various contact methods were investigated. Specimens were inserted into purpose-built apparatus to undergo resistivity and AC susceptibility characterisations.

4.1. Doping

For the chemical vapour deposition (CVD) of carbon to the boron precursor powder, a purpose-built stainless steel tubular furnace assembly was used in conjunction with the gaseous hydrocarbon ethylene (C_2H_4) as the carbon source. The assembly consisted of a stainless steel tubular section that was installed into a horizontal tube furnace. The stainless steel insert was designed to make use of readily-available high temperature O-rings, and the inner diameter (ID) was selected to allow for maximum precursor powder tray sizing. The ID of 54 mm allowed for a loading tray of 43 mm width and 200 mm length to be used, which translated to a maximum powder load of about 3 g, determined by appropriate even spreading over the surface of the tray.

To prevent contamination of the precursor powder from the stainless steel tray, the boron powder (Sigma-Aldrich, 95-97%, amorphous, submicron particle size) was loaded into an inner tray manufactured from molybdenum sheets. The molybdenum tray proved to be well suited to this purpose, as there was minimal adhesion of the boron precursor powder to the surface during unloading, and very little product loss was observed during subsequent cleaning of the tray with ethanol.

Initial tests revealed powder contamination was possible upon removal of the tray from the furnace, in the form of loose carbon flakes that had deposited on the inside of the stainless steel tube. To avoid this contamination, a molybdenum shield was constructed that would cover the molybdenum tray from above, whilst still allowing for ethylene gas flow through the shield. The tray components are shown below in Figure 4-1.

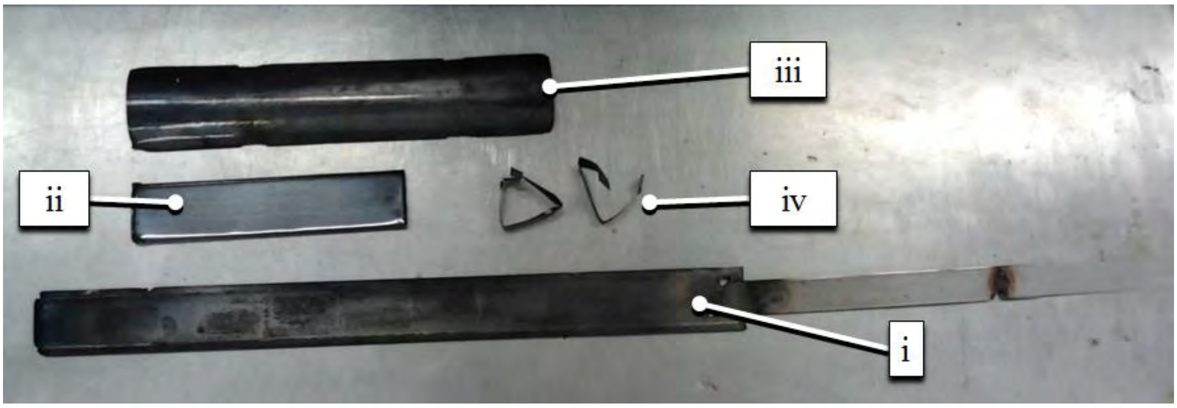

Figure 4-1 Components of the doping apparatus: (i) stainless steel tray, (ii) molybdenum tray, (iii) molybdenum shield, and (iv) molybdenum straps.

At 320 mm in length, the shield was designed to be substantially longer than the molybdenum tray, to minimise the chances of carbon flakes ‘flicking’ in through the large side openings. The assembled tray with molybdenum shield is shown below in Figure 4-2

Figure 4-2 Assembled doping apparatus. The molybdenum tray loaded with boron powder is protected from contamination of carbon flakes by the molybdenum shield. This assembly is placed in the stainless steel tube and inserted into the furnace.

Ethylene was used as the process gas, providing the source for carbon deposition. The stainless steel tube was loaded with the stainless steel and boron-loaded molybdenum trays, before being flushed with argon gas. After flushing, the ethylene gas was introduced into the tube, to a relative pressure of 80 kPa. The furnace was then heated to 600 ºC for 1 to 6 hours to obtain different doping levels.

Measurement of the carbon content was achieved by measurement of the boron precursor powder mass before and after CVD. Measurement was done with a Mettler Toledo PB3002-S, with the scale initially zeroed with the unloaded molybdenum tray. The powder was spread evenly over the tray, to maximise the surface area exposed to the process gas. The loaded molybdenum tray on the scale is shown below in Figure 4-3, noting that the tray is lightly tapped after measurement to further enhance the surface area presented by the powder.

Figure 4-3 Boron-loaded molybdenum tray on the scale. Boron powder is evenly distributed over the surface of the tray to maximise surface area presented for deposition.

It was found that doping to higher levels could be achieved much faster by regular replacement of the hydrocarbon source. The ethylene in the tube was flushed hourly at the 600 ºC operating temperature for a total doping period of 6 hours, to obtain doping concentrations up to 21%.

For the specimens with results presented in this dissertation, the different carbon doping levels were obtained by various mixing ratios of undoped boron powder and 21% doped boron powder - the highest achieved by the CVD process. The powders were thoroughly mixed by hand with a mortar and pestle to maximise homogeneity. The process of using CVD to dope powder and then mixing with undoped powder does somewhat defeat the benefit of the intrinsic homogeneity associated with CVD, but the CVD still provided an effective means to introduce carbon additions with small particle size to the boron powder. Mixing ratios were calculated for a mixture mass of 1 g, which allows for a generous 0.15 g loss during milling, and are detailed below in Table 4-1.

Table 4-1 Mixing ratios of 21% doped boron, and undoped boron powder to obtain 1 g masses of specific doping concentrations

Desired Doping (%)	Mass of 21% doped boron (g)	Mass of undoped boron (g)	Sum (g)
0.00	0.00	1.00	1.00
4.00	0.19	0.81	1.00
8.00	0.38	0.62	1.00
12.00	0.57	0.43	1.00
16.00	0.76	0.24	1.00
20.92	1.00	0.00	1.00

4.2. Reactive liquid infiltration

Specimens were manufactured by the reactive liquid infiltration (RLI) technique, as discussed in Section 3.7.1, in appropriately designed stainless steel containers. In all cases, the grade of stainless steel used was 316. A number of iterations on the designs were made, to improve various aspects; easy of removal of product, easy of welding crucibles, increasing internal reaction pressure, and minimising stainless steel volume and machining time.

The first iteration consisted of stainless steel round bar of 25 mm diameter, with a cylindrical hole of 10 mm diameter bored from one end, and was used in conjunction with a stainless steel cap machined to fit the hole, enclosing a cylindrical volume of 0.5 cm^3 when shut. The sides of the enclosed volume were first lined with molybdenum foil to allow for easy removal of the MgB_2 product, and 'charged' with the boron powder. The boron powder was pressed using a 15 ton press to the required density of 1.185 $g.cm^{-3}$, corresponding to 50% the natural boron density of 2.37 $g.cm^{-3}$ [**148**]. A magnesium pellet machined from magnesium round bar (Alpha Aesar, 99.8%, 3.3 cm dia.) was placed on top of the boron powder, and the stainless steel lid was then TIG welded shut. The crucible design is show below in Figure 4-4, and the crucible, after welding, is shown in Figure 4-5.

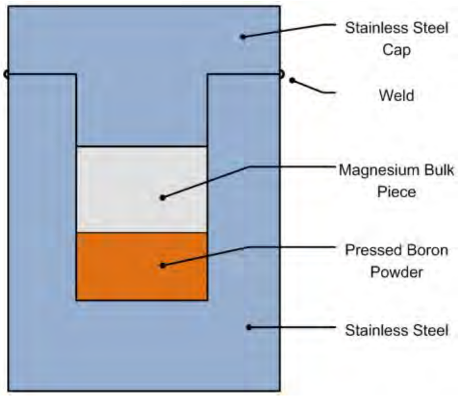

Figure 4-4 RLI crucible design version 1.

Figure 4-5 RLI crucible (version 1) after welding.

The welded crucible was subjected to heat treatment at 850 ºC for a duration of 3 hours, then furnace cooled to room temperature. The crucible was machined open using a lathe to cut through the weld seam. The product was somewhat difficult to remove, owing to the expansion and deformation of the crucible walls during reaction. To avoid this, a second iteration of crucible design was developed, with the primary design objective being easy removal of the MgB_2 product.

The improved design (version 2) was similar, with the key difference being that the precursor powder and magnesium pellet were loaded into a second, smaller, cylindrical tube made from standard 19 mm stainless steel instrumentation pipe. The concept was that the inner tube could be removed somewhat forcefully from the outer crucible, whilst still protecting the integrity of the MgB_2 pellet inside. One removed, the 1.2 mm walls of the tube could easily be sliced open by band saw, and the in-tact pellet removed. The design is shown below in Figure 4-6.

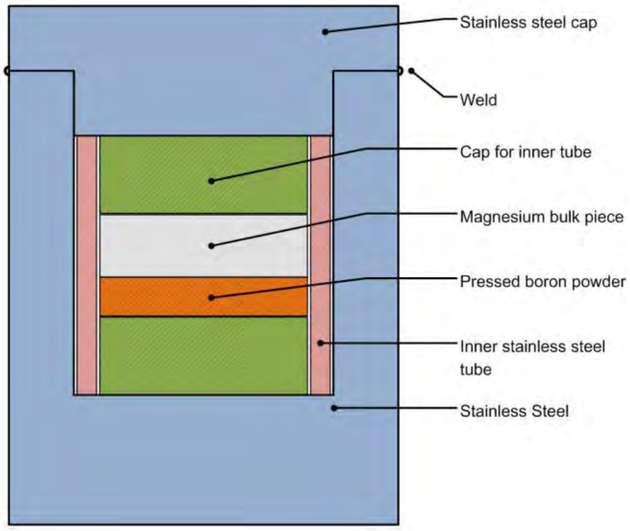

Figure 4-6 RLI crucible, version 2. A stainless steel tube was charged with the reagents, and loaded into the crucible, providing protection to the product during removal.

This crucible design produced bulk pieces that were indeed easy to remove, but a lack of homogeneity was observed under optical microscope. This was attributed to lower reaction pressures due to the increase in free space within the reaction volume. Free space was minimised and thermal conduction maximised by insertion of molybdenum foil at the interface between the inner tube and the crucible walls. The foil aided in avoiding the inner tube from fusing to the crucible walls reaction, but it was felt that this additional stainless steel and molybdenum interface provided too many free spaces that could not be closed before reaction, resulting in decreased reaction pressure.

The preparation time for specimens produced in this crucible was considerably increased due to preparing the molybdenum foil that surrounded both the specimen and the inner tube, and the increased amount of machining required. Although the increase in machining time was not initially significant, as only a few were made, it became significant for the manufacturing many specimens. Due to the limited mechanical workshop time available, it was thus necessary to decrease the machining time required for the next design iteration, which was to increase the quality of the product, whilst still maintaining ease of product removal.

After discussions with the staff in the mechanical workshop, a final design was constructed. This design was much faster to machine, and required less molybdenum foil and less stainless steel. The crucible was made by boring a hole through stainless steel round bar to produce a thick-walled stainless steel tube, and sealed on either end by stainless steel caps. The design is shown below in Figure 4-7.

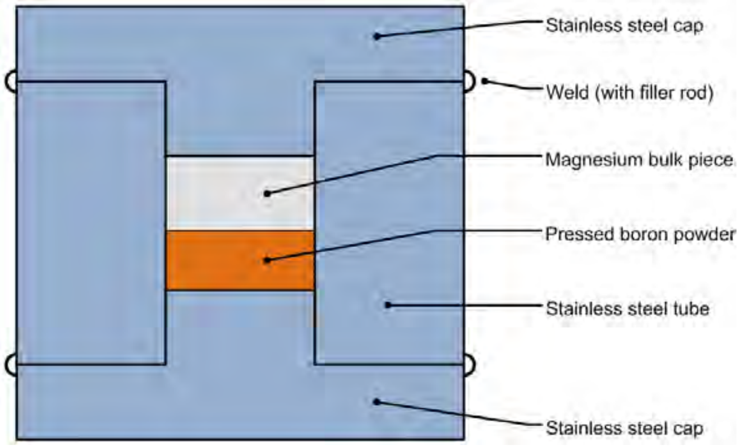

Figure 4-7 RLI crucible, version 3. Crucible wall thickness was increased to increase reaction pressure, and simpler design resulted in less machining and preparation time, as well as reduced stainless steel cost.

This design featured increased wall thickness from 5 mm to 10 mm, and minimised free space in the reaction volume by removing the molybdenum-stainless steel interface previously introduced. The product was removed in a two-step process; first a lathe was used to cut through the weld seems so the end caps could be removed, then afterwards, the stainless steel tube with exposed product was placed in a hydraulic press, and the product was ejected. As an intermediate interface between the crucible and the product, the molybdenum foil provided a coupling that was much weaker than the product, and would allow for the product and molybdenum foil to slide out without any cracking of the product.

This design evidently provided a significant increase in pressure during reaction, as frequently the weld seams would fail. Initially the failures were attributed to poor visual inspection of the welds, but blame subsequently shifted to the welding techniques used. All previous crucibles had been sealed by fusing the components with TIG welding, but this proved insufficient for this design, so the size of the weld seams were increased by the addition of stainless steel filler rods during welding. This meant that the weld could meet a certain size criteria that could be verified visually, as opposed to when the components were fused together without filler rods, where fusing depth was unknown. It also provided an effective means to deal with a crucible that did not tightly close. A typical weld failure is shown below in Figure 4-8(a), with Figure 4-8(b) showing the deformation of the 10 mm thick stainless steel lid due to reaction pressure.

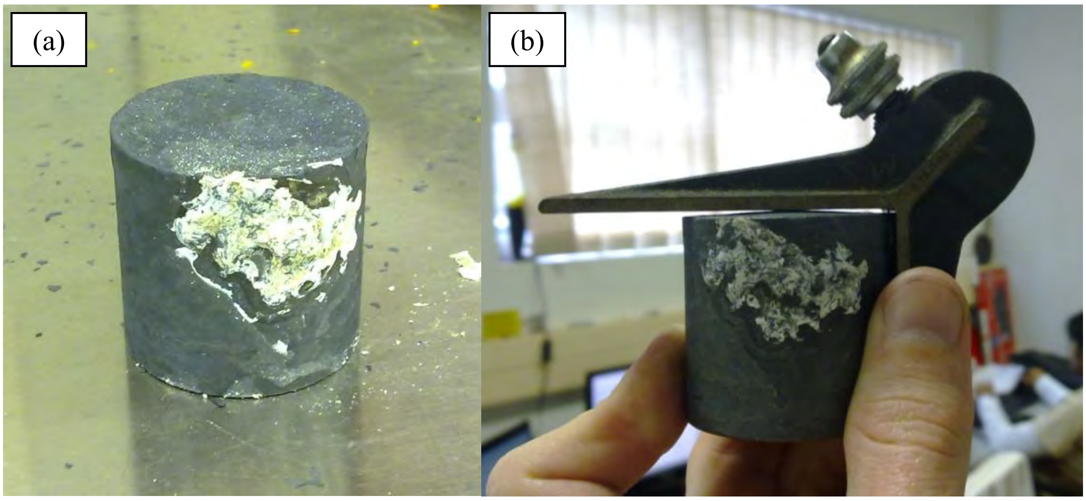

Figure 4-8 A crucible showing evidence of a weld failure. The white product in (a) was identified as MgO, formed by the reaction between the magnesium as it escaped the crucible, and the atmosphere within the furnace. The deformation of the crucible due to the internal reaction pressure is shown in (b).

The latter crucible design was used for all the results presented. Six crucibles were machined and lined with molybdenum foil, then charged with the doped boron powders. The doping ratios obtained were 0%, 4%, 8%, 12%, 16% and 21%. In each case, a mass of 0.86 g of precursor powder was charged, and an excess of magnesium bulk was added to ensure full reaction with the boron powder. The magnesium bulk pieces were cut from the magnesium round bar on a precision lathe, to obtain rods of 19 mm diameter and 2.7 mm height with a mass of 1.46 g. Crucibles were uniquely identified by drill marks engraved on the crucible caps, with the bottom cap receiving an additional drill mark so that all crucibles could be oriented in the same direction during heat treatment. Empty crucibles are shown below in Figure 4-9(a), and with identification marks in Figure 4-9(b).

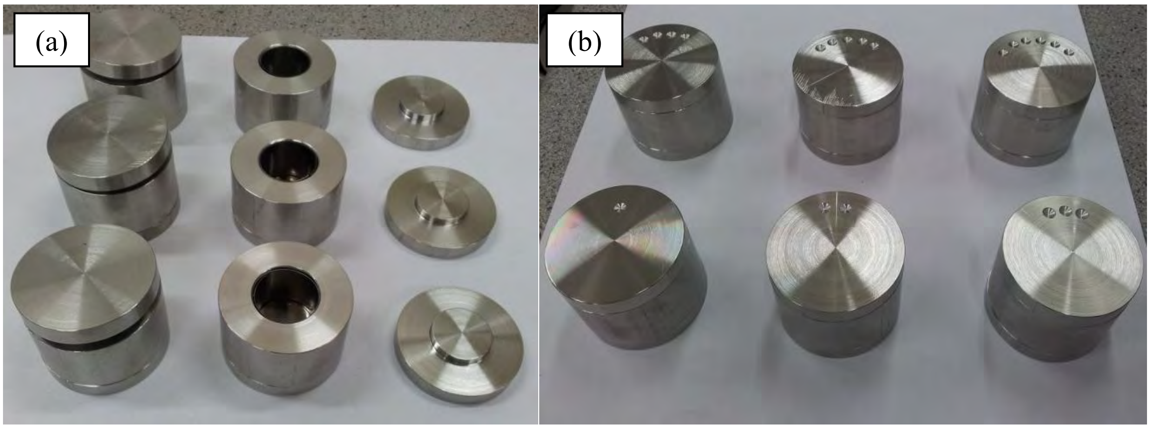

Figure 4-9 RLI crucibles (version 3). The inside of the tubes shown in (a) are darker due to the molybdenum foil lining, and unique identification of crucibles was achieved by decimal coding, shown in (b).

The precursor powder in the crucible was pressed by hand periodically during loading, and the final pressing of the powder to 50% natural density was performed with a powered hydraulic press, after loading of the magnesium pellet and the stainless steel lid. The magnesium rod mass and height were calculated to provide an excess of magnesium, and to ensure that once the crucible lids met the crucible tube, no free space would remain above or below the specimen, and the boron would be pressed to 50% natural density.

After pressing and TIG welding, the crucibles were loaded into a furnace, and heat treatment was initiated. The heating profile is shown below in Figure 4-10.

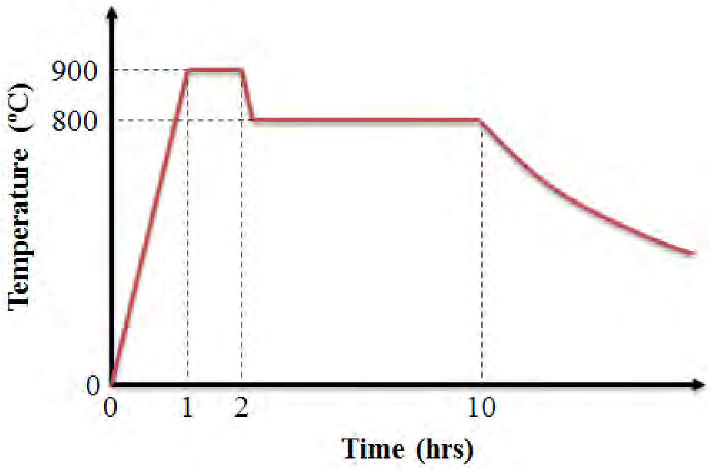

Figure 4-10 Heating Profile

The specimens were heated up to 900 ºC for a duration of 1 hour, after which the temperature was set at 800 ºC for a further 8 hours. The specimens were then furnace-cooled back to room temperature over approximately 14 hours.

After completion of heat treatment, it appeared that either one or two crucibles had leaked: the 4% and/or the 21%. The crucibles had been placed physically close to one another, to ensure minimal differences in heat treatment due to thermal gradients within the furnace. Indications of a leak were found at the interface between the 4% and 21% crucibles, as a substantial amount of magnesium oxide was present. Post heat treatment visual inspection did not reveal the site of the leak on either crucible, but it was determined from the final product that 21% had leaked, as the product remaining in the crucible consisted of unreacted boron precursor powder. It was also found later, that this leak also affected the 4% specimen, as discussed later in Section 5.2.

Using the reactive liquid infiltration technique, five bulk specimens of MgB_2 were produced. By visual inspection, these specimens appeared to have good density, and were sectioned into slices for resistive testing and into rectangular bars for AC susceptibility investigations.

4.3. Cutting

Cutting of specimens from the bulk pellets was performed using a Buehler low speed saw and a diamond sectioning blade. In the laboratory, sectioning of specimens had been previously performed utilising water as a coolant for the diamond blade, to which degradation of the superconductor was noticed. Thus, for the specimens presented in this research, acetone ($(CH_3)_2CO$) was used as the coolant in the cutting process, as it does not degrade the superconducting properties [143]. In order to obtain thin sections, it was necessary to set the specimens in an epoxy prior to cutting, so that specimens could benefit from increased mechanical structural support during the cutting process. The necessity of the epoxy changed based on the density and morphology of the specimens, as typically specimens with higher densities did not require support during cutting. The cylindrical disc-shaped specimens extracted from the stainless steel crucibles were potted, and sliced into multiple thin sections, giving slices with two parallel sides. Dependent on the size, some thin sections were potted again to give mechanical strength before cutting the remaining two sides. For resistive testing, a small cross sectional area is desired, as this will minimise the current required during measurement, which leads to decrease joule heating in the current leads. Larger sections were also cut from the bulk for AC susceptibility.

4.4. Specimen contacts

To perform 4-wire resistivity tests, it was first necessary to find a means of connecting four wires to the specimens. Substantial time was spent investigating methods to obtain good electrical contacts, with sufficient strength to avoid breaking off during mounting and cool-down, where differing thermal expansion coefficients placed stress on the contacts. After sectioning one of the undoped specimens to a cross sectional area of 1 mm x 1 mm and a length of 10 mm, various attempts were made to attach leads to the specimen, and a summary of techniques and results are discussed below.

Silver paste and silver wire

Silver paste was used to join thin silver wires to a cleaned MgB_2 surface. A band of silver was painted around the specimen, and the silver wire wrapped a few times around the band. Silver paste was then applied over the top of the wires, to maximise conduction from the wire to the silver paste. The design is shown below in Figure 4-11.

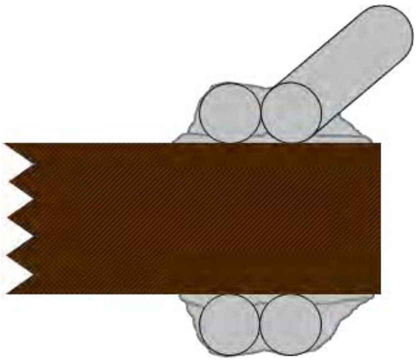

Figure 4-11 Contact using silver paste and silver wire. Silver paste was painted onto the MgB_2 surface, then silver wire was wrapped around the specimen, and finally painted with silver paste again.

The resultant connection provided sufficient electrical performance, but did not meet the mechanical strength criteria. This was due to the fact that the silver wires were so thin, and soldering to the wires was difficult and very delicate.

Silver paste and copper wire

As the silver wire was the clear weakness in the design, it was replaced with copper wire. The copper wire had a greater wire diameter for greater strength, and presented no soldering issues. As before, the wire was wrapped around the specimen to increase strength of the join and provide more surface area between the copper and the silver paste. This ensured that the copper did not pull away from the silver paste, but unfortunately caused the entire contact to break free from the MgB_2 surface, indicating that in this scenario it was the silver-MgB_2 interface that was too weak. The design is shown below in Figure 4-12.

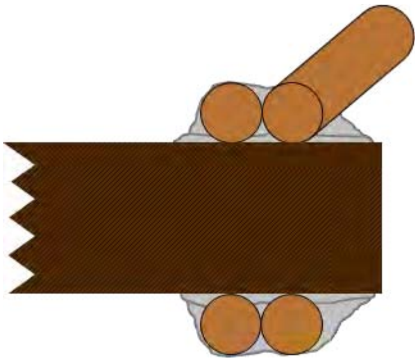

Figure 4-12 Contact using silver paste and copper wire. Copper wire was stronger, and replaced the silver wire.

Indium foil and copper wire

Instead of silver paste as the interface to the MgB_2, contacts were made using indium and copper wire. Due to the high ductility, freshly-scraped indium foil could be sliced into a small pad, and pressed onto the MgB_2 surface, and the copper wire wound around the specimen and into the foil. Some test specimens had additional indium bulk pieces sliced from an indium slug, and placed on top of the copper band, and raised to a temperature of 200 °C using a hot plate, melting the indium bulk. The design is shown below in Figure 4-13.

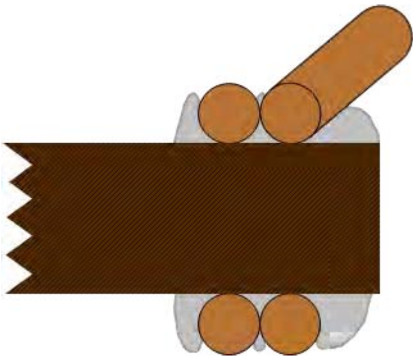

Figure 4-13 Contact using indium and copper wire. Indium was used to increase the pad adhesion to the MgB_2 surface.

Although the indium-MgB_2 join was stronger than the silver-MgB_2 join, it too failed under modest strain, so it was necessary to find further improvements.

Gold sputtering, silver paste and copper wire

To improve the both the electrical conductivity and mechanical strength, a gold pad was sputtered on the surface of the MgB_2 before application of silver paste. Silver paste was used, as it was easier to paint the band around the MgB_2 rather than press indium foil on all the sides. The gold particles increased the effective contact area by filling in the microscopic cracks and valleys on the surface of the specimen, created during the sectioning by diamond blade. This aided mechanical strength, and increased conductivity due to the great increase in conduction surface area. The design is shown in Figure 4-14 below.

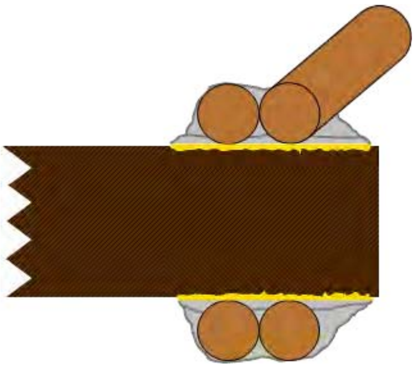

Figure 4-14 Contact with gold, silver paste and copper wire. Gold sputtering increased conductivity due to increased conduction surface area.

This contact technique was unfortunately rather inconsistent, as some contacts were strong, whilst others were weak. It was thus necessary to either solve the issue of inconsistency, or to reduce the time taken to identify inconsistencies.

Copper hooks

Taking the approach of decreasing contact evaluation time, contacts were made using copper hooks. These copper hooks were forged by flattening copper wires of 0.8 mm diameter, and after cleaning, were shaped with pliers.

The specimen was inserted into the hook, which provided a certain amount of spring force onto the specimen. Electrical contact was made on the top and bottom of the specimen, which is rather beneficial for current contacts. Without any solder or paste as depicted in Figure 4-15, the contact could rotate on the specimen, but was still able to maintain a certain degree of contact.

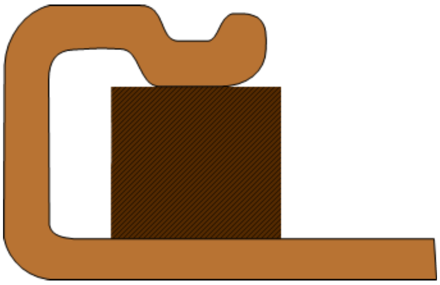

Figure 4-15 Contact made with copper hook.

Poor contacts could easily be identified, and due to the simplicity of the hook design, these poor contacts could be corrected easily. To improve on this design, gold was sputtered onto the top and bottom of the specimen, as well as on the inside of the copper hooks. Sputtering on the inside of the hooks was achieved by sputtering onto the cleaned copper surface before it was shaped into a hook. The gold-gold interface would provide a good electrical contact in the event of the hook moving. The gold plated arrangement is shown in Figure 4-16 below.

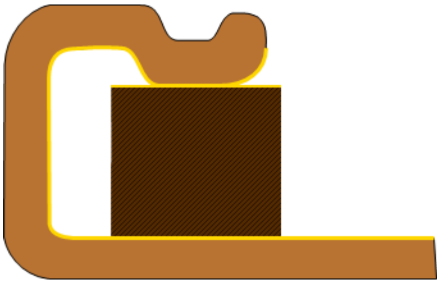

Figure 4-16 Gold sputtered surfaces on the hook contact increased contact integrity in the event that the moved.

Whilst the gold improved the electrical conductivity when the hook moved, an attempt was made using indium, to reduce the likelihood of the contact moving, as depicted in Figure 4-17.

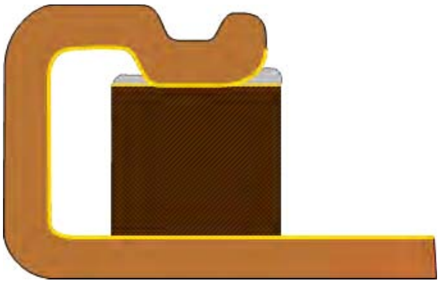

Figure 4-17 Contact hook with added indium to prevent the hook moving.

Indium foil was placed between the two gold surfaces to increase the stiffness of the contact. Unfortunately when the hook did move, the indium and gold pulled away from the MgB_2 surface, significantly increasing the contact resistance.

In addition to the issues discussed above, the hook structure introduced issues for mounting the specimen in a cryogen-free environment. The size of the copper underneath the specimen limited the surface area used for conduction cooling, but would obviously present no such problem for liquid cryogens and vapour cooling systems.

Pogo pins

To facilitate the rapid testing of multiple specimens, a solution was found in the form of spring loaded test pins (‘pogo pins’), typically used for in-circuit testing of populated printed circuit boards. These pins are gold plated, and can simply be pressed down onto the clean MgB_2 surface to make a contact, without requiring any other surface treatment.

An apparatus was built to test the contact method, and included mounting the pins in a 10 mm thick Perspex® lid, which was bolted to the copper sample mount. Holes in the lid were machined accurately using a milling machine to give pin a spacing of 4 mm between each pin, and the lid was bolted to the sample stage so that the pressure onto the specimen could be adjusted. The apparatus is shown below in Figure 4-18.

.

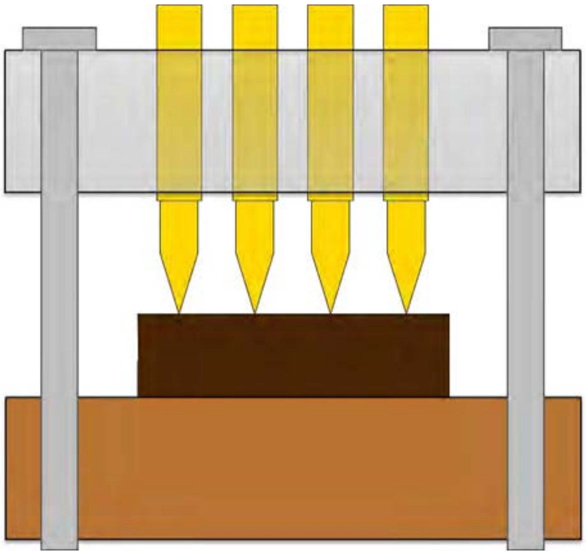

Figure 4-18 Pogo pin apparatus. Four pogo pins are mounted in a Perspex® lid, which is bolted to the copper sample mount. Pressure adjustments are possible by tightening or loosening the bolts.

Due to the thick gold plating on the pins, soldering the leads to the pins was trivial, and any accidental forces on the leads would be transferred to the Perspex® and sample holder instead of to the contact – a significant benefit. The spring loading ensured each pin would make contact regardless of even significant irregularities in the specimen surface, and also ensure that contact would remain during cooling, despite differences in thermal expansion coefficients. The failure of other contact techniques would result in one or more contacts 'floating' above the surface of the superconductor, but in this design, the spring force counters this, so pins will never be left floating.

The various contact techniques suffered primarily from poor mechanical strength, with the exception of the pogo pin apparatus, which was used for all of the resistive tests carried out on the specimens. This apparatus proved to be reliable with high reproducibility, as indicated by little or no deviation in measurements through multiple load/unload cycles. In addition, although the cost of the pins is high from an electronic component point of view, because it is reusable it is more economical than the other methods investigated.

4.5. Resistive testing

Thin sections of MgB_2 were cut from the bulk, typically measuring 2 mm x 1 mm x 13 mm. This was found to be the smallest specimen size that could be cut reliably, as lack of homogeneity in density resulted in areas of the specimen having poor mechanical strength. Specimens were tested in a purposed-built copper stage and sample holder, and affixed to an electrically-insulating sheet of mica using Apiezon® N thermal grease. The insulation was used to ensure that the specimen being tested was isolated from the high-conductivity copper stage. The four-wire resistance stage with the four spring-loaded test pins was then attached. Spring force from the test pins ensured good electrical contact despite any differences in thermal expansion coefficients, and also ensured contact force between the specimen and mica sheet.

As the body diameter of the spring-loaded test pins was 2 mm, the pins were spaced at 4 mm to provide sufficient support from the Perspex lid. The spacing resulted in a distance between the current pins of 12 mm, and a distance between voltage pins of 4 mm. The large spacing between current and voltage pins aided the change from point current injection towards a uniform current density [77]. The spacing of 4 mm between voltage pins presented a disadvantage of low signal levels, as ideally this spacing should be maximised to increase the signal level for the same excitation current. The setup is shown below in Figure 4-19, showing the 2nd stage of the Cryomech GB15 cold head, the heater stage, PT100 thermometer, sample mount and four-wire apparatus.

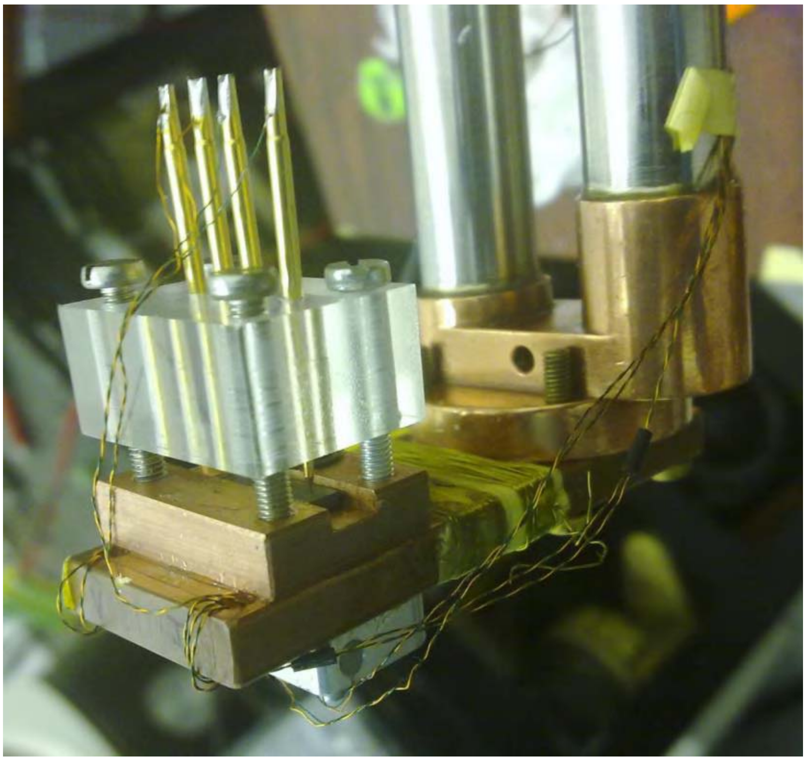

Figure 4-19 Apparatus for resistivity measurements. The gold plated spring-loaded test pins are used to make electrical contact to the specimen.

After mounting a specimen and confirming room temperature continuity and resistivity, a copper radiation shield and multi-layer insulation were mounted around the stage to reduce radiation losses. The installed copper radiation shield is shown below in Figure 4-20, and after installation with multilayer insulation in Figure 4-21. The combination of the two shields allowed the sample stage to be cooled down to below 13 K - the calibration limit of the thermometry.

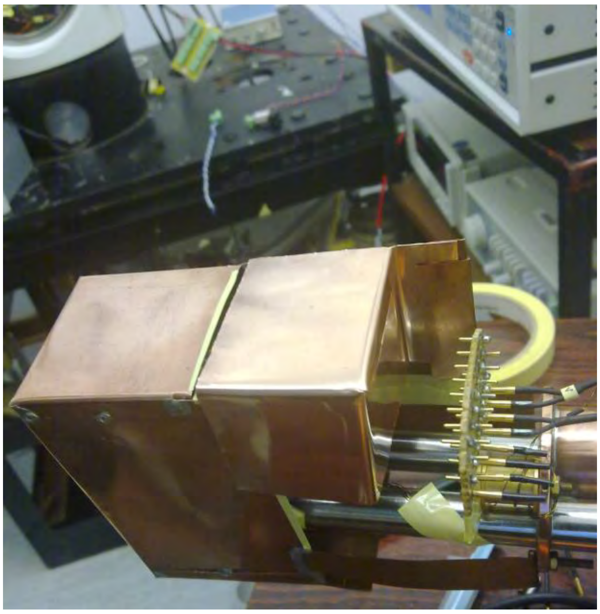

Figure 4-20 The copper radiation shield surrounds the sample stage and is thermally and physically anchored to the 1st stage of the cryocooler.

Figure 4-21 Multi-layer insulation wrapped around the radiation shield decreases the radiation losses to the 1st stage of the cryocooler, allowing it to reach lower temperatures, and subsequently allowing the 2nd stage to reach temperatures below 13 K.

Due to the low resistivity of MgB_2, the voltage developed across specimens at room temperature was very small. As discussed previously, the resistivities measured for MgB_2 vary greatly, but for a resistivity of 100 μΩ.cm, a specimen cut to the required dimensions would have a resistance of 2 mΩ. When excited by a current of 100 μA, a voltage of just 200 nV would be developed over a voltage pin spacing of 4 mm. A few attempts were made to measure these signals, using hardware that was readily available.

An IOTech DaqBook 2001 Ethernet-based data acquisition system was first used in conjunction with a Lake Shore Model 120 current source, as both were readily available in the laboratory. The DaqBook interfaces with DASY Lab software over the Ethernet connection, which allows for custom data collection and processing to be implemented easily. The current source was set to 1 mA, to increase the signal levels, but still remained too small and were masked by high levels of noise and quantisation error.

The use of a Lake Shore Model 336 temperature controller proved to be the next most feasible attempt, as it featured an internal 1 mA current source with current auto reversal options, filtering, and a resolution of 100 µΩ. The model 336 temperature has 4 sensor inputs, and so a specimen could be wired to mimic a thermometer, and the resistance could then be successfully measured by the controller. The drawback to using the controller as the measurement device was the limited resolution, which did not provide sufficient definition of the transition from normal to superconducting state - despite the filtering and adequate noise rejection.

Historically, the laboratory had focussed on high temperatures superconductors that featured a much higher resistivity. An unfortunate by-product of this was that the data acquisition systems that had been used successfully in the past, did not have the specifications to perform measurements on MgB_2. Thus, no equipment in the laboratory was found to provide enough sensitivity for measurement in the 100 nΩ range, so a Fluke model 8508A reference multimeter was loaned from the calibration laboratory. As this meter was intended to be used to calibrate other multimeters, it lacked features standard on most data acquisition systems, so certain compromises were made. Measurements had to be taken at a nominal current of 10 mA provided by the Fluke, which was much larger than typically used, as joule heating and the suppression of T_c occurs. Nevertheless, results to a resolution of 100 nΩ were obtained and showed clear trends of the normal to superconducting phase. The setup of the apparatus is shown in Figure 4-22.

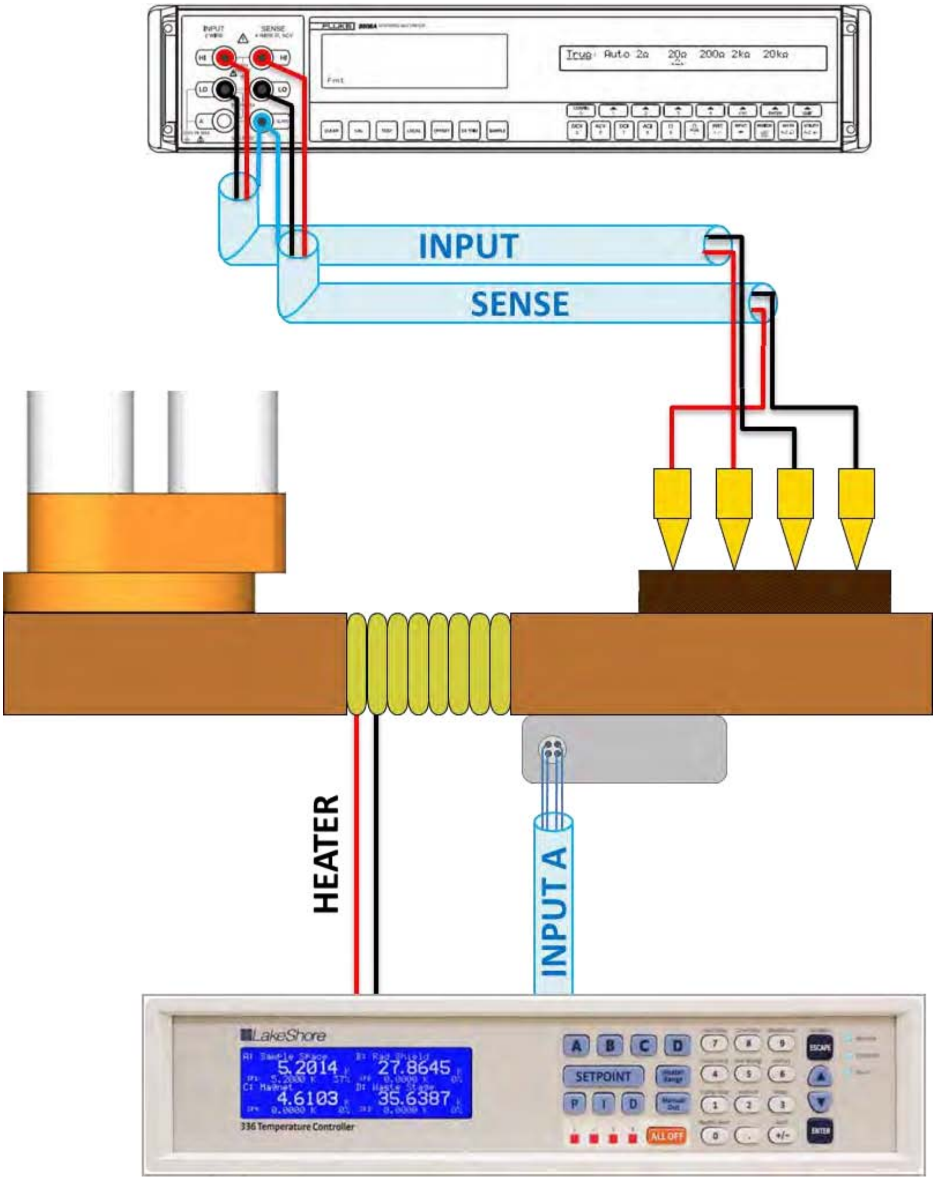

Figure 4-22 Apparatus used for resistive testing: the specimen is mounted to a temperature controlled copper stage. The Lake Shore temperature controller, Cryomech cold head, nichrome heater and PT100 thermometer are responsible for temperature control, whilst the Fluke multimeter is responsible for resistance measurement.

Temperature control was achieved by the use of a Lake Shore Model 336 temperature controller, a self-wound nichrome heater, and a calibrated PT100 thermometer attached to the stage right next to the heater. The heater was driven by a PID output from the controller, and stability was typically within 50 mK. To minimise error caused by thermal lag between the temperature control point and the sample mount, a delay period of 300 seconds was employed before taking measurements once temperature stability had been reached. To avoid thermal transients arising from joule heating in the anchored wiring, specimen contacts or the specimen itself, the current source on the Fluke was never turned off, to ensure heat inputs were constant.

In the absence of doping, the measurements of the control specimen proved to be very difficult, due to low signal levels and high noise floor. Signal levels can be raised, by increasing the distance between the two voltage contacts, but with the average specimen size being 13 mm x 2 mm x 1 mm, the largest feasible distance was just 4 mm. Another option would be the use of a lock-in amplifier, but unfortunately the laboratory did not have one. A software implementation of a lock-in amplifier was possible through the use of the IOTech DaqBook 2000 data acquisition card, but again this was unsuitable due to the limited measurement range. It should be emphasised that the Fluke is a multimeter for calibration, and not designed for logging of data, and featured no output options besides the display, so values were recorded by hand.

Within the multimeter, data samples were taken under auto-reversing DC current conditions, and averaged for 1 minute before being the result was output to the display. From the display, 8 readings were manually taken, sorted, and input to a weighted average filter to give one data point for a specific temperature. The choice of auto-reversing current enabled the cancellation of thermoelectric potentials from dissimilar metal joins along the course of the wiring to the specimen. All wiring inside the cryostat was done with phosphor-bronze twisted pair leads, and externally connections were made with copper shielded twisted pairs, with the screens appropriately connected to the guard terminal to minimise the effect of electromagnetic interference on the measurement. Through this procedure, specimen resistivity was measured at a current of 10 mA, from room temperature down to 16 K.

Due to the difficulties encountered in measuring the low resistance – which was initially perceived to be one of the simplest measurements – the laboratory is looking to acquire the Keithley 6221 precision AC current source and the Keithley 2182 nanovoltmeter. The two units operate together in a ‘delta mode’, which reduces noise considerably, which was one of the problems encountered. In addition, although the measurement current can be varied to reduce joule heating, it is the ‘pulse delta’ mode that is desirable; the duty cycle of the current pulse can be decreased substantially, which results in decreased heating for testing of heat-sensitive devices, and perfect for superconductors.

4.6. Critical current testing

Determining the critical current density with the resistive testing apparatus was not possible directly, as the Fluke multimeter could only output currents of 10 mA and 100 mA at the required resolution. Instead an external variable current source was used, and the Fluke was set to measure DC voltage. The current source used was a Lake Shore Model 120, and was remotely programmed using a potentiometer to allow for variable current in range of 100 µA to 100 mA. The experimental setup is shown in Figure 4-23.

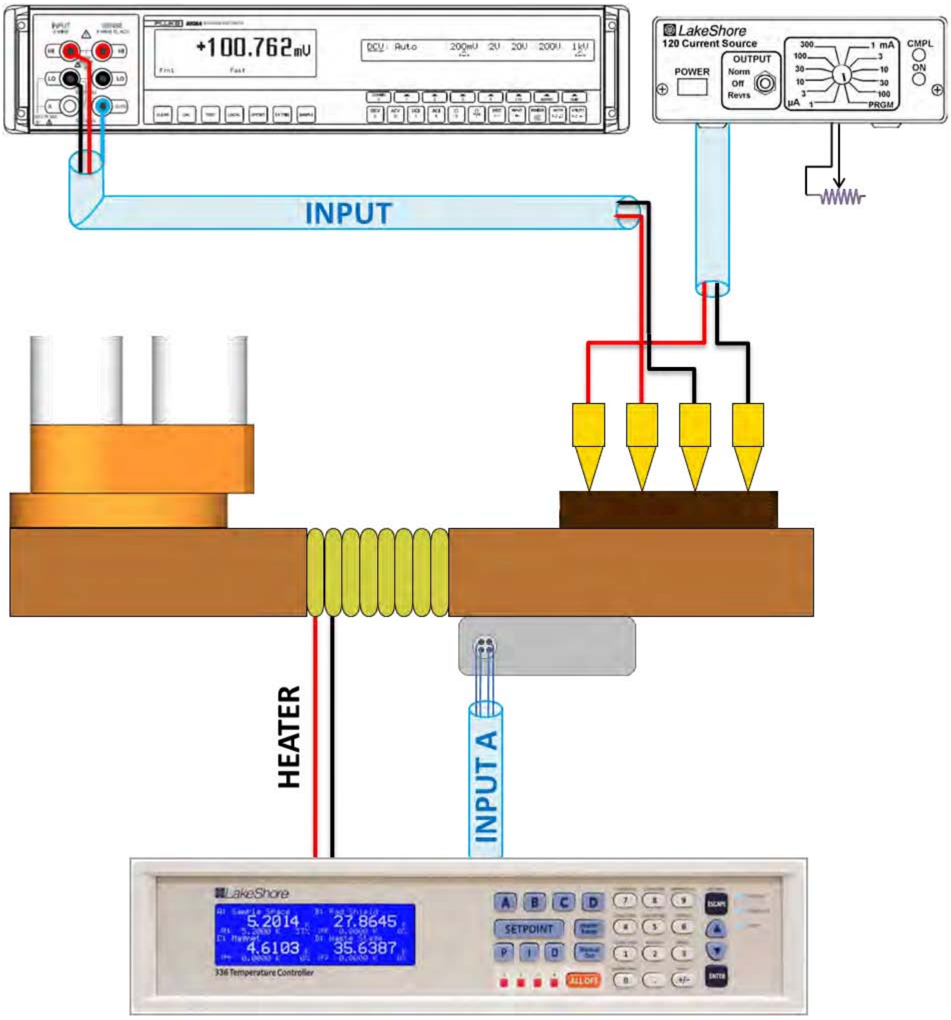

Figure 4-23 Apparatus used for critical current testing: current is sourced from the programmable Lake Shore model 120 current source.

In this configuration, however, the thermoelectric potentials from the joins between specimen, contacts, and wires could not be cancelled effectively, and the voltage developed across the specimen was simply lost in the noise floor. Thermoelectric potentials could be partially cancelled by reversing the current source polarity, but there was still too much noise, and due to the large time constants during measurement, reliable data could not be obtained.

4.7. AC susceptibility

To determine the critical temperature, T_c, of the specimens more accurately, it was necessary to avoid T_c suppression from the high transport currents that were used in resistive testing, so a low-field AC susceptibility approach was taken.

Measurement of the AC susceptibility is performed by immersing the specimen in an alternating magnetic field, generated by a primary solenoid. The change in response of the specimen is measured by a secondary coil assembly, consisting of two identical coils: one coil positioned over the specimen, whilst the other coil is used as a balancing coil. The balancing coil is used to negate the background field response, so that the only output from the secondary coil arrangement is due to the response of the specimen. The primary coil and secondary coil voltages are input to a lock-in amplifier, which is used to provide the quadrature and in-phase (real and imaginary) components of the complex susceptibility, as shown in Figure 4-24

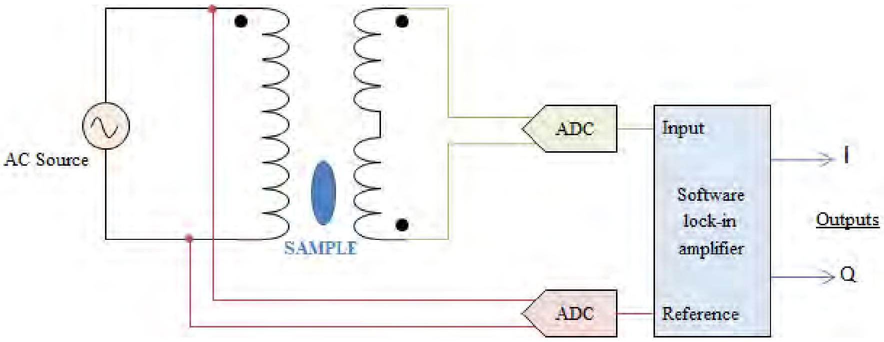

Figure 4-24 AC Susceptometer. The voltage applied to the primary coil, and the output from secondary coil are input to analogue-to-digital converters (ADCs), and input to a lock-in amplifier. The real and imaginary components of the complex susceptibility may be determined easily from the in-phase (I) and quadrature (Q) outputs of the lock-in amplifier.

Before the specimen is cooled down, the quadrature output of the lock-in amplifier is zeroed by a phase adjustment of the reference signal. As the phase difference between the input signal and the reference signal reaches zero, the multiplication of these two results in only a real component, thus the quadrature output is zero. Zeroing the output at room temperature is done so that any change in the quadrature component is due to temperature-dependent effects in the specimen.

At low primary fields, the screening currents established by the specimen will be small, and should not have any suppressive effect on the transition temperature. In the normal state, the specimen should have a finite susceptibility that is likely to be near zero, but abruptly changes to -1 as the transition temperature is reached. The low applied field must be much less than the critical field to allow the superconducting bulk to approach perfect diamagnetic shielding.

χ' is the real component of the susceptibility, and is associated with the dispersive magnetic response, whilst χ'' is the imaginary component, which is associated with absorptive or irreversibility response arising due to energy dissipation within the specimen. There are three main mechanisms for losses in the AC magnetic field: flux flow losses, hysteretic losses near the pinning centres, and surface pinning losses. The χ'' curves can thus exhibit both inter and intra granular peaks, dependent on the loss mechanisms present.

The bulk specimens previously cut to typical dimensions of 1 mm x 2 mm x 4 mm were mounted in a purpose-built AC susceptibility sample stage. The stage consists of a solid copper bar, with a machined groove for a nichrome heater, and mounting options for a calibrated PT100 thermometer and a copper cold finger onto which specimens were mounted. The coil assembly was built with the assistance of a student helping in the lab, designed to operate in the range of 0.1-100 kHz.

A function generator outputs an AC voltage to the primary coil, which establishes an AC magnetic field within the coil. The voltage applied to the primary is also input to a differential channel on the IOTech DaqBook 2001, and used for referencing in the lock in amplifier. The waveform is a sine wave, with a voltage of 142.77 mV RMS at a frequency of 1099.1 Hz. The signals from the series-opposition wound secondary coils are sent to another differential channel on the DaqBook. An electrical block diagram is shown below in Figure 4-25.

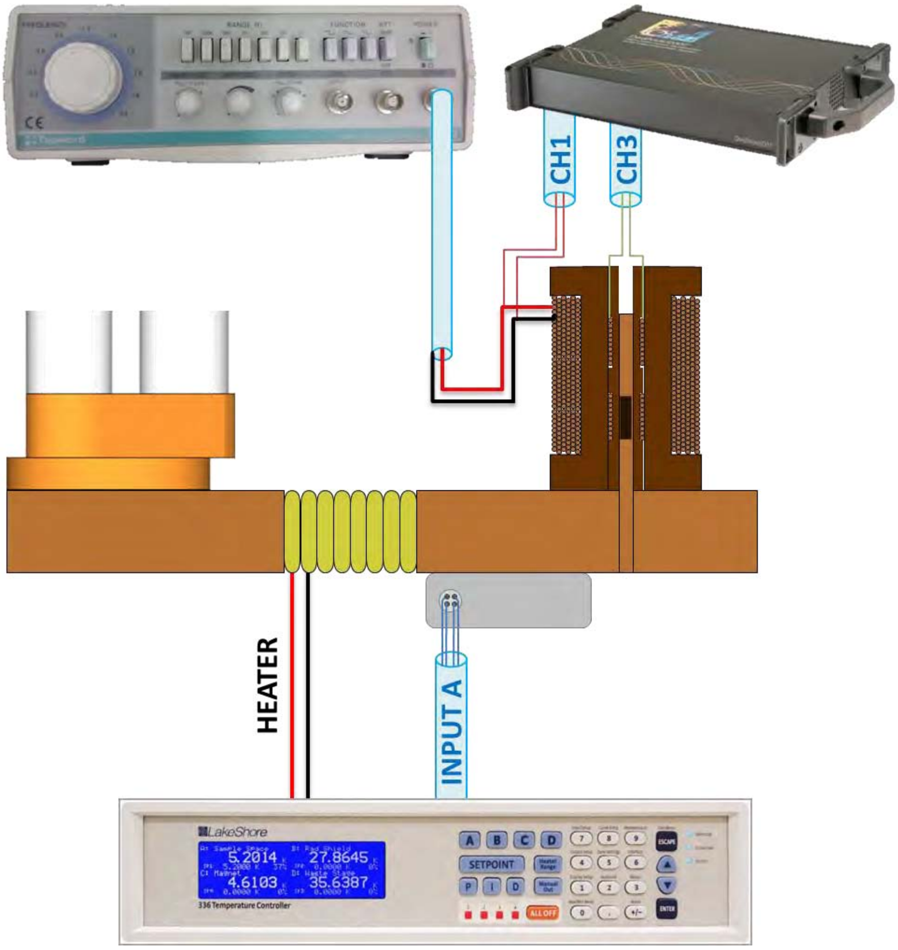

Figure 4-25 Apparatus used for AC susceptibility investigations: a function generator drives the AC magnetic field, whilst the DaqBook provides logging of the primary and secondary coil data over Ethernet.

A software based lock-in amplifier was designed and built in DASY Lab, offering design flexibility for different frequencies, as well as options for data processing, if required. The block diagram is shown below in Figure 4-26, and the DASY Lab interpretation is detailed in Appendix A.

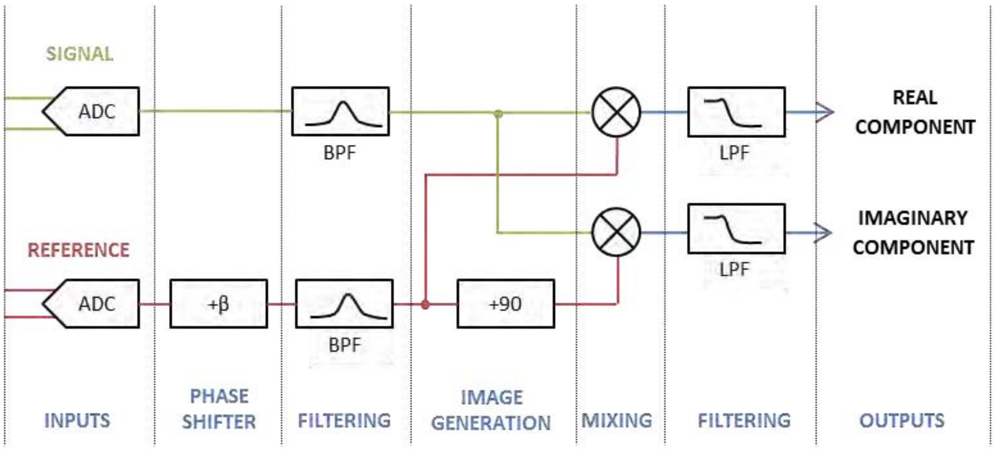

Figure 4-26 Block diagram of the lock-in amplifier implemented in DASY Lab.

Room temperature phase adjustment was performed manually from within DASY Lab, by observing graphs of the primary and secondary signals, where the required phase offset could easily be determined by measuring the difference between zero-crossings. Phases were adjusted as best possible, but limited by the 25 kHz sampling rate of the DaqBook. This meant that the minimum delay intervals were 40 µs, so phase alignment could be within +-20 µs of the input signal. This misalignment corresponded to a maximum phase imbalance of

$$\Delta\beta = \pm\frac{f}{2f_s} * 360° = \pm\frac{1099.1}{(2 * 25000)} * 360° = \pm 7.91°. \tag{4.1}$$

Data reduction was achieved by extracting 1 measurement from the output data stream every 2 seconds, and was written directly to hard disk from within the software.

The heater output was configured to a 5 W limit from within the Lake Shore 336 temperature controller, in order to obtain a linear temperature ramp of 1 K.min^{-1} from room temperature down to 16 K. All specimens were subjected to the same testing procedure, and errors due to thermal lag between thermometry and the specimen were accounted for by performing a control specimen test with at a ramp of 80 mK.min^{-1}. Temperature measurement and ramp settings were performed using custom PC software written to interface with the temperature controller over Ethernet connection, as detailed in Appendix B.

Chapter 5 Results and Discussion

In an attempt to alter the normal resistivity of MgB_2, carbon doping by CVD was performed. To gauge the success of doping it was necessary to perform resistivity measurements, and measure the corresponding change in critical temperature. Such an approach would give an overview of possibly resistivity increases versus the critical temperature margin that would be sacrificed for operation at a given temperature. Specimen morphology was also investigated, to provide insight into the doping mechanism and the effect on the parameters. Specimens with doping concentrations of 0, 4, 8, 12, 16% were investigated, noting that due to the crucible failure during heat treatment, the 21% specimen was not tested.

5.1. Specimen morphology

Specimen morphology was investigated via two techniques, scanning electron microscopy and optical microscopy. The primary advantage of scanning electron microscopy over optical microscopy is the far superior resolutions that can be attained, whilst simultaneously providing a much greater depth of field. Optical microscopy presents the advantage of using visible light and can hence show the specimen in natural colour. With the use of polarised lenses, the optical micrographs can present the various reflective and refractive properties of the specimen. In particular, using polarised light, the optical microscope can identify structures or grains that reflect back the light at different polarisations.

5.1.1. Scanning electron microscopy

Scanning electron microscopy (SEM) was used to investigate the specimen topology at low (600 ×) magnifications, in particular looking to determine the homogeneity of the specimen on a macroscopic scale; looking for large unreacted areas or pores. Investigations into the particle size were also performed. The SEM used was a Carl Zeiss Ultra Plus, which has a resolution of 0.8 nm, but magnification beyond 120 000 × was not necessary.

Typical trend in a fracture face

SEM analysis was performed on an undoped specimen, which broke during sectioning for resistivity measurements. The exposed fracture face was micrographed at different magnification levels, as shown in Figure 5-1.

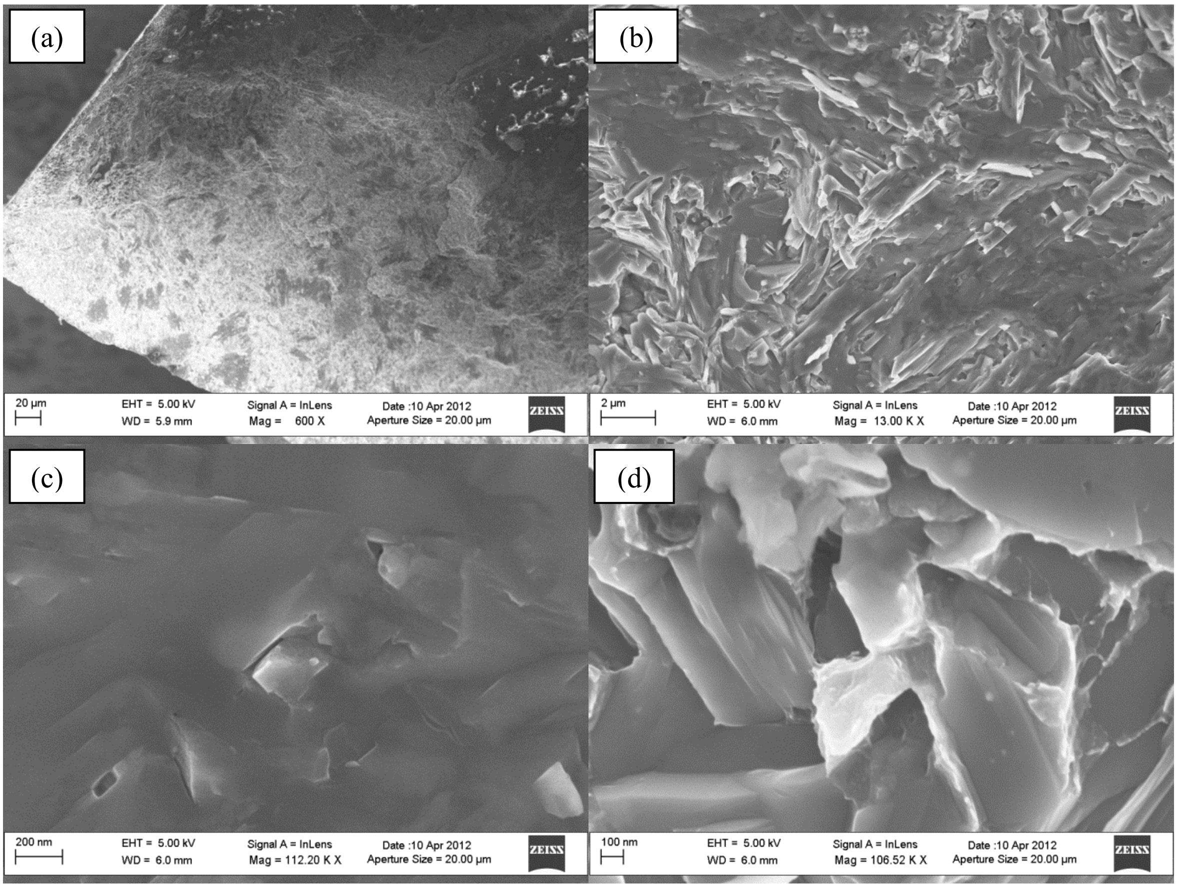

Figure 5-1 Typical scanning electron micrographs of an undoped specimen along a fracture face at magnifications of (a) 600 × and (b) 13 000 ×, and highlighting (c) intragranular fracture at 11 220 ×, and (d) intergranular fracture at 106 520 ×.

Here, intragranular and intergranular fractures can be observed in Figure 5-1(c) and Figure 5-1(d) respectively. There were no visible differences between doped and undoped specimens.

Comparison of high magnification cut specimens

The specimens analysed by SEM were the same specimens used in the resistive tests, and as such, were sectioned on all sides of the specimen. As the diamond blade used in sectioning cuts by abrasion, there is a tendency for platelets to be cleaved from the bulk along the grain boundaries. Thus the surface presented thus shows some intragranular views as well as some intergranular interfaces, the grain boundaries. As the specimens presented little difference at lower (600 ×, 13

000 ×) magnifications, only the high (~100 000 ×) magnification images are shown for the 0-16% doped specimens, in Figure 5-2.

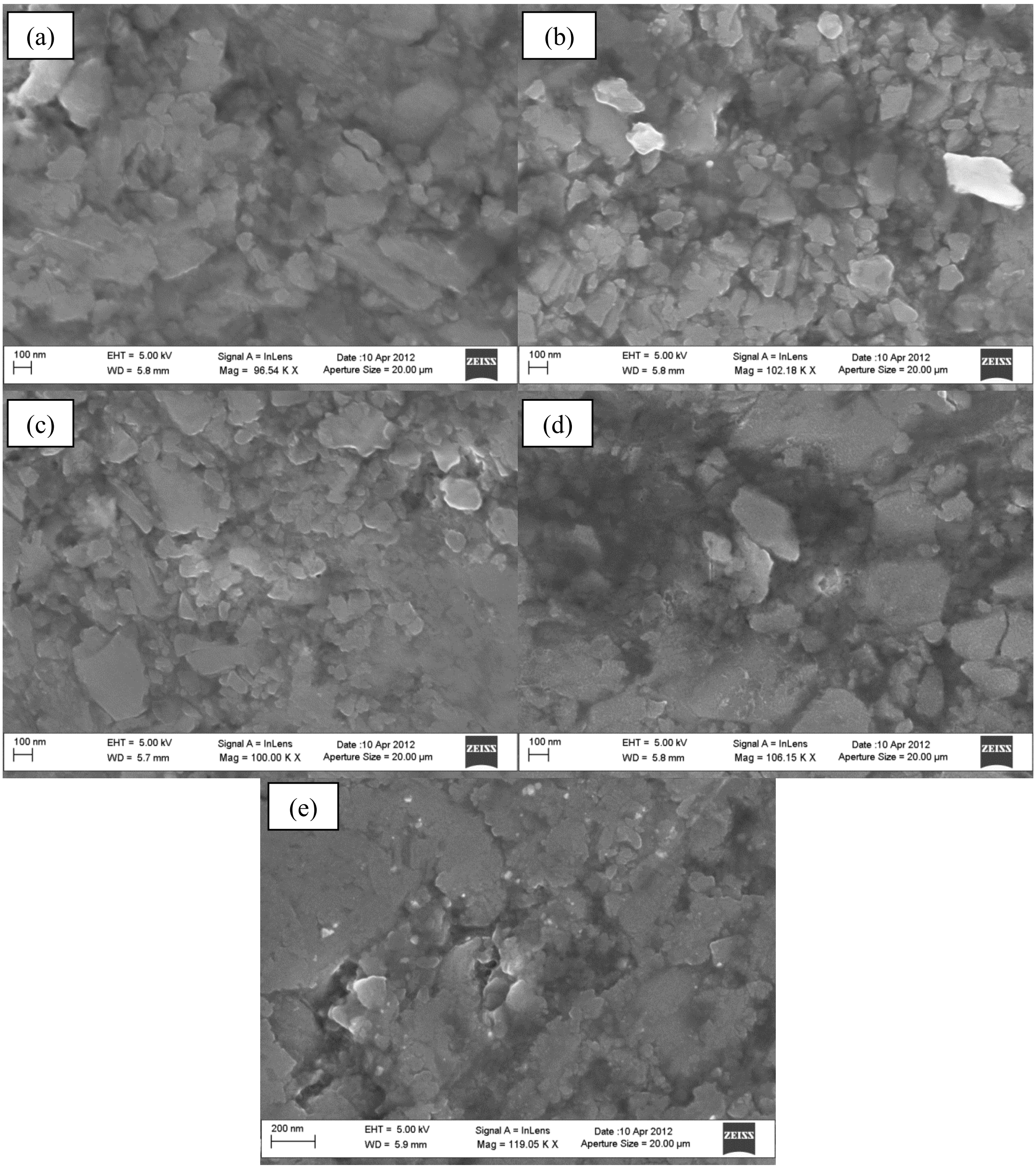

Figure 5-2 High magnification micrographs of specimens doped from 0% (a) to 16% (e). There appears to be little evidence of doping in the micrographs, the only differences stem from the different amounts of platelets removed during sectioning.

The size of grains is difficult to determine due to the wide size distribution of grains, and large number of intragranular slices. Of the smaller grains that are revealed, they appear to be about 100 nm in diameter throughout all the micrographs, thus doping did not appear to affect the grain size.

5.1.2. Optical microscopy

As with the case of the scanning electron micrographs, doping did not seem to introduce any effects observable with optical microscopy, which is not particularly surprising due to the vastly inferior resolution of optical microscopy compared to SEM. The normal and cross-polarised views of a typical specimen are shown in Figure 5-3.

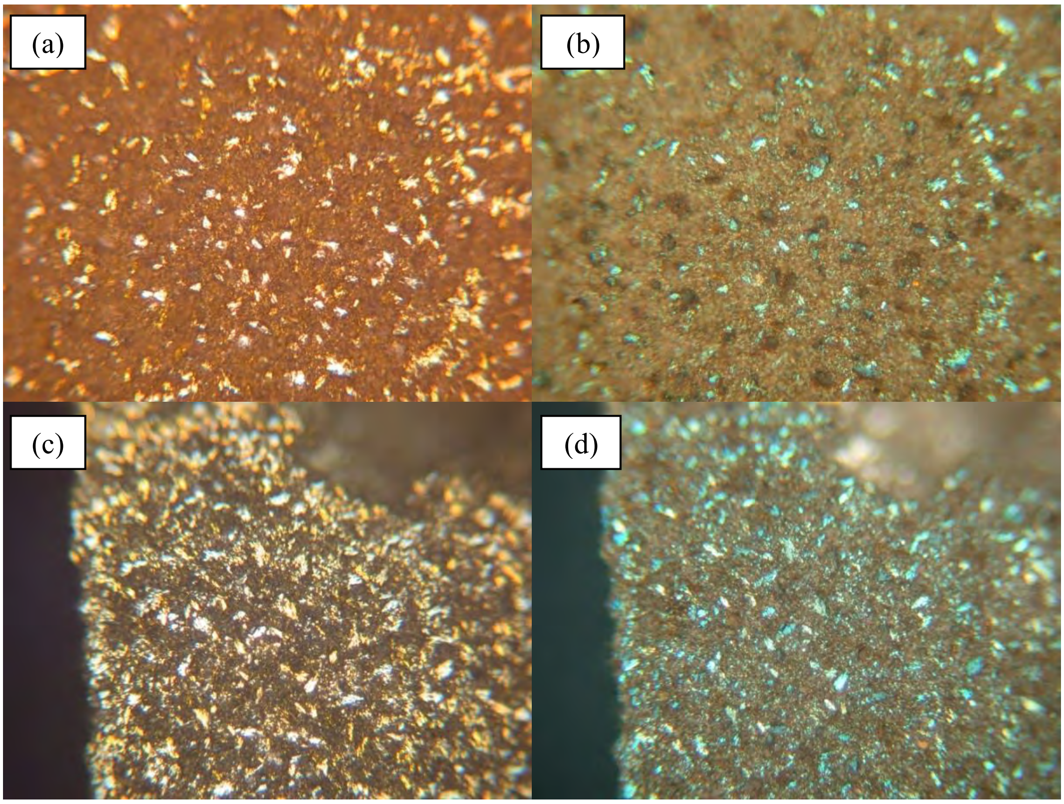

Figure 5-3 Optical micrographs of the 4% doped specimen. Micrographs are taken in normal light (a),(c), and cross polarised (b),(d).

The micrographs reveal that the specimen has a bimodal grain distribution, as there are high numbers of small and large grains, but few grains between these sizes. The specimens appear to have a high density, as there no observable voids, and the similarities between the two micrographs taken at very different sites implies that the specimen has good homogeneity. Darker spots under normal light could be voids, but investigating the same sites under cross-polarised light reveals that these sites simply have grains in different crystallographic orientations.

Identification of voids

An example of a void is shown in Figure 5-4, where there is a dark spot in both the normal light and cross-polarised micrographs.

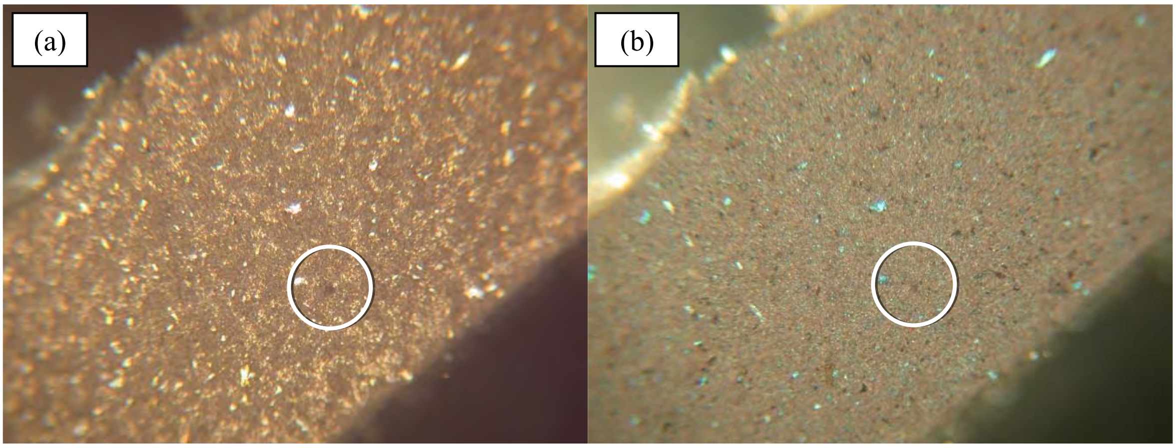

Figure 5-4 Void identification using optical micrographs. Dark spots on both the normal light and cross-polarised micrographs indicate a void, for example the circled spot.

Voids were not initially found with the specimen under the microscope, but only later during analysis of the images. Of the numerous images taken, very seldom were voids observable.

Excess magnesium phase

When sectioning specimens from the bulk pellet obtained from the RLI fabrication process, the face of the pellet that was in contact with the magnesium bulk had poor homogeneity (determined visually), so a 1-2 mm section was removed before sectioning a specimen. One of these discarded pieces was investigated with optical microscopy, as shown in Figure 5-5.

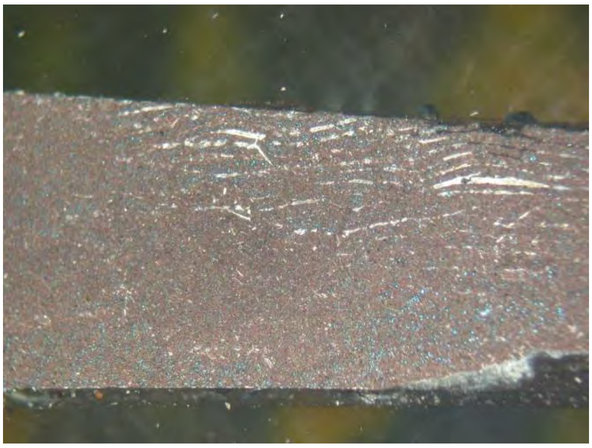

Figure 5-5 Excess Mg layers near the reaction interface. The reaction interface would be at the top of the figure, and the layers appear to bend towards the interface.

The uniform colour of the layers near the top indicates a metallic nature, and hence is excess magnesium filling the space between some MgB_2 layers. The layers seem to bend towards the interface, likely due to the fact that the other faces of the boron preform are contact with the crucible walls, and thus the small expansion of the final product with respect to the boron preform is directed towards the interface.

5.2. Normal resistance measurements

From the resistivity experiments outlined in Section 4.5 the following results were obtained. Unfortunately, the 16% doped specimen suffered some fractures during removal from the crucible which reduced the maximum cut specimen length to ~10 mm, which was too small to be tested with the pogo pin apparatus. In addition, due to the leak during heat treatment of the 21% specimen, no specimen was available to test at this doping concentration. Thus the results presented here are for doping concentrations of 0-12% carbon.

As expected, the doping concentration played a significant role in increasing the resistivity of specimens, with increases in doping concentration resulting in increases in resistivity. The following graphs show the particular trends that were observed whilst measuring the resistance of the doped specimens. A plot of the resistivities is shown on a linear scale in Figure 5-6.

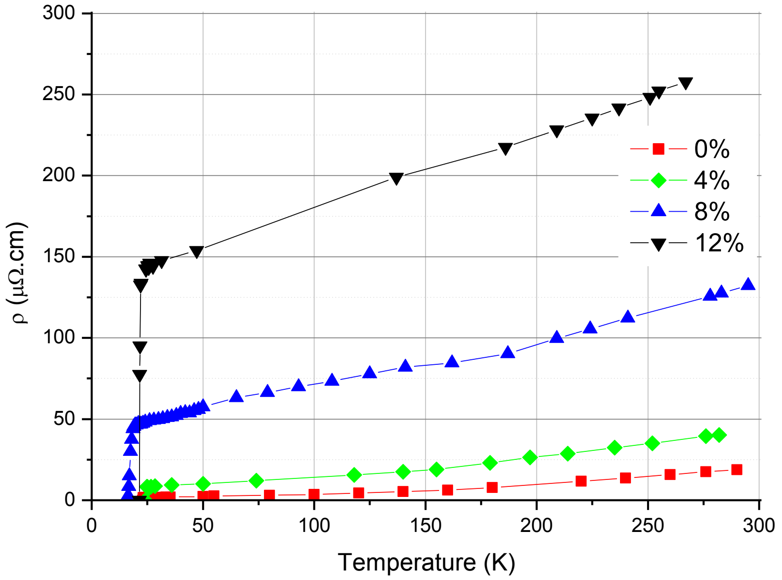

Figure 5-6 Resistivities of doped specimens as a function of temperature. A clear temperature dependence is observed for all specimens, with normal-superconducting transitions observable at low temperatures.

There is dependency of the resistivity on the doping concentration, as the specimen doped to 12% had a room temperature resistivity, ρ_{295}, a factor of 14.24 times larger than the undoped specimen. It is also interesting to interpret these plots on a logarithmic scale as shown in Figure 5-7.

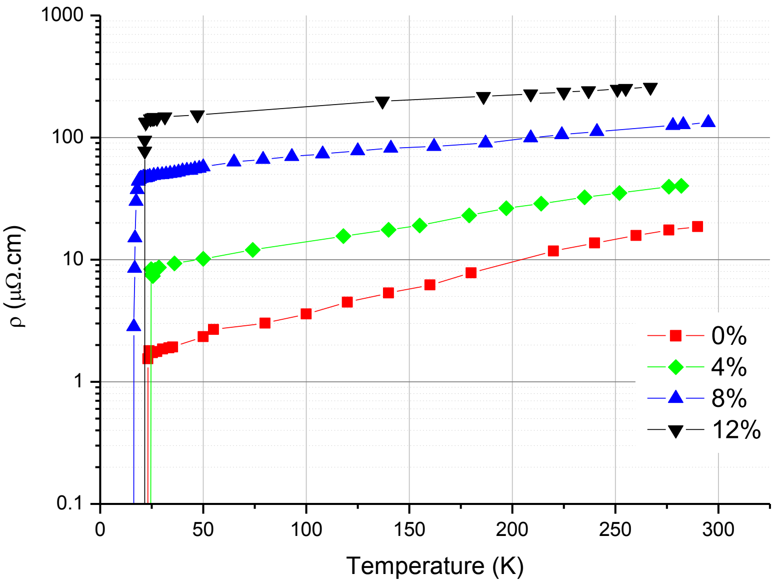

Figure 5-7 Resistivities of doped specimens as a function of temperature, plotted on a logarithmic scale. The increase in doping concentration appears to give a roughly logarithmic reisistivity increase.

Here, for equal increments in doping concentration there appears to be a fairly logarithmic increase in resistivity. It is also interesting to note that the magnitude of the difference between the 12% and undoped curves is large at low temperatures, which is advantageous, as the initial current limiting is obviously at low temperatures. By maximising the resistivity at low temperatures, enhance limiting characteristics can be achieved.

Looking at the transition region, there does not seem to be correlation between doping concentration and the observed critical temperature, T_c, which was defined in three different ways:

1. Quantitatively defined as the data point prior to evidence of the superconducting state appeared. This approach was performed by visual inspection, and suitable due to the narrow transition width of the specimens.
2. Qualitatively defined as the first data point where the derivative of the resistivity exceeds all other normal state values. The normal state derivative values are fairly consistent, thus an upper and lower limit to accepted normal state values could easily be determined by looking at the data from room temperature down to, say, 40 K. The first data point to exceed these bound defined T_c.
3. Qualitatively defined similarly to method number 2, except taking the data point prior to this. This was done due to the fact that in method number 2 the specimen is already superconducting at that data point, so the material should be in the normal state for the data point prior to this. Uncertainty for this method arises from the fact that the data points do not have regular temperature intervals, and the previous data point may be, perhaps, 2 K above the point defined by method 2.

The construction required for method 2 is shown for the 4% in Figure 5-8.

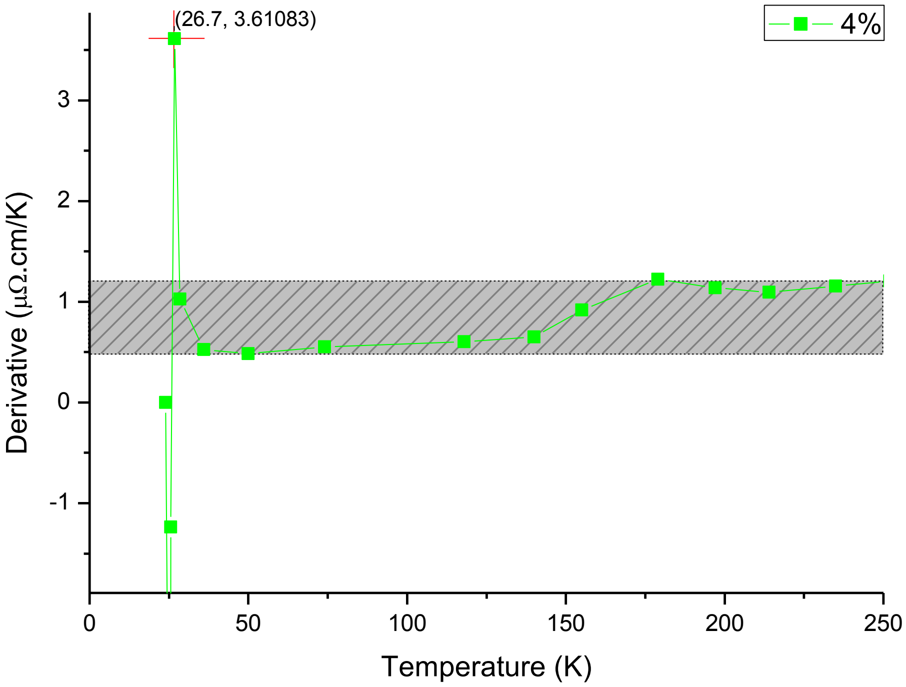

Figure 5-8 Resistivity derivative graph with construction added for determining T_c via method number 2. The box was drawn around typical normal state values, and the first data point to exceed this defines T_c, Method number 3 simply takes the data point prior to this to define T_c.

The T_c's obtained by the 3 different methods are listed in Table 5-1, and plotted in Figure 5-9.

Table 5-1 Critical temperatures obtained by the three methods. The onset of superconductivity lies somewhere between the values obtained by method 2 and method 3.

Sample	Method 1 T_c (K)	Method 2 T_c (K)	Method 3 T_c (K)
0%	23.1	23.7	25.4
4%	24.8	26.7	28.5
8%	20.0	19.5	20.0
12%	21.6	22.0	22.3

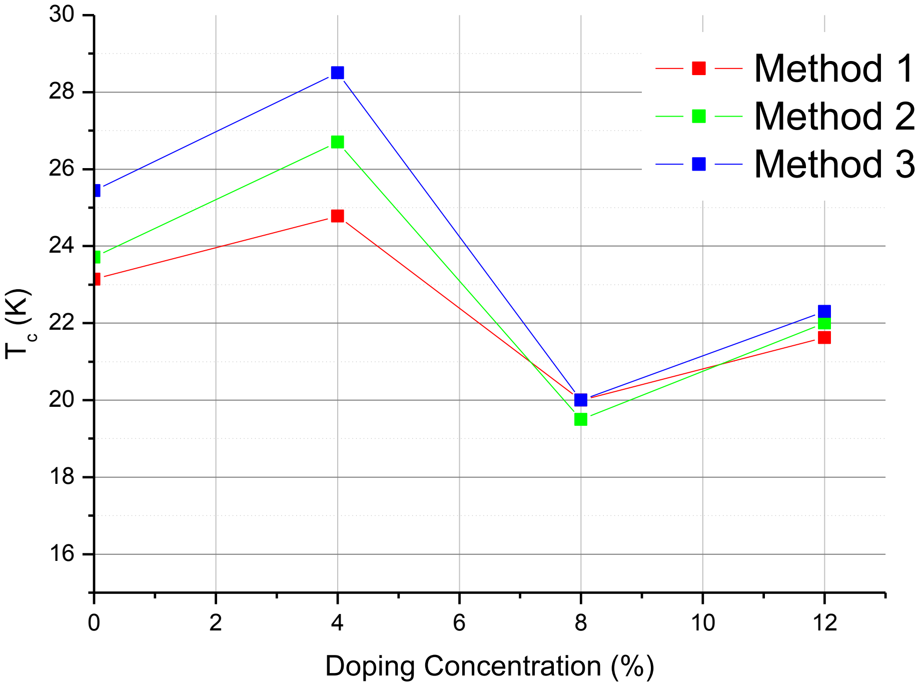

Figure 5-9 Critical temperatures determined by the three methods for the doped specimens. Despite the differences in calculation method, a similar non-correlated trend is observed.

The choice of method in defining T_c did not alter the observed non-correlation, and hence the lack of correlation was not a product of data analysis, but instead from the measurement technique.

As mentioned in Section 4.5, the measurements were made at a nominal current of 10 mA, which evidently had a suppressive effect on the critical temperature, as the control specimen was expected to have a T_c between 35 K and 39 K. The overall suppression can easily be attributed to the high measurement current, but unfortunately the current does not explain the lack of correlation between the transition temperature versus the doping concentration. According to the theory presented in Section 3.4, increased disorder should decrease T_c, and hence the expected trend was for 12% to have the lowest T_c. Therefore based on the theory, the experimental observations are likely to be inaccurate either in the resistivity measurements or the temperature measurements. Due to the measurement technique and the subsequent data processing performed on the resistivity data as outlined in Section 4.5, the data recorded from the Fluke calibration multimeter is considered to be valid, and therefore implies that the temperature data is the source of error.

The discrepancy in temperature data is likely due to joule heating, although not in the specimen itself (due to the low resistivity), but at the specimen contacts. As contact was made by the pogo pins directly and without surface treatment of the sectioned specimen, the contact resistance could have a significant variation both between specimens and experimental runs. Repeatability of specimen resistivity measurement was still maintained due to the four-wire resistance measurement technique implemented. It should be mentioned again, that the resistivity of MgB2 is incredibly low, with clean samples having resistivities that are of the same order as metals such as tungsten, zinc, and platinum. Thus measurement was difficult, and for a bulk sample sectioned to the appropriate dimensions, the measurement is not dissimilar from that of a piece of metal.

The fine points on the pogo pins were suitable for voltage contacts, but due to the small contact area presented, not ideal for current contacts. Current contacts should have a large surface area to ensure that for a given contact resistivity, the contact resistance is minimised. Despite these obvious downfalls, the pogo pins used were the only contact method to achieve any repeatable results. The small contact area is believed to have introduced significant joule heating, which should have remained constant throughout the experiment, as the measurement current was never interrupted to avoid introducing thermal transients. The heat input from the contacts is thus likely to have introduced a thermal gradient, dependent on the specimen contact resistance. So although the thermometry was placed as close to the specimen as possible, it did not necessarily reflect the true temperature of the specimen.

Thus the T_c data obtained were not used at all, and the only information read from the abrupt change in resistivity was that a phase transition occurred, and thus all specimens superconduct at some temperature.

The analysis of data based on the changes in resistivity are still valid despite temperature inaccuracies, as calculations are based on the absolutes values and do not introduce temperature. The contributions of the phonon and residual resistivities to the overall resistivity over the temperature range versus doping concentration are shown in Figure 5-10.

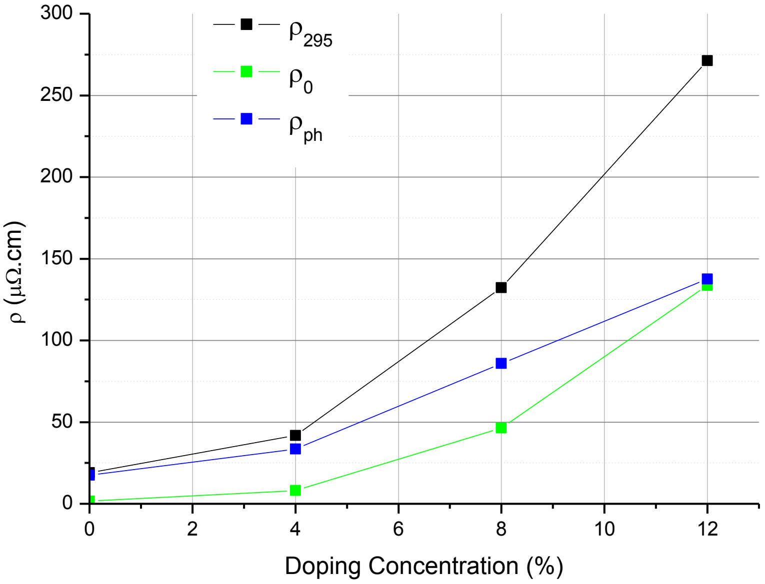

Figure 5-10 Room temperature, residual, and phonon-contributed resistivities for doped specimens. The doping concentration does not appear to affect the residual and phonon-contributed resistivities identically.

This gives better insight into the contours of the plot contours of the resistivity plots, where the undoped specimen visually appears to follow a power law, whilst the 12% doped specimen display a much more linear trend. This results due to the decrease in phonon contribution, hence there is less temperature dependence. It can be seen that as the doping concentration increases, the phonon contributes more absolute resistivity but less relative contribution to the overall resistivity, as highlighted in the stacked bar graph of Figure 5-11.

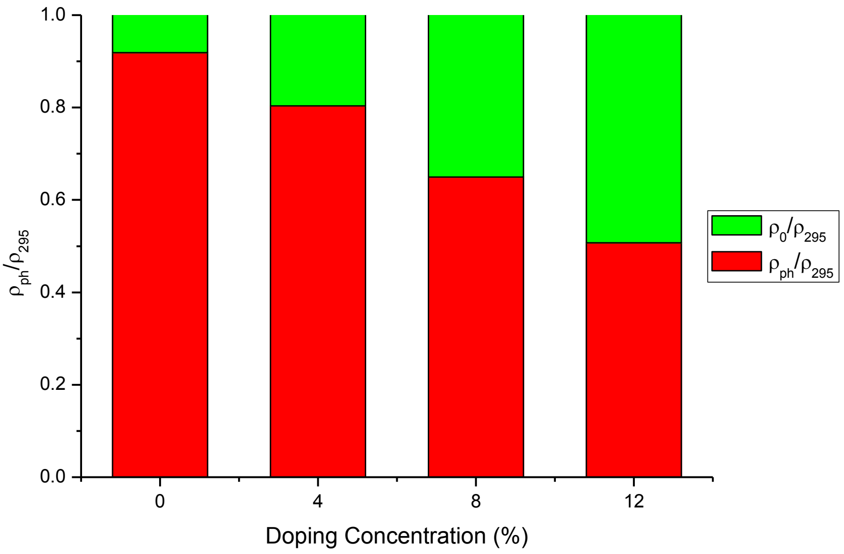

Figure 5-11 Relative contribution of the residual and phonon-contributed resistivity. At a doping level of 12%, the phonon-contributed resistivity is almost equal to the residual resistivity.

From this we can deduce that doping increases the residual resistivity more than the phonon contributed resistivity.

As discussed in Section 3.3.2, the resistivity of MgB_2 varies between specimens. Mazin *et al* noted that the resistivity was found to vary greatly with differing degrees of correlation to T_c [**73**]. The phonon contribution, ρ_{ph} is a measure of the connectivity of the superconducting grains, with reviews suggesting perfect connectivity has a phonon contribution that is around 7-9 $\mu\Omega.\mathrm{cm}^{-1}$ [**198**]. The undoped specimen had a phonon contribution of 17.5 $\mu\Omega.\mathrm{cm}^{-1}$ which, relatively speaking, is not too far off from ideal but also supports the explanation of low T_c's encountered in the following section.

5.3. AC susceptibility

As it was not possible to decrease the measurement current used in the resistivity measurements, it was necessary to make use of AC susceptibility (ACS) measurements to determine the transition point more accurately. As outlined in Section 4.7, measurements were obtained for specimens with various doping concentrations, and these results are presented and discussed below.

The results obtained were all very similar for the majority over the temperature range, so data for the undoped specimen is presented first as a general case. The real component of the complex susceptibility for the undoped specimen is shown in Figure 5-12, where 'Q', the quadrature output from the lock-in amplifier, represents χ'.

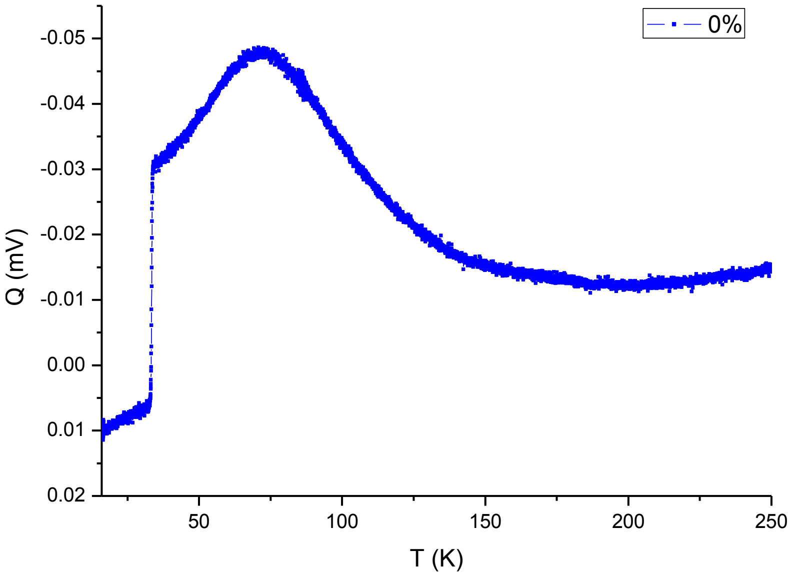

Figure 5-12 Real component of the complex susceptibility for the undoped specimen (0%). A transition is clearly visibly between 25 K and 50 K.

The corresponding imaginary component of the complex susceptibility for the undoped specimen is shown in Figure 5-13, where here 'I', the in-phase output from the lock-in amplifier, represents χ''.

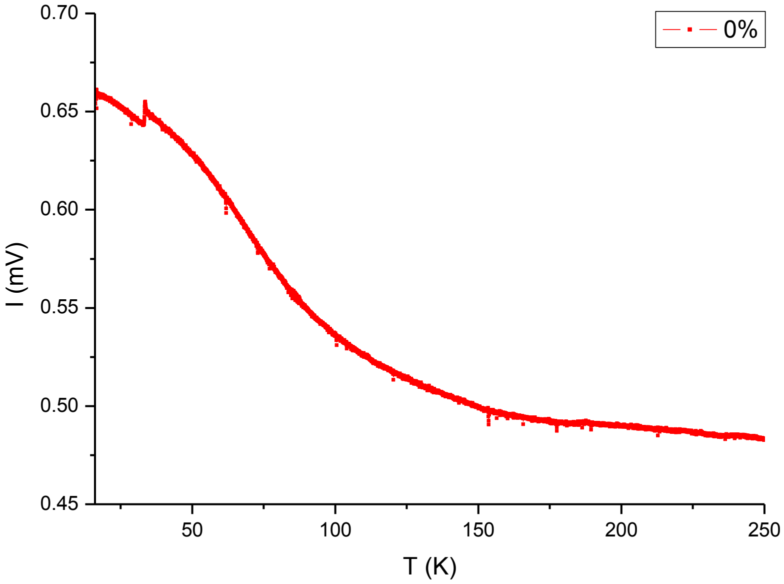

Figure 5-13 Imaginary component of the complex susceptibility for the undoped specimen (0%). The transition can still be identified by the abrupt step somewhere between 25 K and 50 K, but here it is less pronounced than the transition identified from the real component.

From these graphs we can clearly see that there is an abrupt change in susceptibility at low temperatures, indicative of the normal-superconducting phase transition, but the simple response expected seems to be superimposed on a fairly large contour. Investigations revealed that this was due to insufficient balancing: the signal from the secondary was a summation of the specimen response as well as some contributions from the copper cold finger used to cool the specimen. To eliminate this, a reference curve was recorded by performing a 'dry' run; an experiment with no specimen present. The data recorded was thus the imbalance response of the copper cold finger used in the sample mount, the real component of which is shown in Figure 5-14.

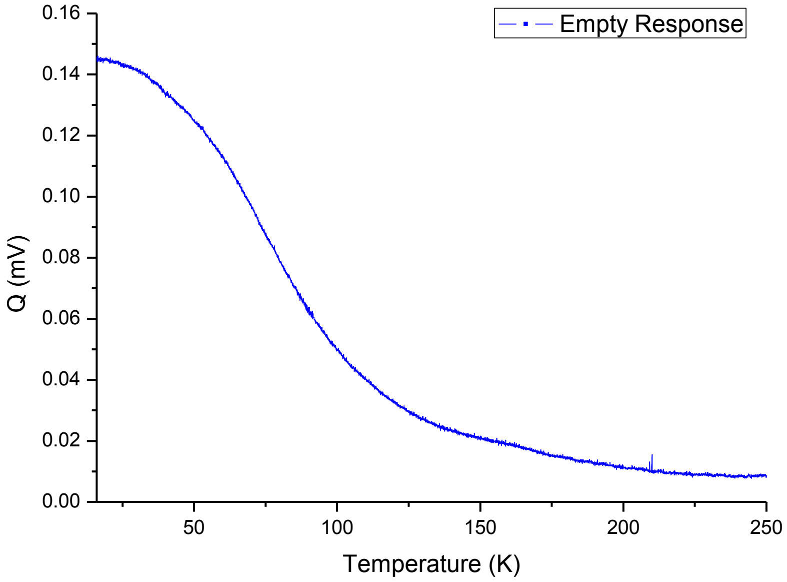

Figure 5-14 Real component of the complex susceptibility reference curve. This response is due to the copper cold finger being insufficiently cancelled by the secondary coils.

After subtraction of the reference data, the real component of the undoped specimen is shown in Figure 5-15, where the data has also been normalised at the transition point.

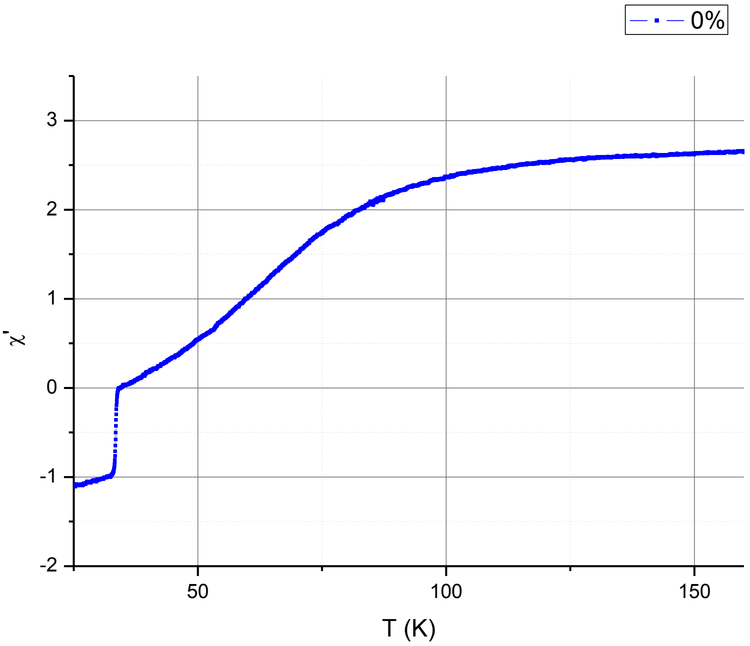

Figure 5-15 Real component of the complex susceptibility for the undoped specimen (0%) after subtraction of the reference curve. The data has been normalised between -1 and 0 around the transition temperature.

As the method of subtracting the reference curve is not perfect, there are still undesired effects present, yet this ultimately proves satisfactory because the derivative of the unwanted behaviour below 50 K is reasonably constant.

A collection of the real susceptibilities is shown in Figure 5-16, noting that a bulk piece of 16% doped specimen was large enough to use in these tests (light blue).

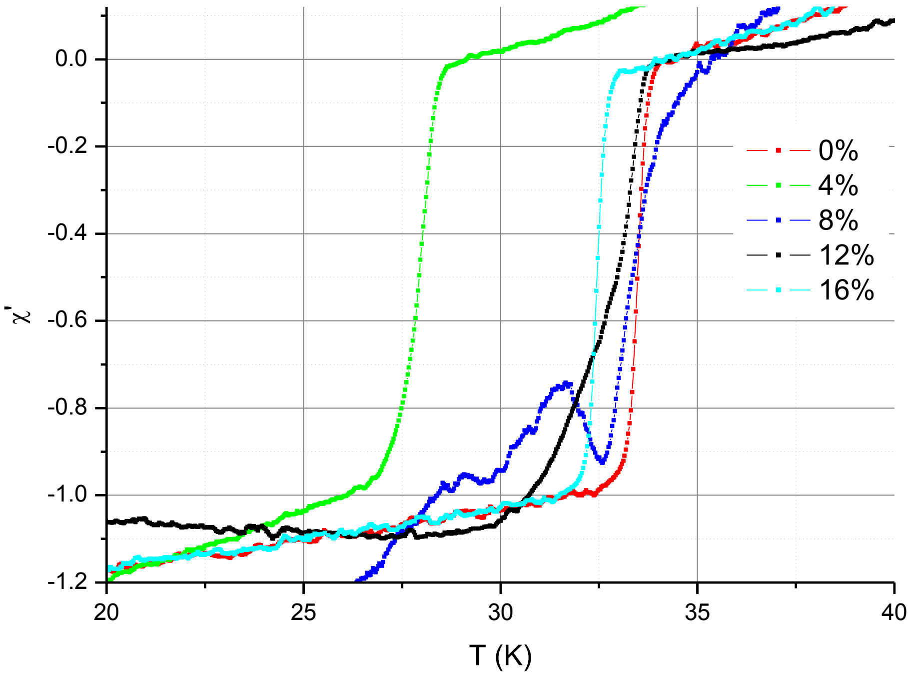

Figure 5-16 Real susceptibility of specimens doped in the range of 0% to 16%.

The derivatives were calculated and plotted to aid in determining the critical temperature. The transition temperature was defined by the first observable onset of superconductivity, specifically where the derivative graph $\frac{d\chi\prime}{dT}$ first exceeds the typical normal state bounds, as shown in Figure 5-17. Here, the normal state values are indicated by the constructed box, and the first data point to exceed these bounds is highlighted and annotated.

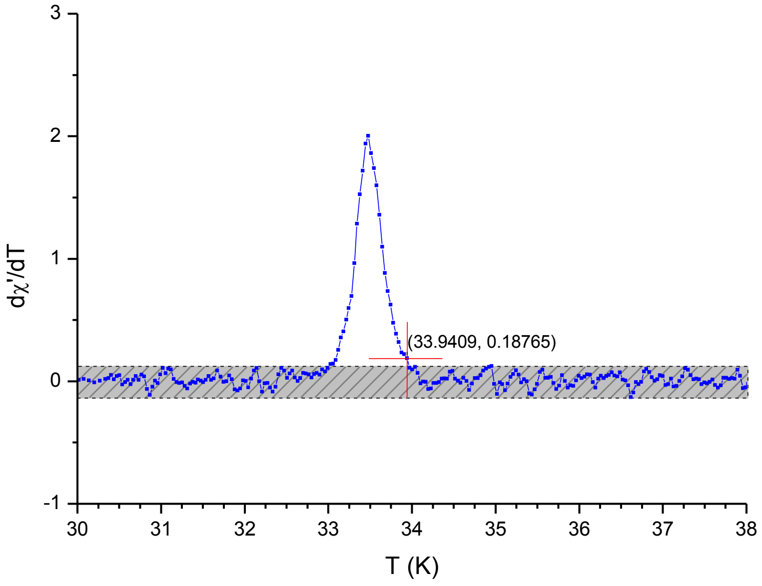

Figure 5-17 Derivative of the real component, showing construction required for determining the critical temperature. The critical temperature is defined as first data point that lies outside the typical normal state bounds, indicated by the cursor and the box construction respectively.

In the derivatives observed, there was only one peak identified, which implies that both the intergranular and intragranular transitions occurred at the same temperature; no weak links were introduced by doping.

All of the derivatives obtained are plotted with coloured drop lines at the critical temperatures in Figure 5-18.

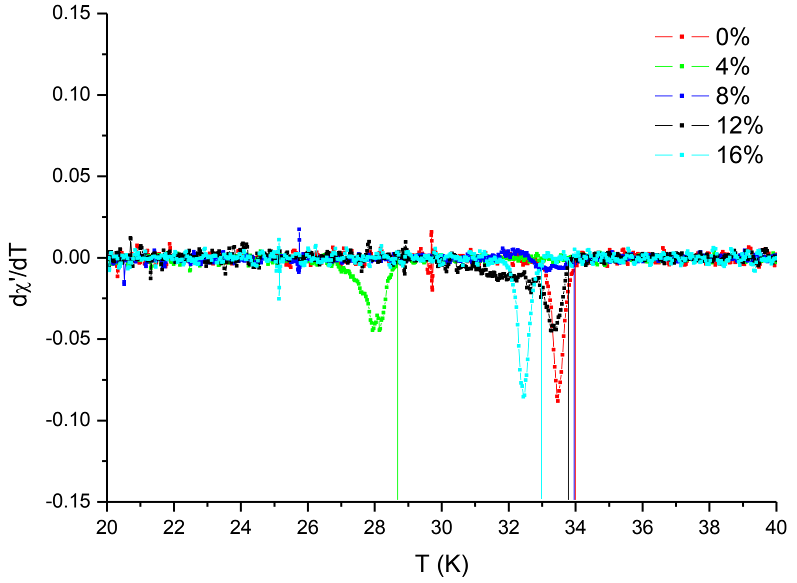

Figure 5-18 Derivatives of the real component, from specimens doped in the range of 0% to 16%. Coloured drop lines are added at the respective critical temperatures.

The critical temperatures obtained from AC susceptibility measurements are detailed in Table 5-2, and plotted in Figure 5-19.

Table 5-2 Critical temperatures obtained from analysis of the AC susceptibilities.

Sample	T_c (K)
0%	33.94
4%	28.62
8%	33.95
12%	33.76
16%	32.90

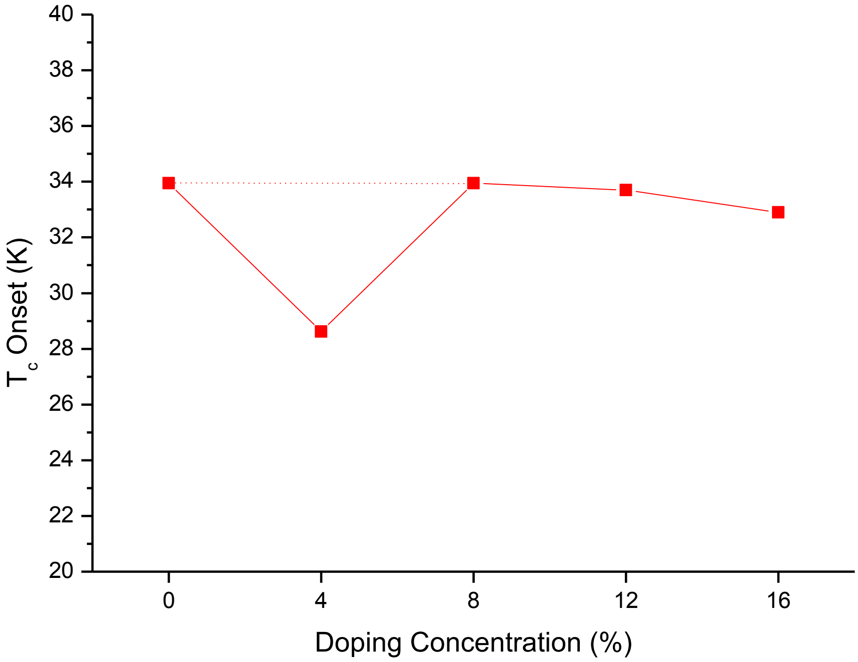

Figure 5-19 Graph of the critical temperature vs. doping concentration. With the exception of the data obtained from the 4% specimen, there appears to be very little change in critical temperature with a change in doping up to 16%.

Again, looking at all the results there does not appear to be a strong correlation between T_c and doping level. However, if the result from the 4% specimen is discarded, there degree of correlation increases substantially.

Recalling Section 0, where the heat treatment of crucibles was discussed, it was noted that a weld failure had occurred in the 21% crucible at the interface between the crucible and the 4% crucible that happened to be in physical contact. Though some of the other crucibles were also in physical contact with each other, none of them were in contact with the 4% or 21% crucibles. The MgO phase formation on the outside of the 21% crucible at the point of weld failure resulted in additional thermal conductivity to the 4% crucible. With a flame temperature of 3100 ºC, the burning magnesium in contact with the 4% crucible is likely to have introduced a significant heat flow, resulting in the heat treatment of that specimen being an undetermined amount higher that the desired peak reaction temperature of 900 ºC, for an undetermined period. Thus, although the product obtained from the 4% crucible *appeared* in-tact, it was affected by the weld failure of the 21% crucible, as clearly manifested in the critical temperature data obtained from AC susceptibility.

Neglecting then the 4% data point, the critical temperatures were accurately determined, and did not vary greatly as a function of doping. The decrease in critical temperature of the 16% doped specimen was just 1 K, which corresponds to a 3% decrease compared to the undoped specimen. Overall the critical temperatures were expected to be higher, but this is likely due an issue during fabrication, as the superconducting grain connectivity differed by a factor of 2 compared to perfect connectivity, identified by the resistivity measurements. This could be explained by the boron precursor form and purity, which as mentioned in Section 3.5, plays a part in determining the properties of the product obtained. The Sigma-Aldrich powder used in this research was only technical grade (95-97% purity), but was the only powder that could be sourced due to import restrictions.

In the topical review by Eisterer [**89**], an empirical fit of data from a number of specimens sourced from laboratories around the world, suggests that carbon-doped MgB_2 bulk has a critical temperature dependence given by

$$T_c = 39.43 - 2.515(\rho_{\mathrm{norm}})\ \mathrm{K}, \tag{5.1}$$

where ρ_{norm} represents the normalised contribution of the residual resistivity, $\rho_{\mathrm{norm}} = \frac{\rho_0}{\rho_{\mathrm{ph}}}$. The normalised resistivity values from resistance measurements, together with the critical temperatures determined by AC susceptibility are shown in Table 5-3.

Table 5-3 Normalised resistivity and critical temperature of the specimens produced in this research

Sample	ρ_{norm}	T_c (K)
0%	0.09	33.94
8%	0.54	33.95
12%	0.97	33.76
16%	*1.49*[‡‡]	32.90

Looking at the data, it can be seen that it does not match the fit suggested by Equation (5.1). With a ρ_{norm} of 0.97 for the 12% specimen, the Eisterer fit suggests a T_c around 37 K, and a T_c around 39.2 K for the 0% specimen. In addition, the estimated ρ_{norm} of the 16% specimen would have a

---

[‡‡] Obtained by a simple linear trend analysis, estimated from the 4 ρ_{norm} values of the 0% to 12% specimens.

predicted T_c of around 35.68 K. The data from Table 5-3 is presented along with a linear fit, in Figure 5-20.

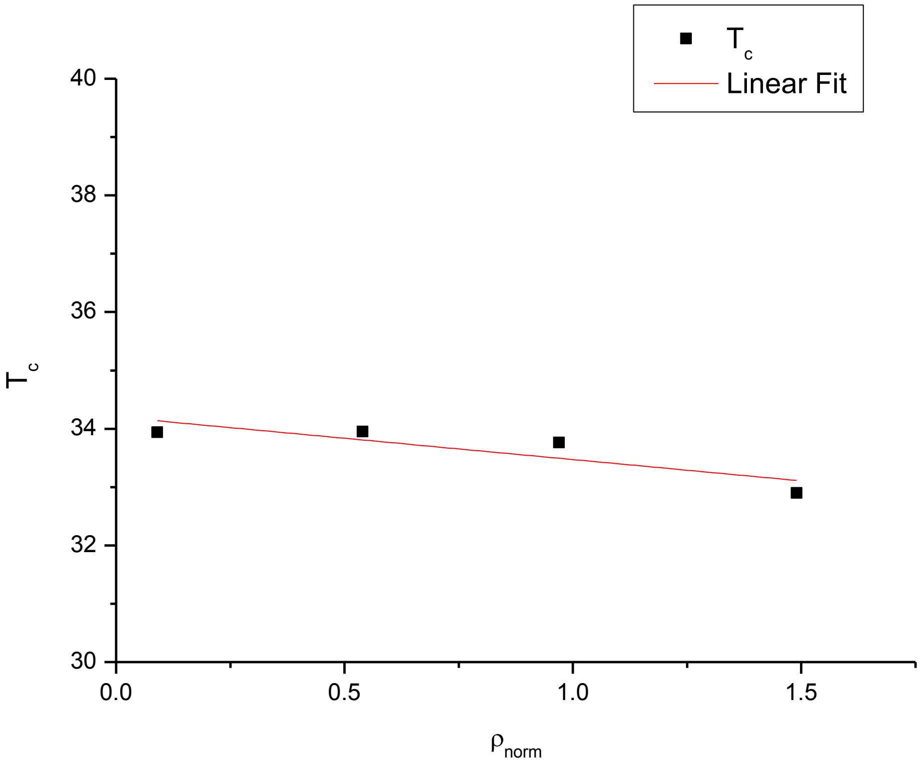

Figure 5-20 Critical temperature dependence on the normalised resistivity. The solid line represents a linear fit applied to the data, described by Equation (5.2)

The linear fit that was applied to the data is given by the equation

$$T_c = 34.20 - 0.73(\rho_{norm}) \text{ K}. \tag{5.2}$$

Here it can be seen that for the specimens produced for this research, a dependency of just $0.73(\rho_{norm})$ is observed, showing that after taking into account all procedures and techniques used, the critical temperature dependence on doping appeared to be small. It is anticipated that this equation will change substantially once the manufacturing process is improved, and the overall T_c suppression reduced. Compared to the Eisterer fit, this equation is move favourable if the suppression of highest T_c from 39.43 K down to 34.20 K still results in a satisfactory operating temperature margin.

Chapter 6 Conclusion

6.1. Summary

This dissertation established institutional memory for initial research in the area of MgB2, which involved the design and construction of various apparatuses that were used to perform CVD, produce MgB2 bulk specimens through the RLI technique, execute resistivity tests, and to perform AC susceptibility tests. With this equipment, a study of the effect of carbon doping on MgB_2 specimens fabricated via the RLI technique was performed. The research goal was to increase the normal state resistivity of MgB_2 by the use of carbon doping, to establish if the resistivity could be increased significantly whilst still maintaining reasonable operational requirements.

Boron powder was doped by chemical vapour deposition of carbon, before being pressed into the designed reaction crucible. Magnesium bulk was then added to the crucible, and the crucible was sealed and heat treated in accordance with the reactive liquid infiltration technique. Ejected specimens were then sectioned for resistive testing and other analysis. Several different techniques for specimen contacts were tested. In the resistivity tests, due to equipment limitation, the measurement current had a suppressive effect on the critical temperature, as well as introducing unnecessary joule heating. The critical temperature data obtained was thus not useful and, was instead measured by analysis of the AC susceptibility of the specimens.

Morphology analysis performed by SEM and optical microscopy revealed that all specimens were dense, featuring few voids, and no signs of impurity phases. There was a clear bimodal grain distribution, and doping did not appear to affect the grain size.

Analysis of resistivity measurements established that doping increased the normal state resistivity, via both increases in the residual resistivity, and phonon-contributed resistivity. From the results of the AC susceptibility measurements, clear transitions were evident, and the critical temperature was defined from these low-field measurements.

Compared to literature reviews, the critical temperature dependence on the normalised resistivity was much lower, but this result should be approached with caution, due to the overall suppression of T_c exhibited by the specimens.

Overall, an order of magnitude increase in resistivity was achieved with a small shift in critical temperature, which satisfied the research goal specifications. The practical implications are highlighted in the intended application area, SFCL devices, where a large increase in current limiting can be achieved with only a small decrease in superconducting properties.

This research is just the start towards practical MgB_2-based SFCL, and several processes have been introduced to the laboratory, to facilitate further investigation. This research was the first attempt at MgB_2 fabrication in the lab, and through the use of the RLI technique was thus the first successful bulks produced. The laboratory is now equipped with equipment suitable for doping powders via chemical vapour deposition, and various temperature-controlled cryogenic sample stages and mounts were built for use in resistive and AC susceptibility investigations. It has also highlighted the issues that require further research, namely in specimen contacts. The pogo-pin apparatus proved to be adequate only for resistivity measurements, but was unsatisfactory for determination of the critical temperature. In early experiments, water degradation was identified as a significant issue in the preparation and storage of specimens, and laboratory practices have been established to ensure that this degradation of specimens is minimised. In addition, the need for key equipment for the laboratory was recognised, namely in low-resistivity measurements.

6.2. Future work

There is still a lot of work to be done on the road to building a scaled SFCL prototype. This research has shown that there is scope to increase the normal state resistivity without a large degradation in T_c, but the next step is determining the actual current limiting properties taking into account the J_c suppression that is likely to occur at higher doping concentrations. The prototype that is to be constructed will be cooled using solid nitrogen, so for an example scenario where, during limiting, the superconductor heats up to the nitrogen solid-liquid temperature of 63 K, the 12% doped specimen would have a resistivity that is a factor of 62 times larger than the undoped specimen. This results in a 62 times great power dissipation for the same operating conditions.

A significant aspect that will be looked at in future is the issue of current and voltage contacts onto the specimens. The area of specimen contacts seems to be a rather specialised one, with limited literature available. There is scope for improving the present apparatus, which will possibly be met with the ability to perform critical current testing as well as resistive testing in the same apparatus. The addition of critical current analysis will prove very valuable, as the extent to which doping alters the critical current is a realistic issue that cannot be neglected for consideration of MgB_2 in practical applications.

This research was the first to produce bulk superconducting MgB_2, and thus with further improvements in the fabrication process, the somewhat low values of T_c can be improved. The values obtained were surprising, which is possibly indicative of an issue with the boron precursor powder, and thus there is certainly scope for improvement.

References

[1] Stavros A Papathanassiou, "A technical evaluation framework for the connection of DG to the distribution network," *Electric Power Systems Research*, vol. 77, no. 1, pp. 24-34, January 2007.

[2] Lin Ye, LiangZhen Lin, and K.-P. Juengst, "Application studies of superconducting fault current limiters in electric power systems," *IEEE Transactions on Apllied Superconductivity*, vol. 12, no. 1, pp. 900-903, March 2002.

[3] Swarn S Kalsi and Alex Malozemoff, "HTS Fault Current Limiter Concept," *Power Engineering Society General Meeting, 2004. IEEE*, vol. 2, pp. 1426-1430, June 2004.

[4] Lin Ye and Liang Zhen Lin, "Study of Superconducting Fault Current Limiters for System Integration of Wind Farms," *IEEE Transactions on Applied Superconductivity*, vol. 20, no. 3, pp. 1233-1237, June 2010.

[5] G.-V Aldica, P Nita, I Tiseanu, T Craciunescu, and P Badica, "High density MgB2 superconductor: structure and morphology through microtomography and SEM investigations," *Journal of optoelectronics and advanced materials*, vol. 10, no. 4, pp. 929-932, April 2008.

[6] G. Giunchi et al., "High density MgB2 bulk materials of different grains size: supercurrents instability and losses in variable magnetic fields," *IEEE Transactions on Applied Superconductivity*, vol. 15, no. 2, pp. 3230-3233, June 2005.

[7] J. S. Slusky et al., "Loss of superconductivity with the addition of Al to MgB2 and a structural transition in Mg1-xAlxB2," *Nature*, vol. 410, no. 6826, pp. 343-345, March 2001.

[8] M. Paranthaman, J. R. Thompson, and D. K. Christen, "Effect of carbon-doping in bulk superconducting MgB2 samples," *Physica C*, vol. 355, no. 1-2, pp. 1-5, June 2001.

[9] S. X. Dou et al., "Substitution-induced pinning in MgB2 superconductor doped with SiC nano-particles," *Superconductor Science and Technology*, vol. 15, no. 11, pp. 1587-1591, November 2002.

[10] E. A. Young and Y. Yang, "Preparation and Properties of Mg(B1 xCx)2 Using Carbon Chemical Vapor Coated Boron," *IEEE Transactions on Applied Superconductivity*, vol. 17, no. 2, pp. 2794-2797, June 2007.

[11] Heike Kamerlingh Onnes, "Further experiments with Liquid Helium C. On the change of electrical resistance of pure metals at very low temperatures etc. IV. The resistance of Gold and pure Mercury at Helium temperatures," vol. 120b, p. 1479, April 1911.

[12] Heike Kamerlingh Onnes, "Further experiments with Liquid Helium D. On the change of electrical resistance of pure metals at very low temperatures etc. V. The disappearance of the resistance of Mercury," vol. 122b, p. 81, May 1911.

[13] Dirk van Delft and Peter Kes, "The discovery of superconductivity," *Physics Today*, vol. 63, no. 9, pp. 38-43, September 2010.

[14] W Meissner and R Ochsenfeld, "Ein neuer Effekt bei Eintritt der Supraleitfähigkeit," *Naturwisseschaft*, vol. 21, no. 44, pp. 787-788, 1933.

[15] Alexei A Abrikosov, "On the Magnetic Properties of Superconductors of the Second Type," *Soviet Physics JETP*, vol. 5, no. 6, pp. 1174-1182, December 1957.

[16] B. T. Matthias, T. H. Geballe, S. Geller, and E. Corenzwit, "Superconductivity of Nb3Sn," *Physical Review*, vol. 95, no. 6, p. 1435, September 1954.

[17] J. E. Kunzler, E. Buehler, F. S. Hsu, and J. H. Wernick, "Superconductivity in Nb3Sn at High Current Density in a Magnetic Field of 88 kgauss," *Physical Review Letters*, vol. 7, no. 5, p. 215, September 1961.

[18] M. C. Jewell, A. Godeke, P. J. Lee, and D. C. Larbalestier, "The Upper Critical Field of Stoichiometric and Off-Stoichiometric Bulk, Binary Nb3Sn," *ADVANCES IN CRYOGENIC ENGINEERING: Transactions of the International Cryogenic Materials Conference - ICMC.*, vol. 711, pp. 474-484, June 2004.

[19] J. K. Hulm and R. D. Blaugher, "Superconducting Solid Solution Alloys of the Transition Elements," *Physical Review*, vol. 123, no. 5, pp. 1569-1580, September 1961.

[20] A. Godeke et al., "Limits of NbTi and Nb3Sn, and Development of W&R Bi-2212 High Field Accelerator Magnets," *IEEE Transactions on Applied Superconductivity*, vol. 17, no. 2, pp. 114-1152, June 2007.

[21] J. W. Ekin, "Superconductors: An Emerging Power Technology," in *Gaseous Dielectrics X*, Athens, 2004, pp. 423-432.

[22] B. D. Josephson, "Possible new effects in superconductive tunnelling," *Physics Letters*, vol. 1, no. 7, pp. 251-253, July 1962.

[23] J. G. Bednorz and K. A. Müller, "Possible high Tc superconductivity in the Ba−La−Cu−O system," *Zeitschrift für Physik B Condensed Matter*, vol. 64, no. 2, pp. 189-193, June 1986.

[24] M. K. Wu, J. R. Ashburn, C. J. Torng, P. H. Hor, and R. L. Meng, "Superconductivity at 93 K in a new mixed-phase Y-Ba-Cu-O compound system at ambient pressure," *Physical Review Letters*, vol. 58, pp. 908-910, March 1987.

[25] J Akimitsu, , January 10, 2001.

[26] Jun Nagamatsu, Norimasa Nakagawa, Takahiro Muranaka, Yuji Zenitani, and Jun Akimitsu, "Superconductivity at 39K in Magnesium Diboride," vol. 410, pp. 63-64, 2001.

[27] Amy Y. Liu, I. I. Mazin, and Jens Kortus, "Beyond Eliashberg Superconductivity in MgB2: Anharmonicity, Two-Phonon Scattering, and Multiple Gaps," *Physical Review Letters*, vol. 87, no. 8, p. 087005, Aug. 2001.

[28] A. B. Kuzmenko, "Multiband and impurity effects in infrared and optical spectra of MgB2," *Physica C*, vol. 456, no. 1-2, pp. 63-74, June 2007.

[29] P. Grant, "Superconductivity: Rehearsals for prime time," *Nature*, vol. 411, no. 6837, pp. 532-533, May 2001.

[30] L. Landau, "Theory of phase transformations. I," *Sov. Phys. JETP*, vol. 7, p. 19, 1937.

[31] L. Landau, "Theory of phase transformations. II," *Sov. Phys. JETP*, vol. 7, p. 627, 1937.

[32] J. W. Gibbs, "A method of geometrical representation of the thermodynamic properties of substances by means of surfaces," *Transactions of the Connecticut Academy of Arts and Sciences*, vol. 2, pp. 382-404, December 1873.

[33] F. London and H. London, "The Electromagnetic Equations of the Supraconductor," *Proceedings of the Royal Society of London. Series A, Mathematical and Physical Sciences*, vol. 149, no. 866, pp. 71-88, March 1935.

[34] A. B. Pippard, "An Experimental and Theoretical Study of the Relation between Magnetic Field and Current in a Superconductor," *Proceedings of the Royal Society of London. Series A, Mathematical and Physical Sciences*, vol. 216, no. 1127, pp. 547-568, February 1953.

[35] V. L. Ginzburg and L. Landau, "On the theory of superconductivity," *Zh. Eksp. Teor. Fiz.*, vol. 20, p. 1064, 1950.

[36] V. L. Ginzburg, "The Present State of the Theory of Superconductivity.II.The Microscopic Theory," *Usp. Fiz. Nauk*, vol. 48, p. 26, 1952.

[37] A. A. Abrikosov, *Doklady Akad. Nauk S.S.S.R.*, vol. 86, p. 489, 1952.

[38] J. Bardeen, L. N. Cooper, and J. R. Schrieffer, "Microscopic Theory of Superconductivity,"

Physical Review, vol. 106, no. 1, pp. 162-164, April 1957.

[39] J. Bardeen, L. N. Cooper, and J. R. Schrieffer, "Theory of Superconductivity," *Physical Review*, vol. 108, no. 5, pp. 1175-1204, December 1957.

[40] L P Gor'kov, "Microscopic derivation of the Ginzburg-Landau equations in the theory of superconductivity," *Sov. Phys. JETP*, vol. 36, no. 6, pp. 1918-1923, December 1959.

[41] L. N. Cooper, "Bound Electron Pairs in a Degenerate Fermi Gas," *Physical Review*, vol. 104, no. 4, pp. 1189-1190, November 1956.

[42] C. A. Reynolds, B. Serin, W. H. Wright, and L. B. Nesbitt, "Superconductivity of Isotopes of Mercury," *Physical Review*, vol. 78, no. 4, p. 487, May 1950.

[43] E. Maxwell, "Isotope Effect in the Superconductivity of Mercury," *Physical Review*, vol. 78, no. 4, p. 477, May 1950.

[44] W. H. Kleiner, L. M. Roth, and S. H. Autler, "Bulk Solution of Ginzburg-Landau Equations for Type II Superconductors: Upper Critical Field Region," *Physical Review*, vol. 133, no. 5A, pp. 1226-1227, March 1964.

[45] U. Essmann and H. Träuble, "The direct observation of individual flux lines in type II superconductors," *Physics Letters A*, vol. 24, no. 10, pp. 526-527, May 1967.

[46] D. Dew-Hughes, "The critical current of superconductors: an historical review," *Low Temperature Physics*, vol. 27, no. 9, pp. 713-722, September 2001.

[47] Stuart Field, Jeff Witt, Franco Nori, and Xinsheng Ling, "Superconducting Vortex Avalanches," *Physical Review Letters*, vol. 74, no. 7, pp. 1206-1209, February 1995.

[48] D Dew-Hughes, "Flux pinning mechanisms in type II superconductors," *Philosophical Magazine*, vol. 30, no. 2, pp. 293-305, 1974.

[49] C. P. Bean, "Magnetization of Hard Superconductors," *Physical Review Letters*, vol. 8, no. 6, pp. 250-253, March 1962.

[50] C. P. Bean, "Magnetization of High-Field Superconductors," *Reviews of Modern Physics*, vol. 36, no. 1, pp. 31-38, January 1964.

[51] Y. B. Kim, C. F. Hempstead, and A. R. Strnad, "Magnetization and Critical Supercurrents," *Physical Review*, vol. 129, no. 2, pp. 528-535, January 1963.

[52] B. T. Matthias and J. K. Hulm, "A Search for New Superconducting Compounds," *Physical Review*, vol. 87, no. 5, pp. 799-806, Sep. 1952.

[53] Morton E. Jones and Richard E. Marsh, "The Preparation and Structure of Magnesium Boride, MgB2," *J. Am. Chem. Soc.*, vol. 76, no. 5, pp. 1434-1436, March 1954.

[54] T. Yildirim et al., "Giant Anharmonicity and Nonlinear Electron-Phonon Coupling in MgB2: A Combined First-Principles Calculation and Neutron Scattering Study," *Physical Review Letters*,

vol. 87, no. 3, p. 037001, July 2001.

[55] W. L. McMillan, "Transition Temperature of Strong-Coupled Superconductors," *Physical Review*, vol. 167, no. 2, pp. 331-344, March 1968.

[56] S. L. Bud'Ko et al., "Boron Isotope Effect in Superconducting MgB2," *Physical Review Letters*, vol. 86, no. 9, pp. 1877-1880, Feb. 2001.

[57] D. G. Hinks, H. Claus, and J. D. Jorgensen, "The complex nature of superconductivity in MgB2 as revealed by the reduced total isotope effect," *Nature*, vol. 411, pp. 457-460, May 2001.

[58] G. Karapetrov, M. Iavarone, W. K. Kwok, G. W. Crabtree, and D. G. Hinks, "Scanning Tunneling Spectroscopy in MgB2," *Physical Review Letters*, vol. 86, no. 19, pp. 4374-4377, May 2001.

[59] T. Takahashi, T. Sato, S. Souma, T. Muranaka, and J. Akimitsu, "High-Resolution Photoemission Study of MgB2," *Physical Review Letters*, vol. 86, no. 21, pp. 4915-4917, May 2001.

[60] I. I. Mazin and V. P. Antropov, "Electronic structure, electron-phonon coupling, and multiband effects in MgB2," *Physica C*, vol. 385, no. 1-2, pp. 49-65, Mar. 2003.

[61] M Tinkham, *Introduction to Superconductivity.*: Courier Dover Publications, 1975.

[62] F. Bouquet, R. A. Fisher, N. E. Phillips, D. G. Hinks, and J. D. Jorgensen, "Specific Heat of Mg11B2: Evidence for a Second Energy Gap," *Physical Review Letters*, vol. 87, no. 4, p. 047001, July 2001.

[63] F. Bouquet et al., "Specific Heat of Single Crystal MgB2: A Two-Band Superconductor with Two Different Anisotropies," *Physical Review Letters*, vol. 89, no. 25, p. 257001, Dec. 2002.

[64] J. J. Tu et al., "Optical Properties of c-Axis Oriented Superconducting MgB2 Films," *Physical Review Letters*, vol. 87, no. 27, p. 277001, Dec. 2001.

[65] F. Manzano et al., "Exponential Temperature Dependence of the Penetration Depth in Single Crystal MgB2," *Physical Review Letters*, vol. 88, no. 4, p. 047002, Jan. 2002.

[66] F. Giubileo et al., "Two-Gap State Density in MgB2: A True Bulk Property Or A Proximity Effect?," *Physical Review Letters*, vol. 87, no. 17, p. 177008, Oct. 2001.

[67] H. Suhl, B. T. Matthias, and L. R. Walker, "Bardeen-Cooper-Schrieffer Theory of Superconductivity in the Case of Overlapping Bands," *Physical Review Letters*, vol. 3, no. 12, pp. 552-554, Dec. 1959.

[68] A. A. Golubov et al., "Specific heat of MgB2 in a one- and a two-band model from first-principles calculations," *Journal of Physics: Condensed Matter*, vol. 14, no. 6, pp. 1353-1360, Feb. 2002.

[69] K.-P. Bohnen, R. Heid, and B. Renker, "Phonon Dispersion and Electron-Phonon Coupling

in MgB2 and AlB2," *Physical Review Letters*, vol. 86, no. 25, pp. 5771-5774, June 2001.

[70] Paul C. Canfield and George W. Crabtree, "Magnesium Diboride: Better Late than Never," *Physics Today*, vol. 56, no. 3, pp. 34-41, March 2003.

[71] A. Floris et al., "Superconducting properties of MgB2 from first principles," *Physica C*, vol. 456, no. 1-2, pp. 45-53, June 2007.

[72] Hyoung Joon Choi, David Roundy, Hong Sun, Marvin L. Cohen, and Steven G. Louie, "First-principles calculation of the superconducting transition in MgB2 within the anisotropic Eliashberg formalism," *Physical Review B*, vol. 66, no. 2, p. 020513, July 2002.

[73] I. I. Mazin et al., "Superconductivity in MgB2: Clean or Dirty?," *Physical Review Letters*, vol. 89, no. 10, p. 107002, Aug. 2002.

[74] S. Tsuda et al., "Carbon-substitution dependent multiple superconducting gap of Mg B2 : A sub-meV resolution photoemission study," *Physical Review B*, vol. 72, no. 6, p. 064527, Aug. 2005.

[75] J. Bardeen, G. Rickayzen, and L. Tewordt, "Theory of the Thermal Conductivity of Superconductors," *Physical Review*, vol. 113, no. 4, pp. 982-994, Feb. 1959.

[76] A. V. Sologubenko, J. Jun, S. M. Kazakov, J. Karpinski, and H. R. Ott, "Thermal conductivity of single-crystalline MgB2," *Physical Review B*, vol. 66, no. 1, p. 014504, June 2002.

[77] J. W. Ekin, *Experimental Techniques for Low-Temperature Measurements: Cryostat Design, Material Properties, And Superconductor Critical-Current Testing*.: Oxford University Press, 2006.

[78] J. D. Jorgensen, D. G. Hinks, and S. Short, "Lattice properties of MgB2 versus temperature and pressure," *Physical Review B*, vol. 63, no. 22, p. 224522, June 2001.

[79] Giovanni Giunchi et al., "Grain size effects on the superconducting properties of high density bulk MgB2," *Superconductor Science and Technology*, vol. 17, no. 9, pp. S583-S588, Sep. 2004.

[80] S. K. Chen, K. A. Yates, M. G. Blamire, and J. L. MacManus-Driscoll, "Strong influence of boron precursor powder on the critical current density of MgB2," *Superconductor Science and Technology*, vol. 18, no. 11, pp. 1473-1477, Nov. 2005.

[81] S. K. Chen and J. L. MacManus-Driscoll, "Enhanced critical current densities in MgB2 by mixing relatively impure boron powders," *Superconductor Science and Technology*, vol. 22, no. 6, June 2009.

[82] V. Grinenko, E. P. Krasnoperov, V. A. Stoliarov, A. A. Bush, and B. P. Mikhajlov, "Superconductivity in porous MgB2," *Journal of Physics: Conference Series*, vol. 43, no. 1, pp. 492-495, June 2006.

[83] Dietrich Stauffer and Amnon Aharony, *Introduction To Percolation Theory*, 2nd ed.: Taylor & Francis, 1994.

[84] A. D. Caplin et al., "Critical fields and critical currents in MgB2," *Superconductor Science*

and Technology, vol. 16, no. 2, pp. 176-182, Feb. 2003.

[85] P. C. Canfield et al., "Superconductivity in Dense MgB2 Wires," *Physical Review Letters*, vol. 86, no. 11, pp. 2423-2426, Mar. 2001.

[86] S. L. Bud'Ko et al., "Magnetoresistivity and Hc2(T) in MgB2," *Physical Review B*, vol. 63, no. 22, p. 220503, June 2001.

[87] Qi Li et al., "Large Anisotropic Normal-State Magnetoresistance in Clean MgB2 Thin Films," *Physical Review Letters*, vol. 96, no. 16, p. 167003, Apr. 2006.

[88] I. Pallecchi et al., "Multiband magnetotransport in the normal state of MgB2," *Physical Review B*, vol. 71, no. 10, p. 104519, Mar. 2005.

[89] M. Eisterer, "Magnetic properties and critical currents of MgB2," *Superconductor Science and Technology*, vol. 20, no. 12, pp. R47-R73, Dec. 2007.

[90] John M. Rowell, "The widely variable resistivity of MgB2 samples," *Superconductor Science and Technology*, vol. 16, no. 6, pp. R17-R27, June 2003.

[91] Akiyasu Yamamoto, Jun-ichi Shimoyama, Kohji Kishio, and Teruo Matsushita, "Limiting factors of normal-state conductivity in superconducting MgB2: an application of mean-field theory for a site percolation problem," *Superconductor Science and Technology*, vol. 20, no. 7, pp. 658-666, July 2007.

[92] S. L. Bud'ko, V. G. Kogan, and P. C. Canfield, "Determination of superconducting anisotropy from magnetization data on random powders as applied to LuNi2B2C, YNi2B2C, and MgB2," *Physical Review B*, vol. 64, no. 18, p. 180506, Nov. 2001.

[93] M. Bhatia, M.D. Sumption, and E.W. Collings, "Effect of various additions on upper critical field and irreversibility field of in-situ MgB2 superconducting bulk material," *IEEE Transactions on Applied Superconductivity*, vol. 15, no. 2, pp. 3204-3206, June 2005.

[94] V. Braccini et al., "High-field superconductivity in alloyed MgB2 thin films," *Physical Review B*, vol. 71, no. 1, p. 012504, Jan. 2005.

[95] A. Gurevich et al., "Very high upper critical fields in MgB2 produced by selective tuning of impurity scattering," *Superconductor Science and Technology*, vol. 17, no. 2, pp. 278-286, Feb. 2004.

[96] V. G. Kogan, "Free Energy and Torque for Superconductors with Different Anisotropies of Hc2 and λ," *Physical Review Letters*, vol. 89, no. 23, p. 237005, Nov. 2002.

[97] Y. Iwasa et al., "A Round Table Discussion on MgB2 Toward a Wide Market or a Niche Production? - A Summary," *IEEE Transactions on Applied Superconductivity*, vol. 16, no. 2, pp. 1457-1464, June 2006.

[98] P. C. Canfield, S. L. Bud'Ko, and D. K. Finnemore, "An overview of the basic physical

properties of MgB2," *Physica C*, vol. 385, no. 1-2, pp. 1-7, Mar. 2003.

[99] V. G. Kogan and S. L. Bud'Ko, "Anisotropy parameters of superconducting MgB2," *Physica C*, vol. 385, no. 1-2, pp. 131-142, Mar. 2003.

[100] C. Ferdeghini et al., "Upper critical fields up to 60 T in dirty magnesium diboride thin films," *IEEE Transactions on Applied Superconductivity*, vol. 15, no. 2, pp. 3234-3237, June 2005.

[101] A. Gurevich, "Limits of the upper critical field in dirty two-gap superconductors," *Physica C*, vol. 456, no. 1-2, pp. 160-169, June 2007.

[102] Y. Yang et al., "Measurement of AC losses in MgB2 wire and bulk conductors at different temperatures," *IEEE Transactions on Applied Superconductivity*, vol. 15, no. 2, pp. 2883-2886, June 2005.

[103] X. H. Zeng et al., "Superconducting MgB2 thin films on silicon carbide substrates by hybrid physical-chemical vapor deposition," *Applied Physics Letters*, vol. 82, no. 13, p. 2097, Mar. 2003.

[104] C. G. Zhuang et al., "Ultrahigh current-carrying capability in clean MgB2 films," *Journal of Applied Physics*, vol. 104, no. 1, p. 013924, July 2008.

[105] V. Braccini et al., "Improvement of Magnetic Field Behavior of Ex-Situ Processed Magnesium Diboride Tapes," *IEEE Transactions on Applied Superconductivity*, vol. 17, no. 2, pp. 2766-2769, June 2007.

[106] David Larbalestier, Alex Gurevich, D. Matthew Feldmann, and Anatoly Polyanskii, "High-Tc superconducting materials for electric power applications," *Nature*, vol. 414, pp. 368-377, Nov. 2001.

[107] E. W. Collings, M. D. Sumption, M. Bhatia, M. A. Susner, and S. D. Bohnenstiehl, "Prospects for improving the intrinsic and extrinsic properties of magnesium diboride superconducting strands," *Superconductor Science and Technology*, vol. 21, no. 10, p. 103001, Oct. 2008.

[108] R. J. Cava, H. W. Zandbergen, and K. Inumaru, "The substitutional chemistry of MgB2," *Physica C*, vol. 385, no. 1-2, pp. 8-15, Mar. 2003.

[109] Cristina Buzea and Tsutomu Yamashita, "Review of the superconducting properties of MgB2," *Superconductor Science and Technology*, vol. 14, no. 11, pp. R115-R146, Nov. 2001.

[110] Jens Kortus, Oleg V. Dolgov, Reinhard K. Kremer, and Alexander A. Golubov, "Band Filling and Interband Scattering Effects in MgB2: Carbon versus Aluminum Doping," *Physical Review Letters*, vol. 94, no. 2, p. 027002, Jan. 2005.

[111] H. Kishan et al., "Superconductivity of nano-TiO2-added MgB2," *Physica C*, vol. 458, no. 1–5, 2007.

[112] T. Masui, "Transport properties and Raman spectra of impurity substituted MgB2," *Physica*

C, vol. 456, no. 1-2, pp. 102-107, June 2007.

[113] Jens Kortus, "Current progress in the theoretical understanding of MgB2," *Physica C*, vol. 456, no. 1-2, pp. 54-62, June 2007.

[114] R. H. Wilke et al., "Systematic Effects of Carbon Doping on the Superconducting Properties of Mg(B1-xCx)2," *Physical Review Letters*, vol. 92, no. 21, p. 217003, May 2004.

[115] M. Angst, S. L. Bud'Ko, R. H. T. Wilke, and P. C. Canfield, "Difference between Al and C doping in anisotropic upper critical field development in MgB2," *Physical Review B*, vol. 71, no. 14, p. 144512, Apr. 2005.

[116] W K Yeoh and S X Dou, "Enhancement of Hc2 and Jc by carbon-based chemical doping," vol. 456, pp. 170-179, 2007.

[117] S. X. Dou et al., "Enhancement of the critical current density and flux pinning of MgB2 superconductor by nanoparticle SiC doping," *Applied Physics Letters*, vol. 81, no. 18, pp. 3419-3421, Oct. 2002.

[118] M. D. Sumption et al., "Irreversibility field and flux pinning in MgB2 with and without SiC additions," *Superconductor Science and Technology*, vol. 17, no. 10, pp. 1180-1184, Oct. 2004.

[119] M. A. Susner et al., "Influence of Mg/B ratio and SiC doping on microstructure and high field transport Jc in MgB2 strands," *Physica C*, vol. 456, no. 1-2, pp. 180-187, June 2007.

[120] J. Chen et al., "Enhancement of flux pinning and high-field critical current density in carbon-alloyed MgB2 thin films," *Physical Review B*, vol. 74, no. 17, p. 174511, Nov. 2006.

[121] S. X. Dou et al., "Mechanism of Enhancement in Electromagnetic Properties of MgB2 by Nano SiC Doping," *Physical Review Letters*, vol. 98, no. 9, p. 097002, Mar. 2007.

[122] Y. Zhang, S. H. Zhou, C. Lu, K. Konstantinov, and S. X. Dou, "The effect of carbon doping on the upper critical field (Hc2) and resistivity of MgB2 by using sucrose (C12H22O11) as the carbon source," *Superconductor Science and Technology*, vol. 22, no. 1, p. 015025, Jan. 2009.

[123] M. S. A. Hossain et al., "Enhancement of flux pinning in a MgB2 superconductor doped with tartaric acid," *Superconductor Science and Technology*, vol. 20, no. 1, pp. 112-116, Jan. 2007.

[124] Arpita Vajpayee et al., "Superconducting properties of adipic-acid-doped bulk MgB2 superconductor," *Superconductor Science and Technology*, vol. 22, no. 1, p. 015016, Jan. 2009.

[125] J. H. Kim et al., "Systematic study of a MgB2+C4H6O5 superconductor prepared by the chemical solution route," *Superconductor Science and Technology*, vol. 20, no. 7, pp. 715-719, July 2007.

[126] Dongliang Wang et al., "Enhancement of the High-Field Jc properties of MgB2/Fe Tapes by Acetone Doping," *Journal of Superconductivity and Novel Magnetism*, vol. 22, no. 7, pp. 671-676, 2009.

[127] K. Rogacki et al., "Strong magnetic pair breaking in Mn-substituted MgB2 single crystals," *Physical Review B*, vol. 73, no. 17, p. 174520, May 2006.

[128] J. Karpinski et al., "Single crystals of MgB2: Synthesis, substitutions and properties," *Physica C*, vol. 456, no. 1-2, pp. 3-13, June 2007.

[129] Steven C. Erwin and I. I. Mazin, "Toward one-band superconductivity in MgB2," *Physical Review B*, vol. 68, no. 13, p. 132505, Oct. 2003.

[130] M. Monni et al., "Role of charge doping and lattice distortions in codoped Mg1-x(AlLi)xB2 compounds," *Physical Review B*, vol. 73, no. 21, p. 214508, June 2006.

[131] Fabio Bernardini and Sandro Massidda, "Anomalous effect of Li-Al codoping in MgB2 : A simple explanation," *Physical Review B*, vol. 74, no. 1, p. 014513, July 2006.

[132] M. Yavas, S. Okur, M. Egilmez, M. Kalkanci, and L. Ozyuzer, "Fabrication of superconducting MgB2 from boron oxide (B2O3), and its microstructural and electrical characterization," *Journal of Optoelectronics and Adavnced Materials*, vol. 7, no. 1, pp. 407-410, February 2005.

[133] Y. Zhang et al., "Significant improvement of Jc in MgB2 bulk superconductor using ball-milled high-purity crystalline boron," *Superconductor Science and Technology*, vol. 21, no. 11, p. 115004, November 2008.

[134] Xun Xu et al., "Effect of boron powder purity on superconducting properties of MgB2," *Superconductor Science and Technology*, vol. 19, no. 6, pp. 466-469, June 2006.

[135] Sihai Zhou, A. V. Pan, J. Horvat, M. J. Qin, and H. K. Liu, "Effects of precursor powders and sintering processes on the superconducting properties of MgB2," *Superconductor Science and Technology*, vol. 17, no. 9, pp. S528-S532, Sep. 2004.

[136] R. A. Ribeiro, S. L. Bud'Ko, C. Petrovic, and P. C. Canfield, "Effects of boron purity, Mg stoichiometry and carbon substitution on properties of polycrystalline MgB2," *Physica C*, vol. 385, no. 1-2, pp. 16-23, Mar. 2003.

[137] A. E. Newkirk, "Elemental Boron," in *Boron, Metallo-Boron Compounds and Boranes*, R M Adams, Ed. New York, United States of America: Interscience, 1694, pp. 233-288.

[138] T. Cavallin, E. A. Young, C. Beduz, Y. Yang, and G. Giunchi, "Thermal Conductivity of Bulk MgB2 Produced by Infiltration of Different Boron Powders," *IEEE Transactions on Applied Superconductivity*, vol. 17, no. 2, pp. 2770-2773, June 2007.

[139] Ji Ping Zhou and John T. McDevitt, "Corrosion reactions of yttrium barium copper oxide (YBa2Cu3O7-x) and thallium barium calcium copper oxide (Tl2Ba2Ca2Cu3O10+x) superconductor phases in aqueous environments," *Chem. Mater.*, vol. 4, no. 4, pp. 953-959, July 1992.

[140] S Jin, "Water reactions of superconducting Bi2Sr2CaCu2O8 phase at O°C and ambient temperature," *Solid State Communications*, vol. 74, no. 10, pp. 1087-1090, June 1990.

[141] H. Y. Zhai et al., "Degradation of superconducting properties in MgB2 films by exposure to water," *Superconductor Science and Technology*, vol. 14, no. 7, pp. 425-428, July 2001.

[142] Y. Cui et al., "Degradation of MgB2 Thin Films in Water," *IEEE Transactions on Applied Superconductivity*, vol. 15, no. 2, pp. 224-227, June 2005.

[143] K. J. Song et al., "The effect of solvent treatments and aging on the superconducting properties of MgB2 materials," *Physica C*, vol. 467, no. 1-2, pp. 106-111, Dec. 2007.

[144] D. K. Aswal et al., "Degradation behavior of MgB2 superconductor," *Physica C*, vol. 363, no. 3, pp. 208-214, Nov. 2001.

[145] A. Serquis et al., "Degradation of MgB2 under ambient environment," *Applied Physics Letters*, vol. 80, no. 23, p. 4401, June 2002.

[146] M. Annabi, A. M'chirgui, F. Ben Azzouz, M. Zouaoui, and M. Ben Salem, "Corrosion process of MgB2 superconductor in a moisture atmosphere," *Physica Status Solidi (C)*, vol. 1, no. 7, pp. 1916-1919, May 2004.

[147] Suchitra Rajput and Sujeet Chaudhary, "Effects of ambient and humidity exposure on the MgB2 superconductor," *Journal of Physics and Chemistry of Solids*, vol. 70, no. 3-4, pp. 516-520, Mar. 2009.

[148] G Giunchi, G Ripamonti, T Cavallin, and E Bassani, "The reactive liquid Mg infiltration process to produce large superconducting bulk MgB2 manufacts," *Cryogenics*, vol. 46, pp. 273-242, 2006.

[149] Zi-Kui Liu, D. G. Schlom, Qi Li, and X. X. Xi, "Thermodynamics of the Mg-B system: Implications for the deposition of MgB2 thin films," *Applied Physics Letters*, vol. 78, no. 23, pp. 3678-3680, 2001.

[150] Joanna R Groza and Antonios Zavaliangos, "Sintering activation by external electrical field," *Materials Science and Engineering: A*, vol. 287, no. 2, pp. 171-177, Aug. 2000.

[151] Mamoru Omori, "Sintering, consolidation, reaction and crystal growth by the spark plasma system (SPS)," *Materials Science and Engineering: A*, vol. 287, no. 2, pp. 183-188, Aug. 2000.

[152] S. Zhou et al., "Effects of sintering atmosphere on the superconductivity of MgB2," *Superconductor Science and Technology*, vol. 22, no. 4, p. 045018, Apr. 2009.

[153] Wolfgang Gawalek et al., "High pressure/high temperature treatment of melt textured YBCO high temperature superconductors," *Czechoslovak Journal of Physics Supplement*, vol. 46, no. 3, pp. 1405-1406, Mar. 1996.

[154] Sergey Lee, "Cyrstal growth of MgB2," *Physica C*, no. 385, pp. 31-41, 2003.

[155] Y. Takano et al., "Superconducting properties of MgB2 bulk materials prepared by high-pressure sinteringc," *Applied Physics Letters*, vol. 78, no. 19, p. 2914, May 2001.

[156] T. A. Prikhna et al., "High-pressure synthesis of MgB2 with and without tantalum additions," *Physica C: Superconductivity*, vol. 372-376, pp. 1543-1545, August 2002, http://www.sciencedirect.com/science/article/B6TVJ-45NGP0N-1G/2/57915275d2adabb94371de90b231a9db.

[157] Michael Tomsic et al., "Overview of MgB2 Superconductor Applications," *International Journal of Applied Ceramic Technology*, vol. 4, no. 3, pp. 250-259, 2007.

[158] Hyper Tech Research, Inc. [Online]. http://www.hypertechresearch.com/page4.html

[159] Alexander Molodyk, Mikhail Novozhilov, Susan Street, Louis Castellani, and Alex Ignatiev, "All-MOCVD Technology for Coated Conductor Fabrication," *IEEE Transactions on Applied Superconductivity*, vol. 21, no. 3, pp. 3175-3178, June 2011.

[160] R. Flükiger, M. S. A. Hossain, C. Senatore, and M. Rindfleisch, "Improved transport properties and connectivity of in situ MgB2 wires obtained by Cold High Pressure Densification (CHPD)," *Physica C*, vol. 471, no. 21, pp. 1119-1123, Nov. 2011.

[161] D. Zhang et al., "Research on Stability of MgB2 Superconducting Magnet for MRI," *IEEE Transactions on Applied Superconductivity*, vol. 21, no. 3, pp. 2100-2103, June 2011.

[162] S. Pittaluga, S. Besio, V. Punzo, and A. Trequattrini, "Racetrack Coils for Dedicated MRI Magnets," *IEEE Transactions on Applied Superconductivity*, vol. 20, no. 3, pp. 786-789, June 2010.

[163] Weijun Yao et al., "A Solid Nitrogen Cooled MgB2 "Demonstration" Coil for MRI Applications," *IEEE Transactions on Applied Superconductivity*, vol. 18, no. 2, pp. 912-915, June 2008.

[164] (2011, Nov.) Team22. [Online]. http://www.igte.tugraz.at/team22/index.php?option=com_content&view=article&id=53&Itemid=63

[165] M.G. Molina, P.E. Mercado, and E.H. Watanabe, "Improved Superconducting Magnetic Energy Storage (SMES) Controller for High-Power Utility Applications," *IEEE Transactions on Energy Conversion*, vol. 26, no. 2, pp. 444-456, June 2011.

[166] Jinhong Liu, Hui Zhang, Jinqi Li, and Yanru Zhong, "Research on high power superconducting magnetic energy storage based on cascaded H-bridge," *2011 International Conference on Electrical and Control Engineering (ICECE)*, pp. 2498-2501, Sept 2011.

[167] I. Serban, R. Teodorescu, J.M. Guerrero, and C. Marinescu, "Modeling of an autonomous microgrid for renewable energy sources integration," *Industrial Electronics, 2009. IECON '09. 35th Annual Conference of IEEE*, pp. 4311-4316, November 2009.

[168] M.H. Ali, Bin Wu, and R.A. Dougal, "An Overview of SMES Applications in Power and

Energy Systems," *IEEE Transactions on Sustainable Energy*, vol. 1, no. 1, pp. 38-47, April 2010.

[169] M.G. Molina and P.E. Mercado, "Power Flow Stabilization and Control of Microgrid with Wind Generation by Superconducting Magnetic Energy Storage," *IEEE Transactions on Power Electronics*, vol. 26, no. 3, pp. 910-922, March 2011.

[170] Kuang Honghai and Wu Zhengqiu, "Research of super capacitor energy storage system based on DG connected to power grid," *International Conference on Sustainable Power Generation and Supply, 2009. SUPERGEN '09*, pp. 1-6, April 2009.

[171] Haisheng Chen et al., "Progress in electrical energy storage system: A critical review," *Progress in Natural Science*, vol. 19, no. 3, pp. 291-312, March 2009.

[172] C.A. Luongo, "Superconducting storage systems: an overview," *IEEE Transactions on Magnetics*, vol. 32, no. 4, pp. 2214-2223, July 1996.

[173] Annette Evans, Vladimir Strezov, and Tim J. Evans, "Assessment of utility energy storage options for increased renewable energy penetration," *Renewable and Sustainable Energy Reviews*, vol. 16, no. 6, pp. 4141-4147, August 2012.

[174] B.-K. Kang, S.-T. Kim, B.-C. Sung, and J.-W. Park, "Preprint, A Study on Optimal Sizing of Superconducting Magnetic Energy Storage in Distribution Power System," *IEEE Transactions on Applied Superconductivity*, vol. PP, no. 99, p. 1, Nov. 2011.

[175] T. Hamajima et al., "Advanced superconducting power conditioning system with SMES for effective use of renewable energy," *Physics Procedia*, vol. 27, pp. 396-399, April 2012.

[176] Naoki Atomura et al., "Conceptual design of MgB2 coil for the 100 MJ SMES of advanced superconducting power conditioning system (ASPCS)," *Physics Procedia*, vol. 27, pp. 400-403, 2012.

[177] K Vinod, R G Abhilash Kumar, and U Syamaprasad, "Prospects for MgB 2 superconductors for magnet application," *Superconductor Science and Technology*, vol. 20, no. 1, pp. R1-R13, 2007.

[178] M. Alessandrini et al., "High critical current of Ti-sheathed MgB2 wires for AC and weight-critical applications," *Superconductor Science and Technology*, vol. 19, no. 1, pp. 129-132, January 2006.

[179] S. X. Dou, E. W. Collings, O. Shcherbakova, and A. Shcherbakov, "Aluminium-stabilized magnesium diboride—a new light-weight superconductor," *Superconductor Science and Technology*, vol. 19, no. 4, pp. 333-337, April 2006.

[180] H. Fujii, K. Togano, and H. Kumakura, "Enhancement of critical current densities of powder-in-tube processed MgB2 tapes by using MgH2 as a precursor powder," *Superconductor Science and Technology*, vol. 15, no. 11, pp. 1571-1576, Nov. 2002.

[181] Sonja I. Schlachter, Wilfried Goldacker, Antje Frank, Bernd Ringsdorf, and Heinrich

Orschulko, "Properties of MgB2 superconductors with regard to space applications," *Cryogenics*, vol. 46, no. 2-3, pp. 201-207, February 2006.

[182] J. S. Panek et al., "Astro-E2 Magnesium Diboride High Current Leads," *ADVANCES IN CRYOGENIC ENGEINEERING: Transactions of the Cryogenic Engineering Conference - CEC. AIP Conference Proceedings*, vol. 710, pp. 952-960, June 2004.

[183] Ch. Haberstroh and G. Zick, "A Superconductive MgB2 Level Sensor for Liquid Hydrogen," *ADVANCES IN CRYOGENIC ENGINEERING: Transactions of the Cryogenic Engineering Conference - CEC. AIP Conference Proceedings*, vol. 823, pp. 679-684, April 2006.

[184] Minoru Takeda, Yu Matsuno, Itaru Kodama, Hiroaki Kumakura, and Chikara Kazama, "Application of MgB2 Wire to Liquid Hydrogen Level Sensor—External-Heating-Type MgB2 Level Sensor," *IEEE Transactions on Applied Superconductivity*, vol. 19, no. 3, pp. 764-767, June 2009.

[185] Piero Spillantini, "Active shielding for long duration interplanetary manned missions," *Advances in Space Research*, vol. 45, no. 7, pp. 900-916, April 2010.

[186] M.A. Green et al., "The two-coil toroid magnet, an option for ASTROMAG," *IEEE Transactions on Magnetics*, vol. 24, no. 2, pp. 1015-1018, March 1988.

[187] P. Spillantini, "Passive cooling of superconducting magnetic systems in space," *Advances in Space Research*, 2012.

[188] Pascal Tixador, "Development of superconducting power devices in Europe," *Physica C*, vol. 470, no. 20, pp. 971-979, Nov. 2010.

[189] B. W. Lee, J. Sim, K. B. Park, and I. S. Oh, "Practical Application Issues of Superconducting Fault Current Limiters for Electric Power Systems," *IEEE Transactions on Applied Superconductivity*, vol. 18, no. 2, pp. 620-623, June 2008.

[190] Lin Ye and A.M. Campbell, "Case study of HTS resistive superconducting fault current limiter in electrical distribution systems," *Electric Power Systems Research*, vol. 77, no. 5-6, pp. 534-539, Apr. 2007.

[191] J. Šouc, F. Gömöry, and M. Vojenčiak, "Coated conductor arrangement for reduced AC losses in a resistive-type superconducting fault current limiter," *Superconductor Science and Technology*, vol. 25, no. 1, p. 014005, Jan. 2012.

[192] Lin Ye et al., "MgB2 Sample Tests for Possible Applications of Superconducting Fault Current Limiters," *IEEE Transactions on Applied Superconductivity*, vol. 17, no. 2, pp. 2826-2829, June 2007.

[193] J. B. Song et al., "The design, fabrication and testing of a cooling system using solid nitrogen for a resistive high-Tc superconducting fault current limiter," *Superconductor Science and*

Technology, vol. 21, no. 11, p. 115023, November 2008.

[194] M. Majoros et al., "Fault Current Limiting Properties of MgB2 Superconducting Wires," *IEEE Transactions on Applied Superconductivity*, vol. 17, no. 2, pp. 1764-1767, June 2007.

[195] Lin Ye et al., "Experimental studies of the quench behaviour of MgB2 superconducting wires for fault current limiter applications," *Superconductor Science and Technology*, vol. 20, no. 7, pp. 621-628, July 2007.

[196] Lin Ye et al., "Investigations of current limiting properties of the MgB2 wires subjected to pulse overcurrents in the benchtop tester," vol. 20, pp. 320-326, 2007.

[197] Tatiana A. Prikhna et al., "High-Pressure Synthesized Nanostructural MgB2 Materials With High Performance of Superconductivity, Suitable for Fault Current Limitation and Other Applications," *IEEE Transactions on Applied Superconductivity*, vol. 21, no. 3, pp. 2694-2697, June 2011.

[198] X. X. Xi, "Two-band superconductor magnesium diboride," *Reports on Progress in Physics*, vol. 71, no. 11, p. 116501, Nov. 2008.

Appendix A Lock-in amplifier software

A software lock-in amplifier was achieved by the use of DASY Lab software in conjunction with an IOTech DaqBook 2000 Ethernet-based data acquisition device. The schematic developed is shown over-page in Figure A1.

The reference signal and input signal are input from the analogue input module, after which the reference signal undergoes a calibration phase adjustment, and a further 90-degree phase shift to generate the imaginary reference.

The three signals; the input, reference and imaginary reference, are then filtered by low-pass and high-pass filters to achieve narrow band-pass filtering. The signals are then mixed by the two multipliers, and low pass filtered to extract the DC value.

As the sampling frequency is 25 kHz, all data is passed through the system at 25 kHz, resulting in a rather excessive data rate for this application. If data were written to disk at this rate, it would write approximately 350 MB of data per run. As the timing interval for the thermometry is 2 seconds, it was not necessary to record data at a rate faster than this. A timing system discards the majority of data, but allows one set of data to be written to disk every 2 seconds, to coincide with the thermometry readings.

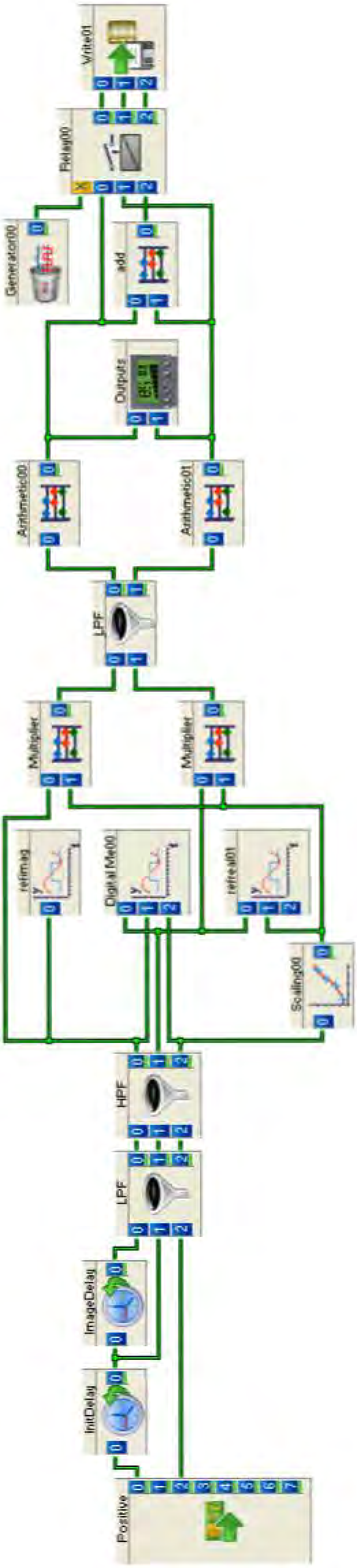

Figure A1 Software lock-in amplifier, constructed in DASY Lab, used in the AC susceptibility measurements.

Appendix B Temperature Logger Software

For the logging of temperature data, software written by Brett Swann [unpublished], one of the past students from the lab, was used. The software is probably 95% his work, and only 5% mine, but is presented here just for completeness. The software interfaces with the Lakeshore Model 336 temperature controller over an Ethernet connection, and provides remote logging of data and setting of control outputs. A history of the temperature and derivatives are display, which allows for easy identification of cooling problems (such as sudden drop in cooling rate arising from an increase in cryostat pressure).

The particular features that I have introduced are the filtering of data using a Savitzky-Golay (SG) algorithm, and the control output section. The filter used is simply a weighted filter with the coefficients determined by the SG algorithm, which preserves more local maxima information than other weighted filters. Both temperature and raw sensor data are filtered, and derivatives are calculated off of this smoothed data.

The output control features were added to provide easy manipulation of the tuning parameters, ramps and setpoints of the controller, all on one page. This was necessary, as the tuning parameters varied considerably at low temperatures, and thus required frequent adjustment. As the measurement periods during resistive testing were substantial, it was essential that temperature stability remained as great as possible. Temperature oscillations could be reduced to 30 mK in certain ranges.

Some screenshots of the interface are shown in Figure B1, Figure B2, and Figure B3.

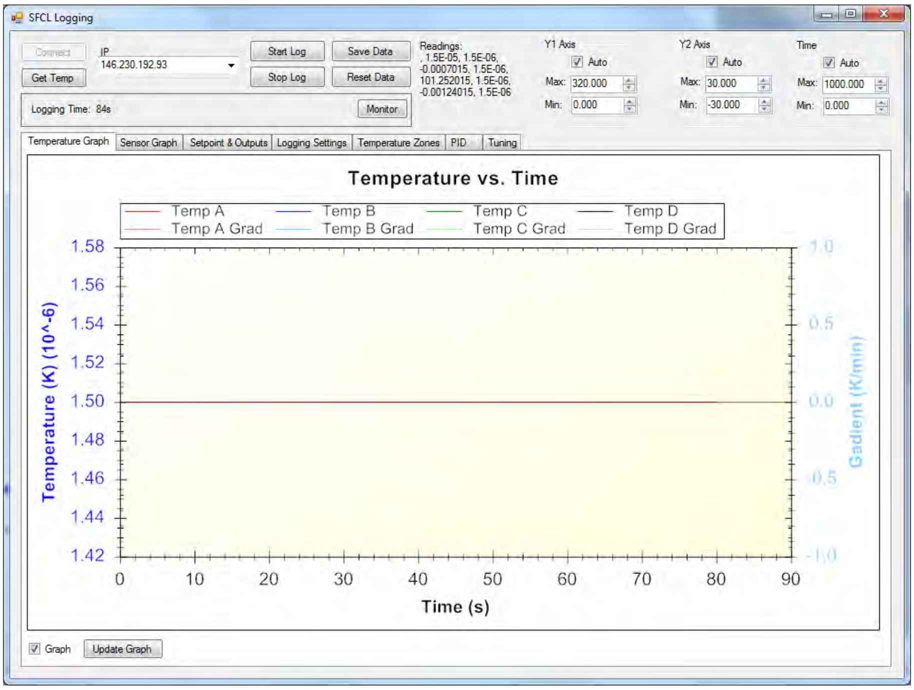

IP
146.230.192.93

Logging Time: 84s

Readings:
, 1.5E-05, 1.5E-06,
-0.0007015, 1.5E-06,
101.252015, 1.5E-06,
-0.00124015, 1.5E-06

Y1 Axis
☑ Auto
Max: 320.000
Min: 0.000

Y2 Axis
☑ Auto
Max: 30.000
Min: -30.000

Time
☑ Auto
Max: 1000.000
Min: 0.000

☑ Graph

Figure B1 Main page of the logging software: shows temperature and temperature derivative histories.

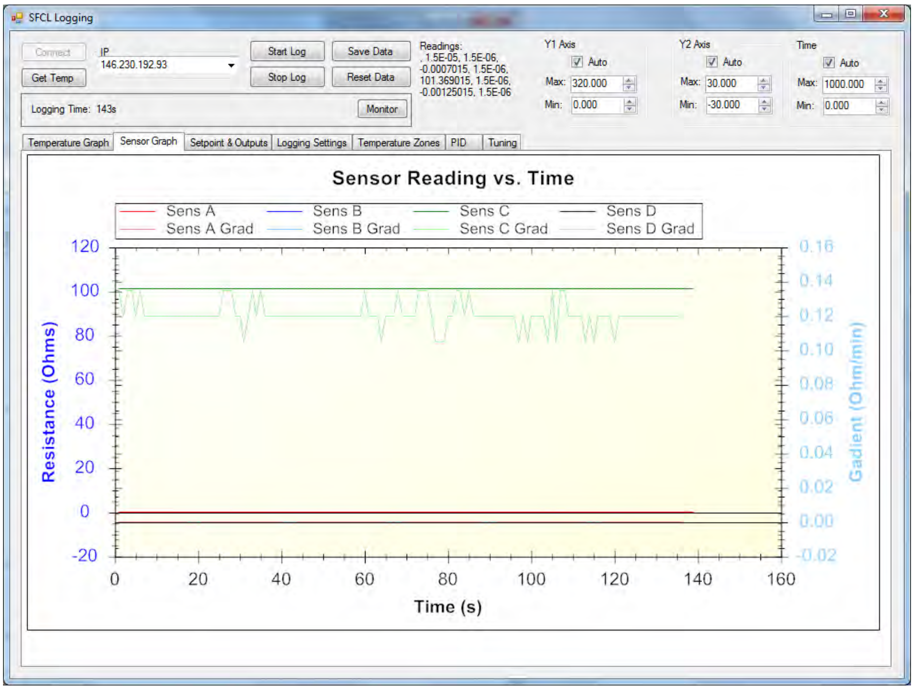

IP
146.230.192.93

Logging Time: 143s

Readings:
, 1.5E-05, 1.5E-06,
-0.0007015, 1.5E-06,
101.369015, 1.5E-06,
-0.00125015, 1.5E-06

Y1 Axis
☑ Auto
Max: 320.000
Min: 0.000

Y2 Axis
☑ Auto
Max: 30.000
Min: -30.000

Time
☑ Auto
Max: 1000.000
Min: 0.000

Figure B2 Sensor page: used if calibration data is not loaded into the temperature controller, or when the sensor is operating out of the calibration range.

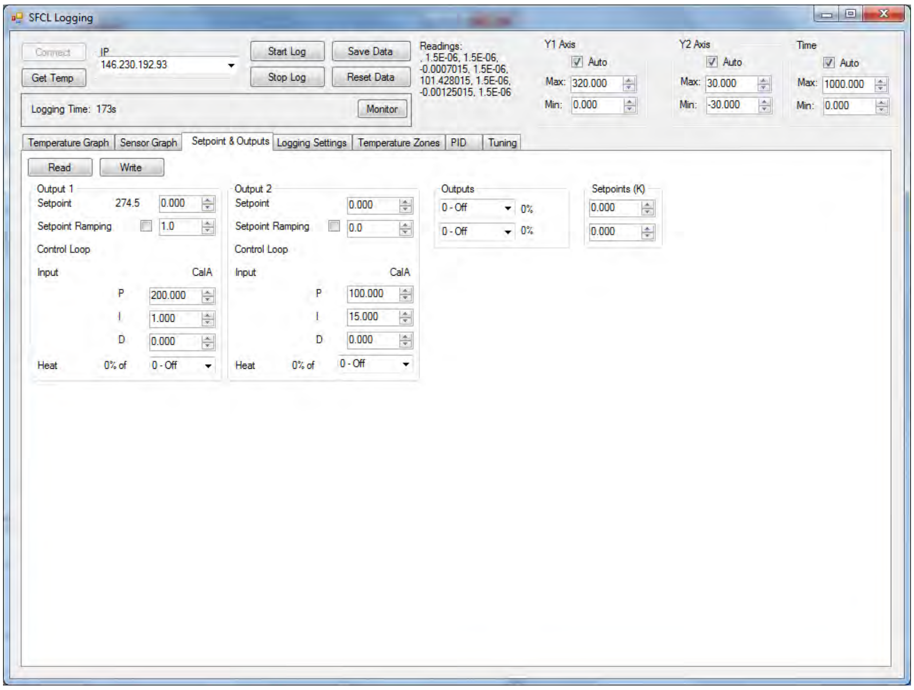

IP: 146.230.192.93

Readings:
, 1.5E-06, 1.5E-06,
-0.0007015, 1.5E-06,
101.428015, 1.5E-06,
-0.00125015, 1.5E-06

Logging Time: 173s

Y1 Axis: ☑ Auto, Max: 320.000, Min: 0.000

Y2 Axis: ☑ Auto, Max: 30.000, Min: -30.000

Time: ☑ Auto, Max: 1000.000, Min: 0.000

Output 1
Setpoint 274.5 0.000
Setpoint Ramping ☐ 1.0
Control Loop
Input CalA
P 200.000
I 1.000
D 0.000
Heat 0% of 0 - Off

Output 2
Setpoint 0.000
Setpoint Ramping ☐ 0.0
Control Loop
Input CalA
P 100.000
I 15.000
D 0.000
Heat 0% of 0 - Off

Outputs
0 - Off 0%
0 - Off 0%

Setpoints (K)
0.000
0.000

Figure B3 Control output page: used to remotely set the control setpoints, ramp, tuning parameters and heater power.